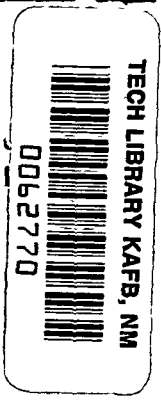




IN COPY: RET  
AFWL TECHNICAL  
KIRTLAND AFB,



INERT GAS THRUSTERS

PREPARED FOR  
LEWIS RESEARCH CENTER  
NATIONAL AERONAUTICS AND SPACE ADMINISTRATION  
GRANT NSG 3011

Annual Report  
July 1975  
Harold R. Kaufman  
Department of Mechanical Engineering  
Colorado State University  
Fort Collins, Colorado

December 16, 1976

TO: NASA Distribution List

RE: Correction to NASA CR-135102 under Grant NSG-3011

After publication a correction was found concerning NASA CR-135102 under Grant NSG-3011. Reported electron densities in the hollow cathode chamber were 100 times too high. On page 41 the last sentence should read: "The electron density is  $\sim 10^{12}/\text{cm}^3$  (below a 35 V discharge), which is  $\sim 10$  times more dense than a typical ion thruster discharge chamber." In Figs. 23-24 the electron density exponent should be 12 not 14.



0062770

1 Report No NASA CR-135100		2 Government Accession No		3 Recipient's Catalog No	
4 Title and Subtitle INERT GAS THRUSTERS (u)				5 Report Date July 1976	
				6 Performing Organization Code	
7 Author(s) Harold R. Kaufman				8 Performing Organization Report No	
				10 Work Unit No	
9 Performing Organization Name and Address Department of Mechanical Engineering Colorado State University Fort Collins, Colorado 80523				11 Contract or Grant No NSG 3011	
				13 Type of Report and Period Covered Contractor Report 1 Aug. 1975 - 30 July 1976	
12 Sponsoring Agency Name and Address National Aeronautics and Space Administration Washington, D.C. 20546				14 Sponsoring Agency Code	
15 Supplementary Notes Grant Manager, Michael J. Mirtich, Jr. Spacecraft Technology Division NASA Lewis Research Center Cleveland, Ohio 44135					
16 Abstract <p>Inert gases are of interest as possible alternatives to the usual electric thruster propellants of mercury and cesium. The multipole discharge chamber investigated has been shown capable of low discharge chamber losses and flat ion beam profiles with a minimum of optimization. Minimum discharge losses were 200-250 eV/ion for xenon and 300-350 eV/ion for argon, while flatness parameters in the plane of the accelerator grid were 0.85 - 0.95. The design used employs low magnetic field strengths, which permits the use of sheet-metal parts. The corner problem of the discharge chamber was resolved with recessed corner anodes, which approximately equalized both the magnetic field above the anodes and the electron currents to these anodes.</p> <p>Argon hollow cathodes were investigated at currents up to about 5 amperes using internal thermionic emitters. Cathode chamber diameter optimized in the 1.0 to 2.5 cm range, while orifices diameter optimized in the 0.5 to 5 mm range. The use of a bias voltage for the internal emitter extended the operating range and facilitated starting.</p> <p>The masses of 15 and 30 cm flight-type thrusters were estimated at about 4.2 and 10.8 kg. The masses of these basic designs could be reduced by the use of contoured shapes for anodes and pole pieces, as well as the substitution of lighter materials for the stainless steel parts. Recommendations were also made for the development program of an inert gas thruster.</p>					
17 Key Words (Suggested by Author(s)) Electrostatic thruster Ion source			18 Distribution Statement  Unclassified-Unlimited		
19 Security Classif (of this report) Unclassified		20 Security Classif (of this page) Unclassified		21 No of Pages	22 Price*

\* For sale by the National Technical Information Service, Springfield, Virginia 22161

## TABLE OF CONTENTS

	Page
I. INTRODUCTION . . . . .	1
II. MULTIPOLE DISCHARGE CHAMBER . . . . .	2
Experimental Configuration . . . . .	3
Magnetic Field . . . . .	6
Chamber Length . . . . .	9
Propellant Flow Rate . . . . .	17
Ion Beam Profiles . . . . .	17
Performance Correlation . . . . .	22
III. ELECTRON DEFLECTION IN A SPATIALLY VARYING MAGNETIC INDUCTION . . . . .	26
IV. ARGON HOLLOW CATHODE . . . . .	29
Test Environment Effects . . . . .	31
Cathode Size Effect . . . . .	39
Enclosed Keeper . . . . .	41
Effect of Barium-Strontium Oxides . . . . .	43
Comparison of Xenon and Argon . . . . .	43
Orifice Size Effect . . . . .	45
Emitter Bias Effect . . . . .	51
Magnetic Orifice Cathode . . . . .	53
Discharge Chamber Cathode . . . . .	56
Cathode Chamber Plasma Properties . . . . .	62
Cathode Starting . . . . .	71
V. FLIGHT-TYPE THRUSTERS . . . . .	72
VI. GAS THRUSTER PROPULSION SYSTEM . . . . .	78
Tankage . . . . .	78

	Page
Flow Metering and Control . . . . .	80
Isolation . . . . .	81
Cathodes . . . . .	81
Discharge Chamber Erosion . . . . .	82
Starting and Control . . . . .	82
Propulsion-System Characteristics . . . . .	82
Summary of Recommendations . . . . .	84
VII. CONCLUDING REMARKS . . . . .	86
REFERENCES . . . . .	88

## I - INTRODUCTION

The development of electron-bombardment thrusters has been pursued primarily with mercury and cesium propellants. Researchers have demonstrated, however, that electron-bombardment thrusters can be operated on a variety of gases.<sup>1-5</sup> Of the gases considered in these studies, the one whose physical characteristics are most suited to space propulsion is xenon. The high atomic weight and ease of storage (low tankage fraction) are the major factors in this choice. Argon is a more economical alternate for space propulsion if tons of propellant are required (so that cryogenic storage is practical) and readily available electric power makes efficiency (and hence atomic weight) less important. Argon is also the preferred propellant in ground applications of thruster technology such as ion etching and sputter deposition.

The use of both argon and xenon propellants in electric thrusters was studied in this investigation, although the use of argon was emphasized. The major efforts were on discharge-chamber and electron emission technologies, and two large sections of this report describe the progress in these areas. A multipole approach is used for the discharge chamber, while a hollow cathode approach is used for electron emission. Another section describes program requirements of gas thruster propulsion systems. Two short sections include a derivation of primary-electron interaction with the magnetic field and flight-type structures for the multipole approach used herein.

SI (rationalized mks) units are used throughout this report.

## II - MULTIPOLE DISCHARGE CHAMBER

by Gerald C. Isaacson

The multipole approach used herein was first described in the previous annual progress report of this Grant.<sup>1</sup> This approach is conceptually related to both the multipole design of Moore<sup>2</sup> and Ramsey<sup>3</sup> and the cusped field design of Beattie and Wilbur<sup>4,5</sup>. The detailed design is similar to the cusped field thruster in that thin pole pieces of soft iron are used with electromagnets between adjacent pole pieces. The major difference from the cusped field thruster is that more and smaller pole pieces are used, giving a larger fraction of low-field-strength volume in the ion chamber. The major similarities to the Moore and Ramsey design are the large number of pole pieces used and the general discharge-chamber shape. Moore and Ramsey, however, used permanent magnets as pole pieces, with the magnetization direction towards or away from the center of the discharge chamber. When permanent magnets are used in the design studied herein, they replace the electromagnets between adjacent pole pieces rather than become the pole pieces. As an additional difference, Moore and Ramsey used much higher magnetic field strengths.

The multipole approach was selected because of the general high performance level of this type of discharge chamber. Documented performance did not include beam profiles when the multipole approach was first selected. Past experience with a wide range of designs, though, indicated the multipole approach should produce very uniform beams. This expectation was later supported by experimental data,<sup>1</sup> with flatness parameters typically in the 0.70-0.75 range. The previous annual report of this Grant also gave minimum discharge losses of 200-250 eV/ion. The

biggest shortcomings of this previous work were marginal magnetic field strength and corner losses. The design described in this annual report corrected both of these shortcomings. The range of magnetic field strength was extended to well above the "optimum" value, while the recessed corner anodes suggested in the previous annual report corrected the excessive electron currents to those anodes.

### Experimental Configuration

The 15-cm multipole thruster used in this investigation is shown in Fig. 2-1. This design makes extensive use of flat or cylindrical sheet-metal parts. The pole pieces are fabricated of 1.5-mm thick soft iron. The side pole pieces are flat with an internal diameter of 15 cm, while the back wall (upstream) pole pieces are cylindrical with mean diameters of about 5, 10, and 15 cm. A center-to-center spacing of 2.7 cm was used for the pole pieces, with 1.5-mm thick stainless steel anodes positioned midway between each pair of pole pieces. Sealing of the discharge chamber was accomplished with stainless steel rings just outside the anodes. These rings were flat for the upstream end of the discharge chamber and cylindrical for the side. Each side section, consisting of anode, sealing ring, two pole pieces, and the electromagnets between the pole pieces, could be added or removed as a unit. This modular approach permitted the discharge chamber length to be conveniently varied in 2.7 cm increments.

The disposition of electromagnets was twelve between each pair of side pole pieces, eight between the 10 and 15 cm upstream pole pieces, and four between the 5 and 10 cm upstream pole pieces. The electromagnets

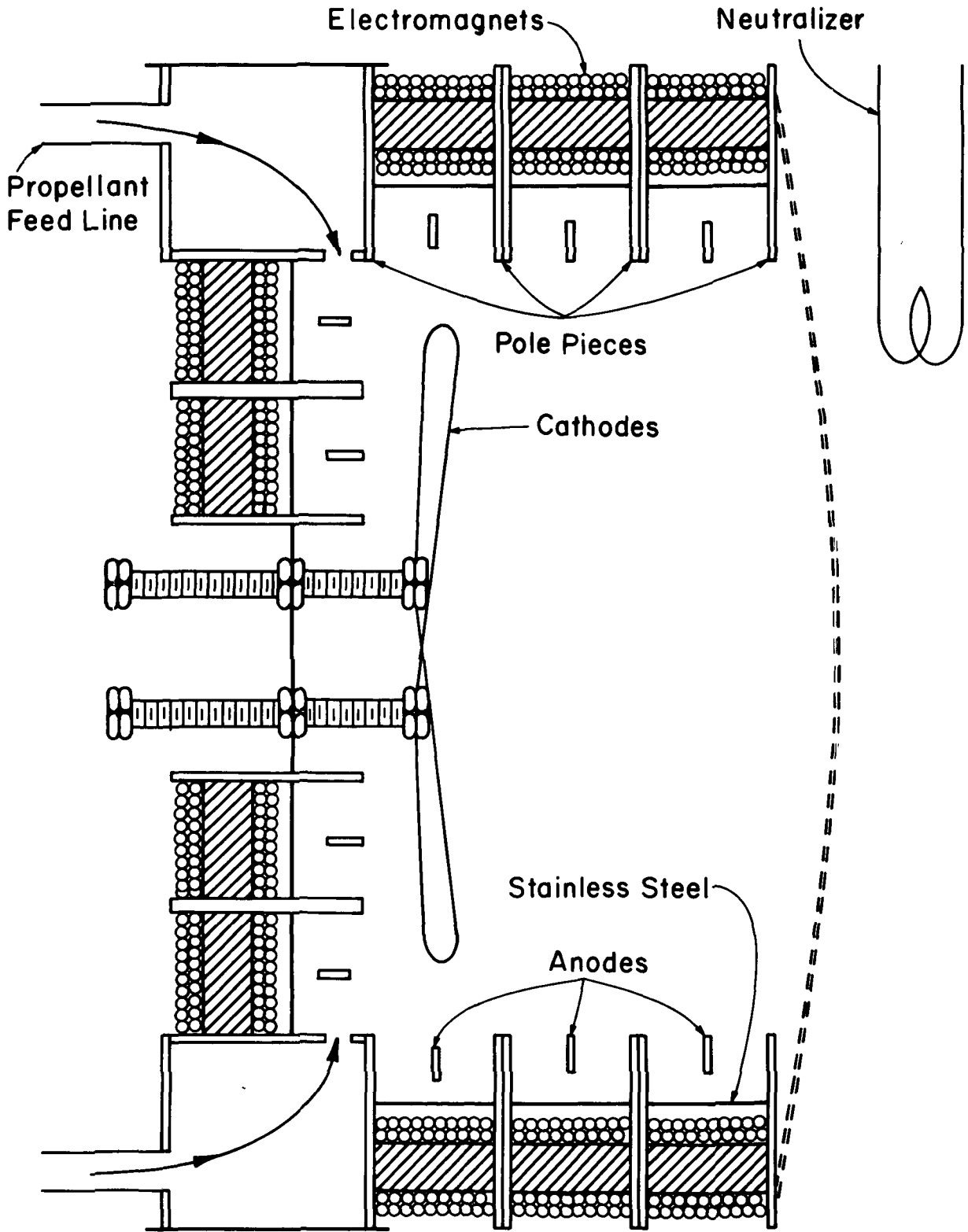


Figure 2-1. Sketch of Multipole Gas Ion Thruster.

in each section were positioned so that they were not circumferentially in line with electromagnets in adjoining sections. This was done to avoid the saturation problems that might have otherwise occurred. All the electromagnets were connected in series so that the current was the same in all electromagnets.

Dished small hole accelerator grid (S.H.A.G.) optics were used, with a 67 percent open screen and a 24 percent open accelerator. The thicknesses of the screen and accelerator grids were about 0.4 and 0.5 mm. The center-to-center hole spacing within each grid was about 2.2 mm and they were assembled with an interelectrode spacing of about 1 mm. All data presented were obtained at +1000 and -500 volts for screen and accelerator potentials.

Inasmuch as long-life cathodes were the subject of a separate investigation, 0.25-mm tungsten wire was used for both the main and neutralizer cathodes. The propellant was introduced into the annular region formed by the two corner pole pieces, as shown in Fig. 1. Several 6 mm holes permitted flow radially inwards into the discharge chamber.

Propellant flow was controlled with an adjustable leak valve and measured with a mass flowmeter. The flow rate was maintained within  $\pm 1$  percent of the desired value while data were being obtained. A Faraday cup probe was installed 6.5 mm downstream of the accelerator grid, which was installed convex side out. This probe was translated across the beam for current density profiles. Details of the Faraday probe and associated electronics are given by Wilbur.<sup>6</sup> An E x B momentum analyzer was installed with the sensing probe 68 cm downstream of the accelerator grid. This probe was moveable transverse to the ion beam, with the path

of motion passing through the center of the ion beam. Details of the E x B sensing probe and its operation are given by Vahrenkamp,<sup>7</sup> with the method of analyzing the data given by Beattie.<sup>8</sup>

All propellant utilizations presented in this report were corrected for double ionization and propellant backflow. The propellant backflow was calculated from facility pressure and the free-molecular-flow conductance of the accelerator system. The double ionization was calculated using the surveys of the E x B momentum analyzer.

### Magnetic Field

An iron filing map of the magnetic field is shown in Fig. 2-2. As shown, the primary electrons must cross a region of relatively strong magnetic field near each of the anodes in order to escape from the discharge chamber. A simple model was developed in the previous annual report to help determine the optimum magnetic field strength for a thruster. The pictorial representation of this model is reproduced from the preceding annual report in Fig. 2-3. It is evident from Fig. 2-3(a) that the deepest penetration into the region of magnetic field above an anode corresponds to two electron cyclotron radii. As shown in the previous annual report, this penetration corresponds to a product of field strength times depth of

$$2r_c B = 6.74 \times 10^{-6} \sqrt{E} \text{ ,}$$

where the primary electron energy E is in eV. Using an integrated field of  $\int B dx$  in place of  $2r_c B$ , the same magnitude is shown to be required for a nonuniform field strength in Section III. For a 50 eV electron, a field integral of  $48 \times 10^{-6}$  tesla-m (48 Gauss-cm) is required.

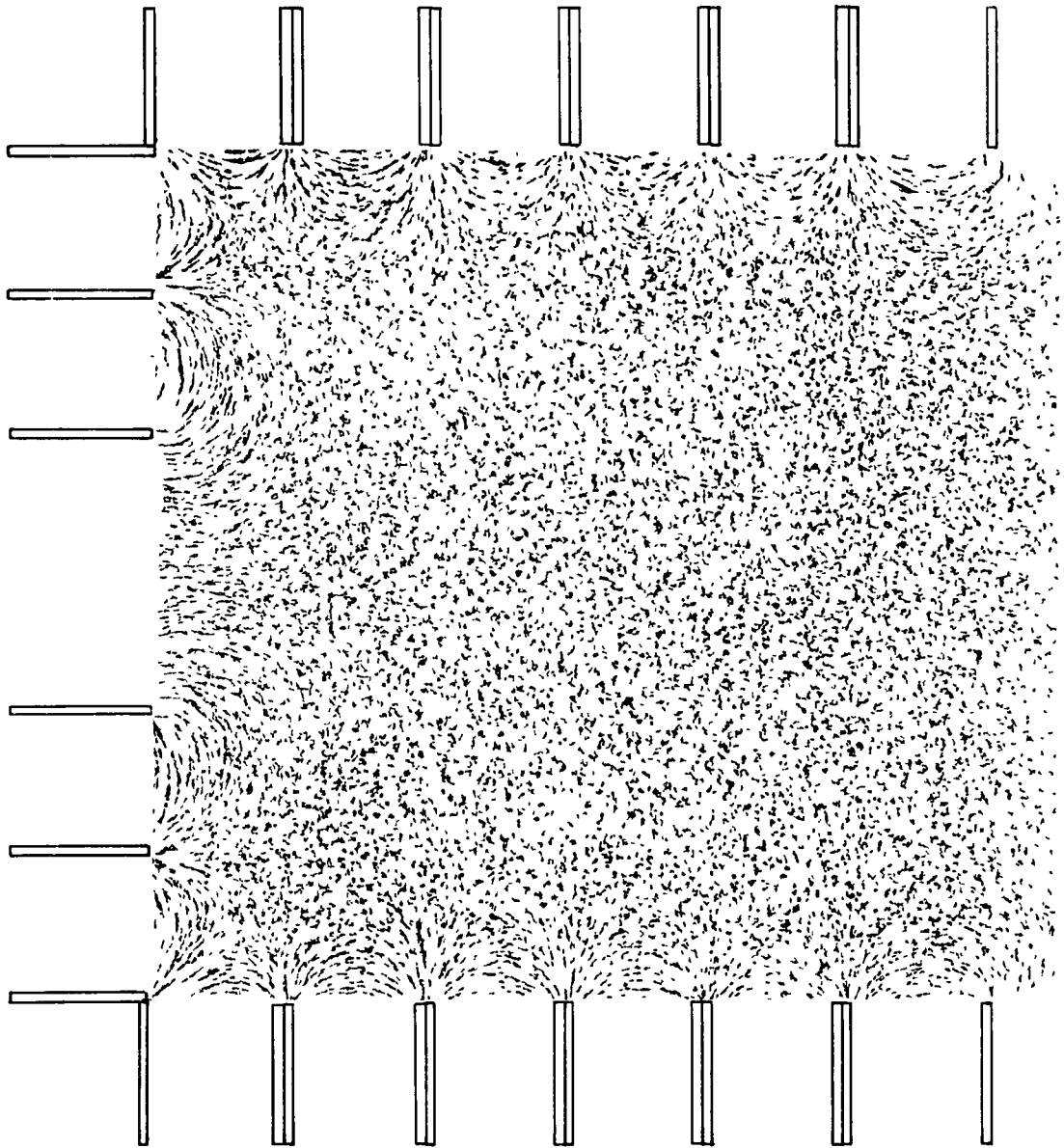
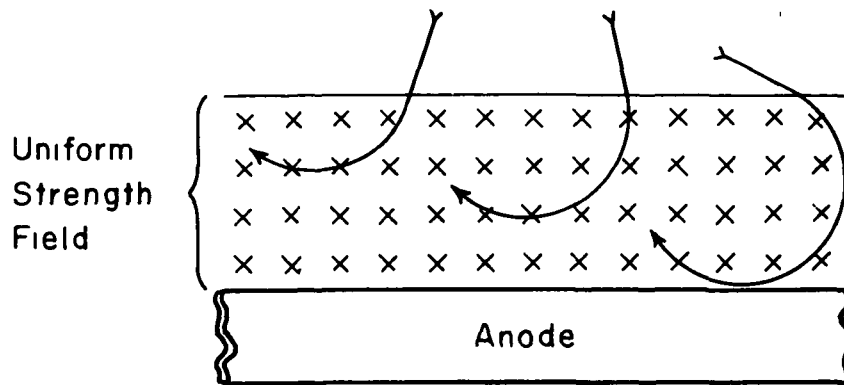
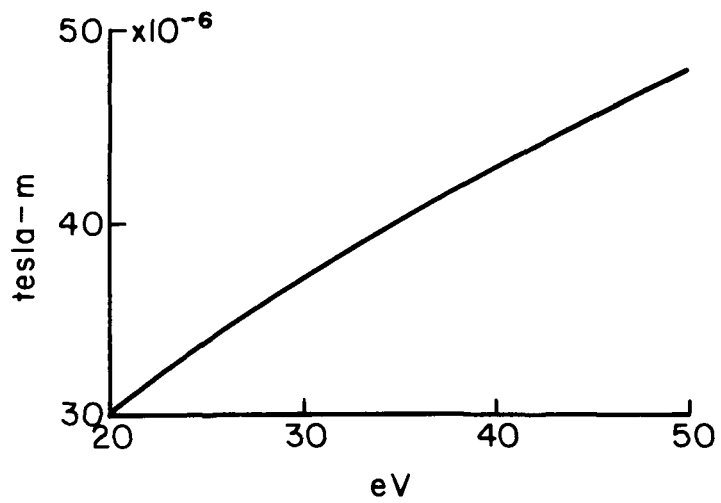


Figure 2-2. Iron filing magnetic-field map.



(a) Simplified Deflection Configuration



(b) Required Flux per Unit Anode Length as a Function of Electron Energy

Figure 2-3. Electron interaction with fringe magnetic field above anode.

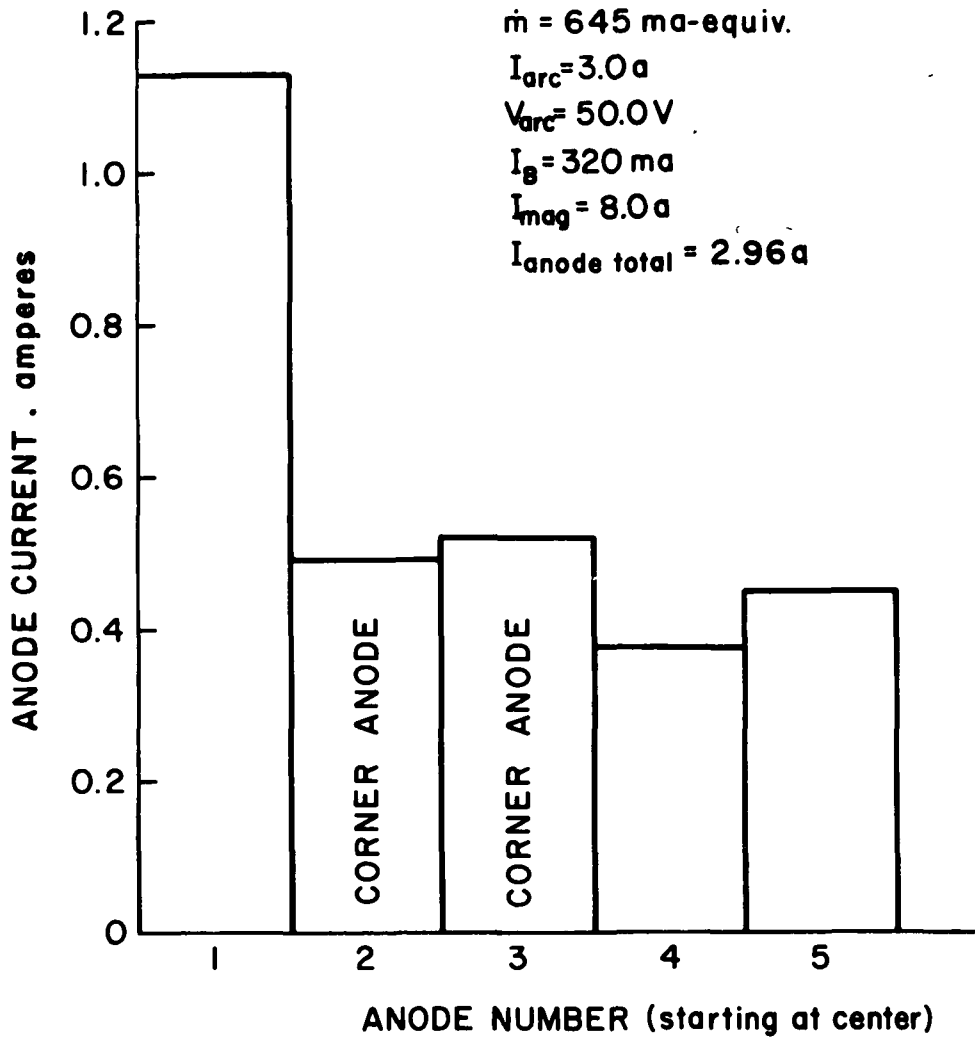
The experimental variation of magnetic field above each anode was obtained and numerically integrated to compare with the theoretical model. The integrated values above the corner anodes were about 80 percent of the values above other anodes. To provide the same primary electron containment at these corner anodes, the corner anodes were recessed 2.5 mm instead of being flush with the pole pieces (see Fig. 2-1). This recess was roughly 10 percent of the pole-piece spacing, rather than the 20 percent found in the study of simulated pole pieces described in the previous annual report. The distribution of current to the anodes is shown in Fig. 2-4. This distribution is fairly uniform, which is an independent check on the amount of recess used for the corner anodes.

The variation of discharge loss with electromagnet current is shown in Fig. 2-5. The discharge loss decreased with increasing magnet current for both propellants, reaching a minimum at about 8 amperes. Numerical integration of the field above the anodes at 8 amperes yielded about  $100 \times 10^{-6}$  tesla-m. From Fig. 2-3(b), the theoretical value should be  $45 - 48 \times 10^{-6}$  tesla-m for a 45-50 V discharge. This factor of 2 difference between experiment and theory is reasonable in view of the simple model used.

#### Chamber Length

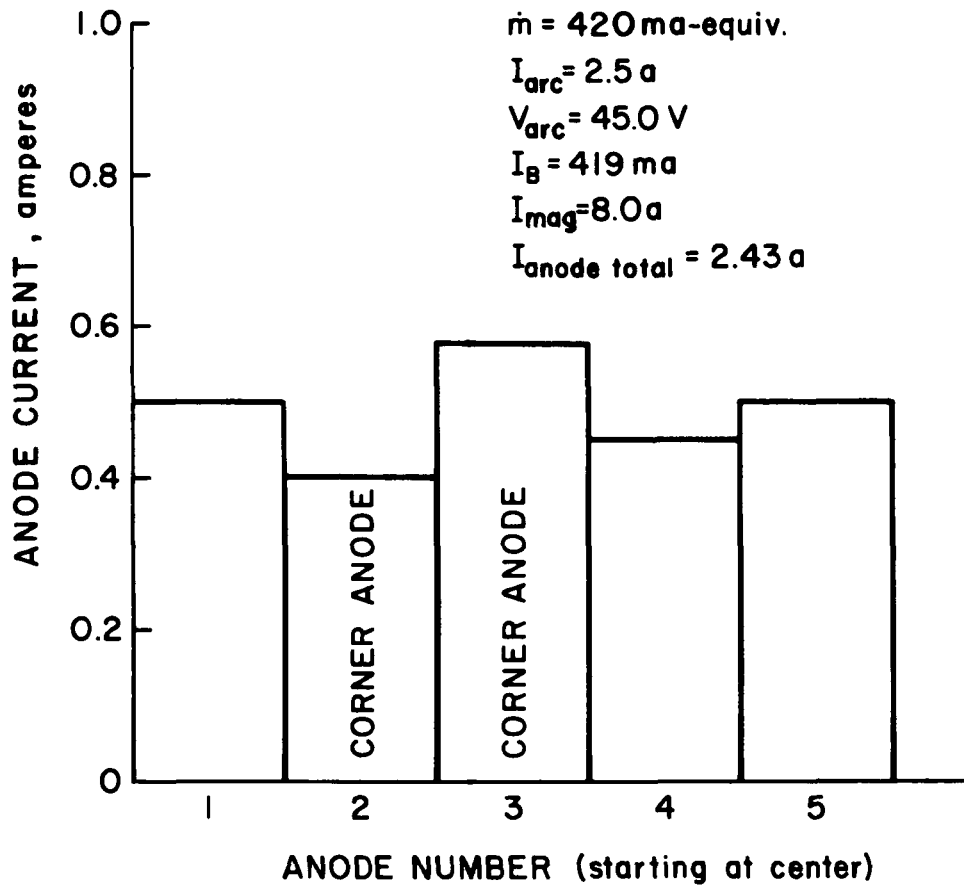
The effects of discharge-chamber length on performance were investigated. The chamber length was decreased from a maximum of 16.2 cm in 2.7 cm increments for both propellants. The electromagnet current was kept constant at 8 amperes, which was near optimum for both propellants.

Discharge-chamber performance is shown in Fig. 2-6 for argon



(a) Argon propellant

Figure 2-4. Anode distribution of discharge current.



(b) Xenon propellant

Figure 2-4. Concluded.

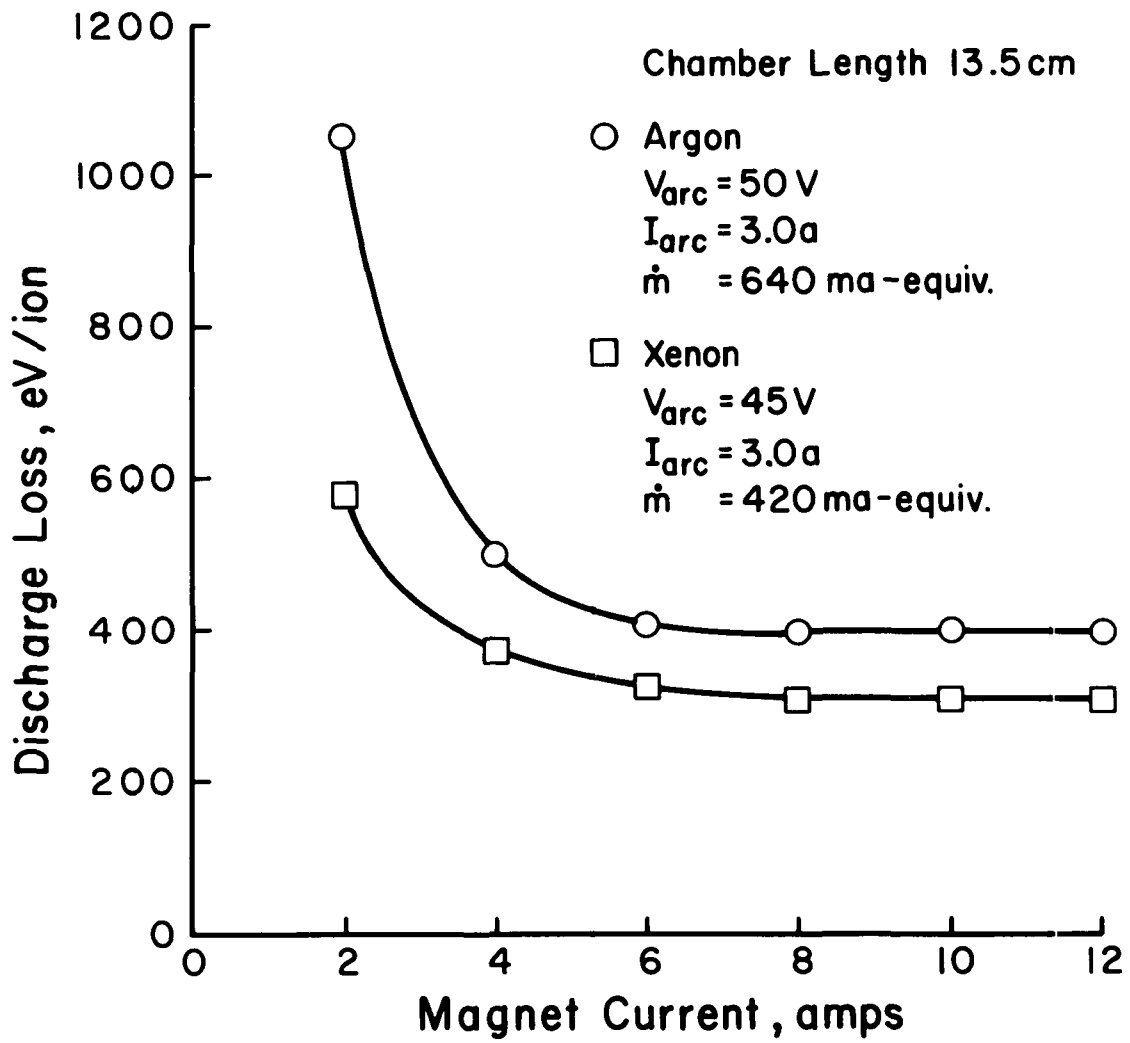


Figure 2-5. Variation of discharge loss with magnet current.

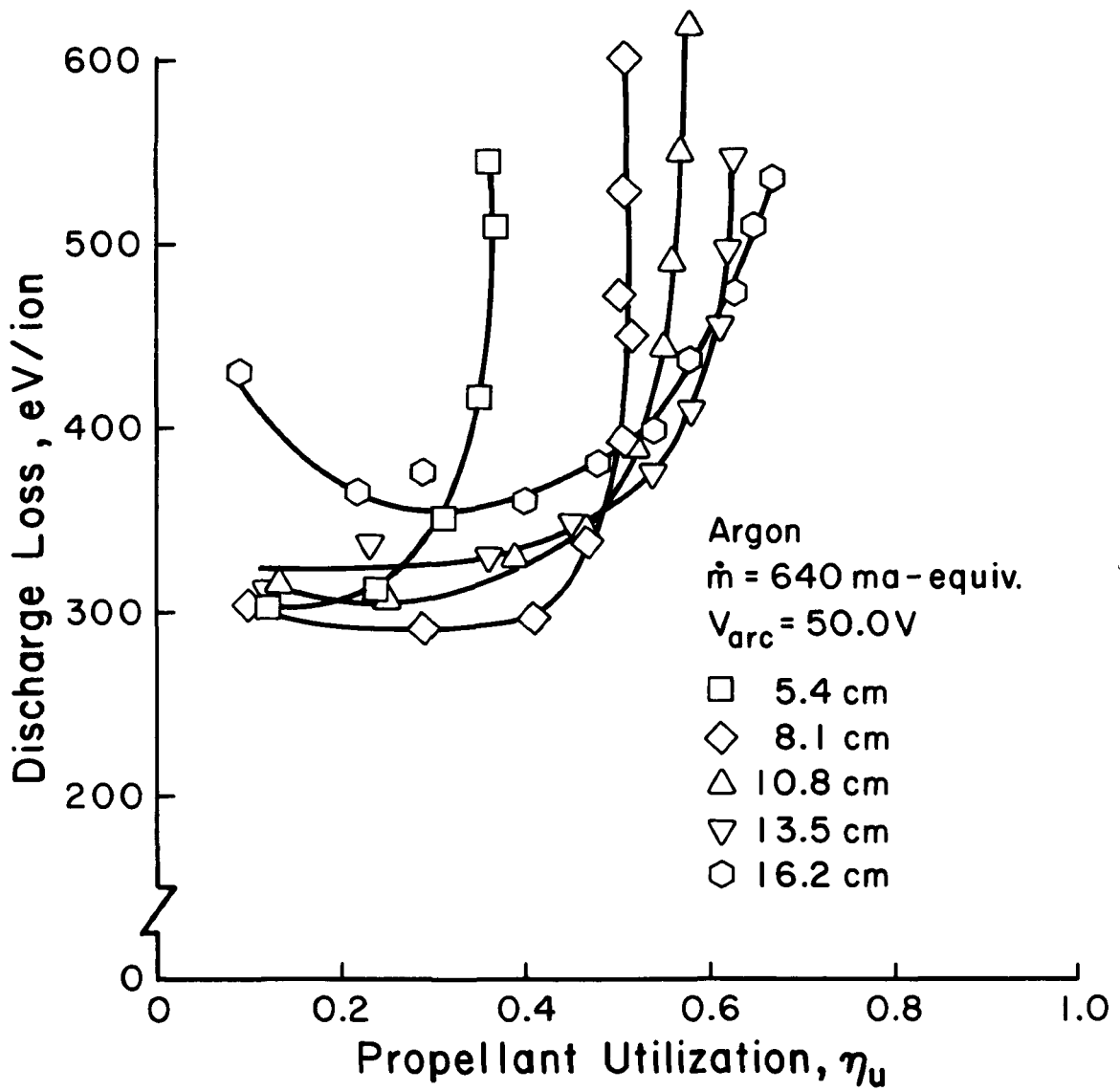


Figure 2-6. Effect of chamber length on discharge-chamber performance with argon propellant.

propellant. Minimum discharge losses decreased as the discharge-chamber length decreased from 16.2 cm to 8.1 cm, and then increased slightly at the 5.4 cm length. Operation was not possible with argon at the 2.7 cm length. The maximum utilization decreased continuously with a decrease in discharge-chamber length. Except for the increase in losses at the 5.4 cm length, these trends are in agreement with the classical variations with discharge-chamber length. That is, the longer chamber gives a higher probability of ionization (hence higher utilization), but it also gives a higher probability of ion recombination on the walls of the discharge chamber (hence higher discharge losses).

To obtain additional insight into the trends of Fig. 2-6, the neutral loss rates were calculated for the five chamber lengths using the method of Kaufman and Cohen<sup>9</sup> with a numerical value from the center of the scatter band given therein. This method gives a single neutral loss rate that should correspond to the "knee" of the discharge loss vs. utilization curve. Because the scatter band is quite large, close numerical agreement should not be expected. For argon in 5.4, 8.1, 10.8, 13.5, and 16.2 cm long chambers, the predicted loss rates were 0.486, 0.390, 0.343, 0.315, and 0.296 amperes-equivalent. For a neutral flow rate of 0.640 ampere-equivalent, these neutral loss rates correspond to knee utilizations of 0.24, 0.39, 0.46, 0.51, and 0.54. These predicted knee utilizations appear to be in good agreement with the experimental values.

Similar performance data obtained for xenon propellant are shown in Fig. 2-7. Again the minimum discharge losses decreased with chamber length from 16.2 to 8.1 cm, then increased when it was further shortened to 5.4 cm. Operation was possible at the 2.7 cm length with xenon and

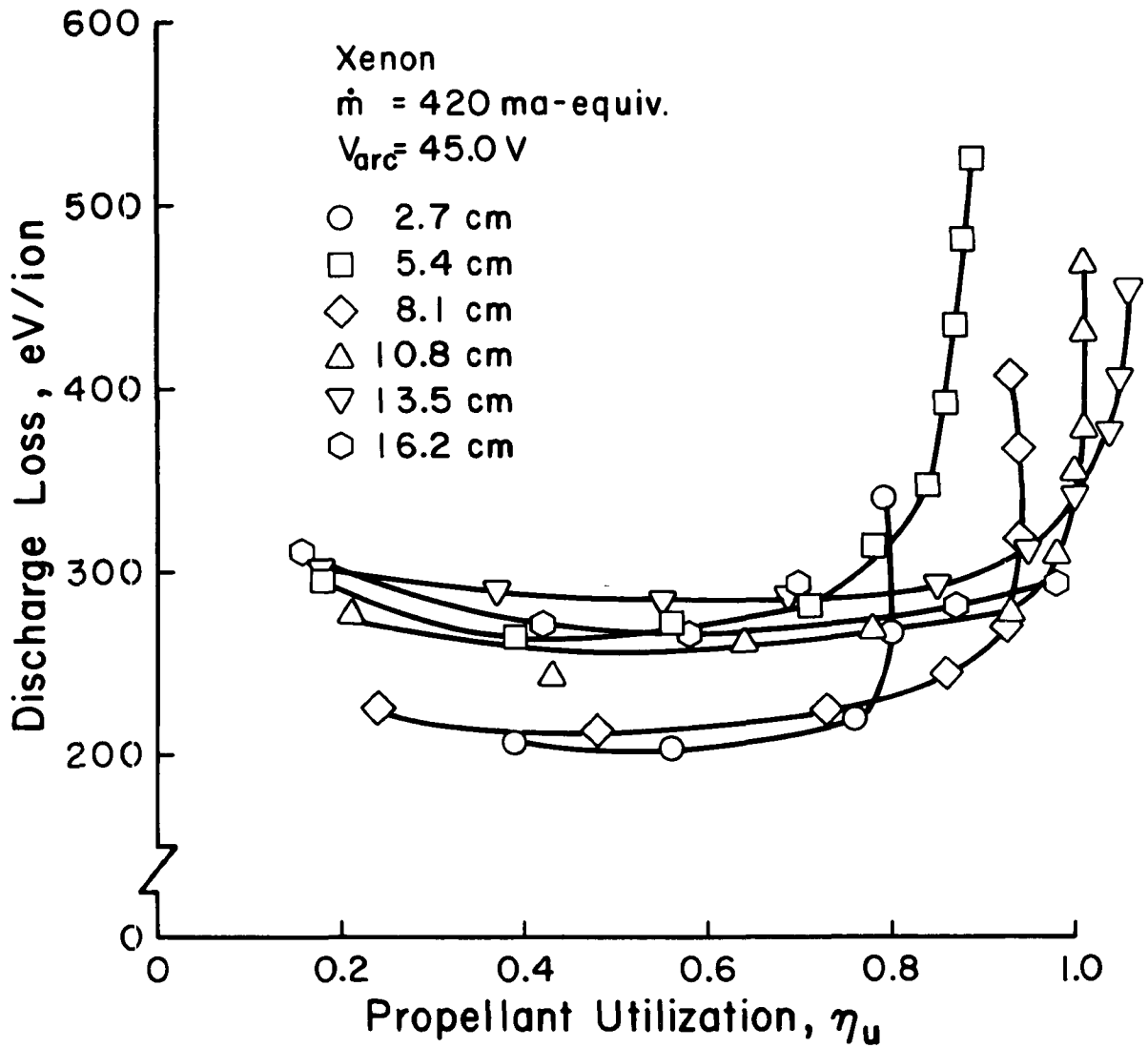


Figure 2-7. Effect of chamber length on discharge-chamber performance with xenon propellant.

resulted in the lowest discharge losses obtained. At this length, however, the discharge was unstable and subject to extinction from any perturbation. Except for the 16.2 cm length, which was constrained by a cathode emission limit, the maximum utilization again decreased with decreased discharge chamber length. Using the same procedure as with argon, the predicted loss rates were 0.141, 0.089, 0.071, 0.63, 0.057, and 0.054 ampere-equivalent for discharge-chamber lengths of 2.7, 5.4, 8.1, 10.8, 13.5, and 16.2 cm. For an 0.440 ampere-equivalent xenon flow rate, these neutral loss rates correspond to knee utilizations of 0.66, 0.79, 0.83, 0.85, 0.86, and 0.87. These predicted knee utilizations appear to be in reasonable agreement with experimental data. The discrepancy between predicted values and experimental data for the three longer chambers is due, at least in part, to insufficient correction for xenon double ions. Complete double-ion correction data were obtained only with the 8.1 cm chamber length. Because the double ion fraction will tend to increase with chamber length (note utilizations above 1.0 in Fig. 2-7), the use of data from the 8.1 cm length would be expected to result in too little correction for the longer chambers.

The increase in minimum discharge losses when going from an 8.1 cm length to a 5.4 cm length (both argon and xenon) and the decrease in going from 5.4 cm to 2.7 cm was not expected. It is believed that these particular trends result from the interaction of the main cathode with the fields above the anodes. That is, these trends would be expected to be modified if the cathode were relocated.

### Propellant Flow Rate

The effects of varying propellant flow rate were investigated using the 8.1 cm chamber length for both argon and xenon. Data were obtained over an approximately 3:1 range for both propellants. The argon data in Fig. 2-8 show increased discharge losses and decreased utilization as the propellant flow rate is decreased. The minimum discharge losses were about 300 eV/ion for the 0.922 and 1.534 ampere-equivalent flow rates. The higher discharge losses for the 0.416 and 0.622 ampere-equivalent flow rates were probably associated with the low maximum utilizations (~0.5) obtainable at these flow rates.

Similar flow rate data for xenon are presented in Fig. 2-9. The maximum utilization decreases with xenon flow rate, but the minimum discharge loss remains nearly constant at about 225 eV/ion.

### Ion Beam Profiles

Ion beam profiles were obtained in a plane 6.5 mm downstream of the center of the accelerator system and are shown in Figs. 2-10 and 2-11 for argon and xenon. These profiles are generally quite flat. The argon profile for the 5.4 cm length is the poorest, probably due to the accelerator system approaching the cathode. A similar central hump is evident for xenon with the 5.4 cm length. The flatness parameters shown in Figs. 2-10 and 2-11 are all calculated using the total beam area. Because the grids are dished, the probe is about 1.3 cm downstream at the edge of the beam, which gives room for radial expansion of the beam. If the flatness parameter were based on the accelerator-system diameter instead (15 cm), the flatness parameters would increase to about 0.85-0.90.

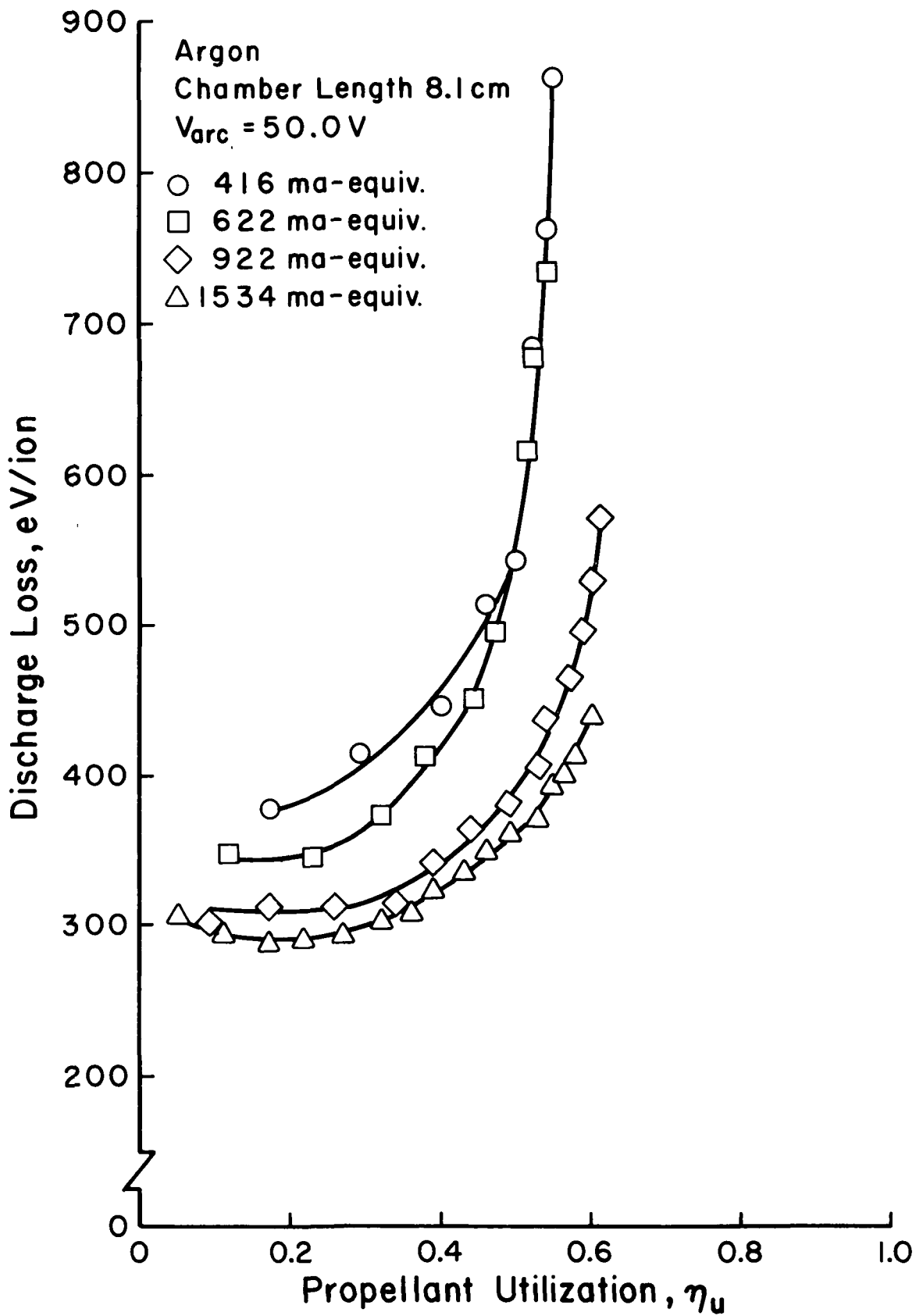


Figure 2-8. Effect of flow rate on discharge-chamber performance with argon propellant.

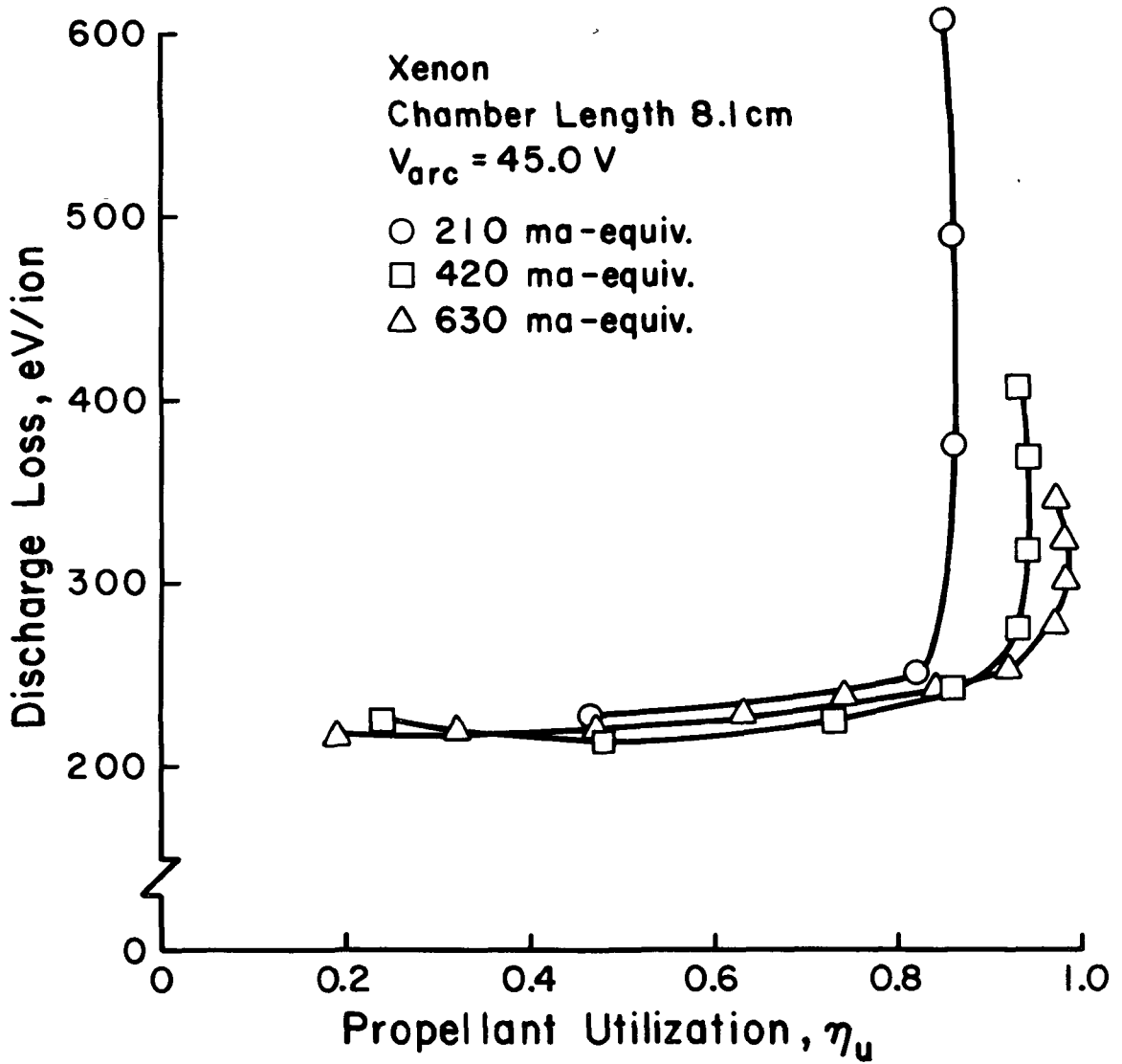


Figure 2-9. Effect of flow rate on discharge-chamber performance with xenon propellant.

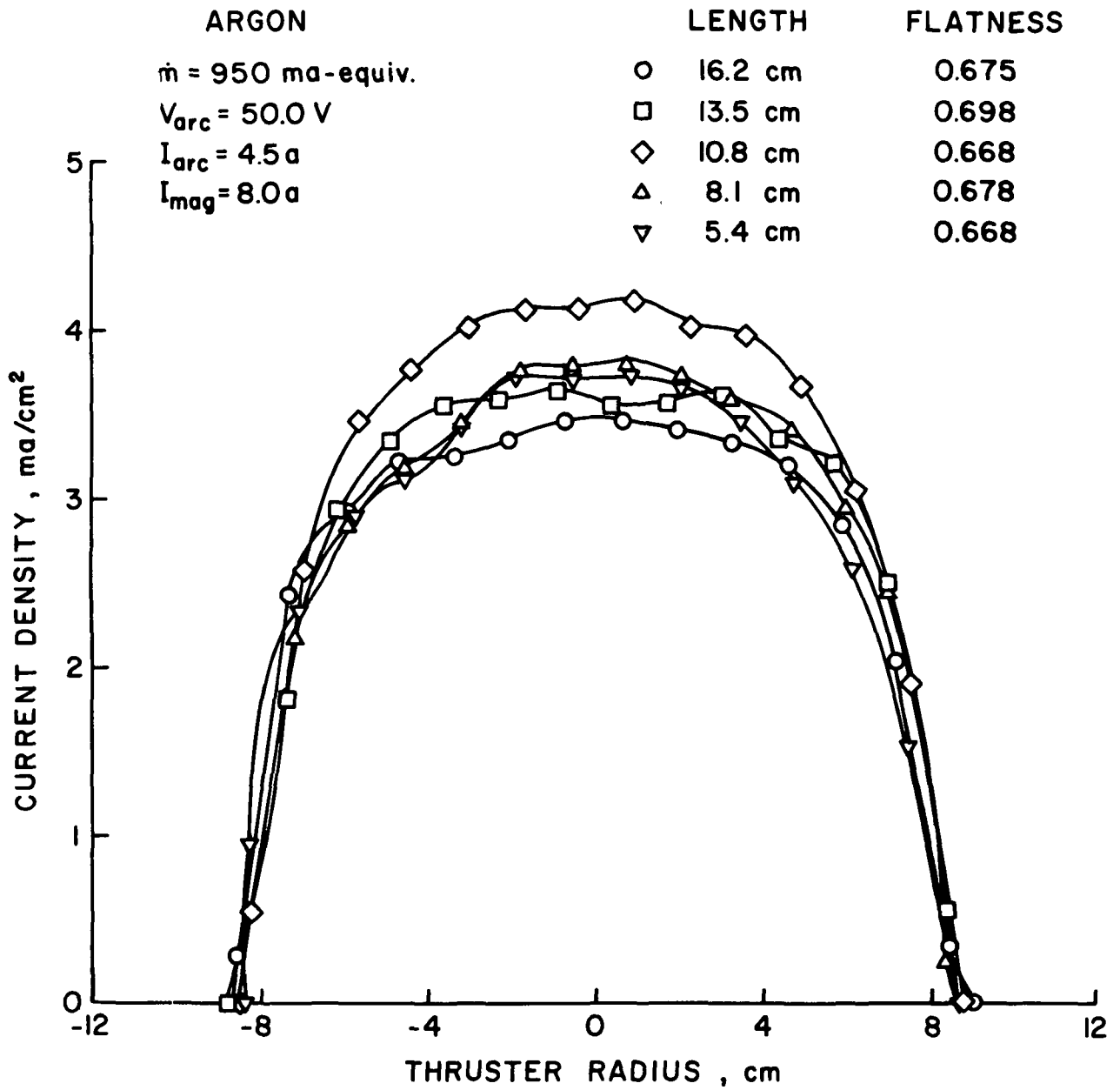


Figure 2-10. Ion beam profiles with argon propellant.

XENON		LENGTH	FLATNESS
$\dot{m} = 630 \text{ ma-equiv}$	○	16.2 cm	0.720
$V_{arc} = 45.0 \text{ V}$	□	13.5 cm	0.682
$I_{arc} = 3.0a$	◇	10.8 cm	0.783
$I_{mag} = 8.0a$	△	8.1 cm	0.734
	▽	5.4 cm	0.637

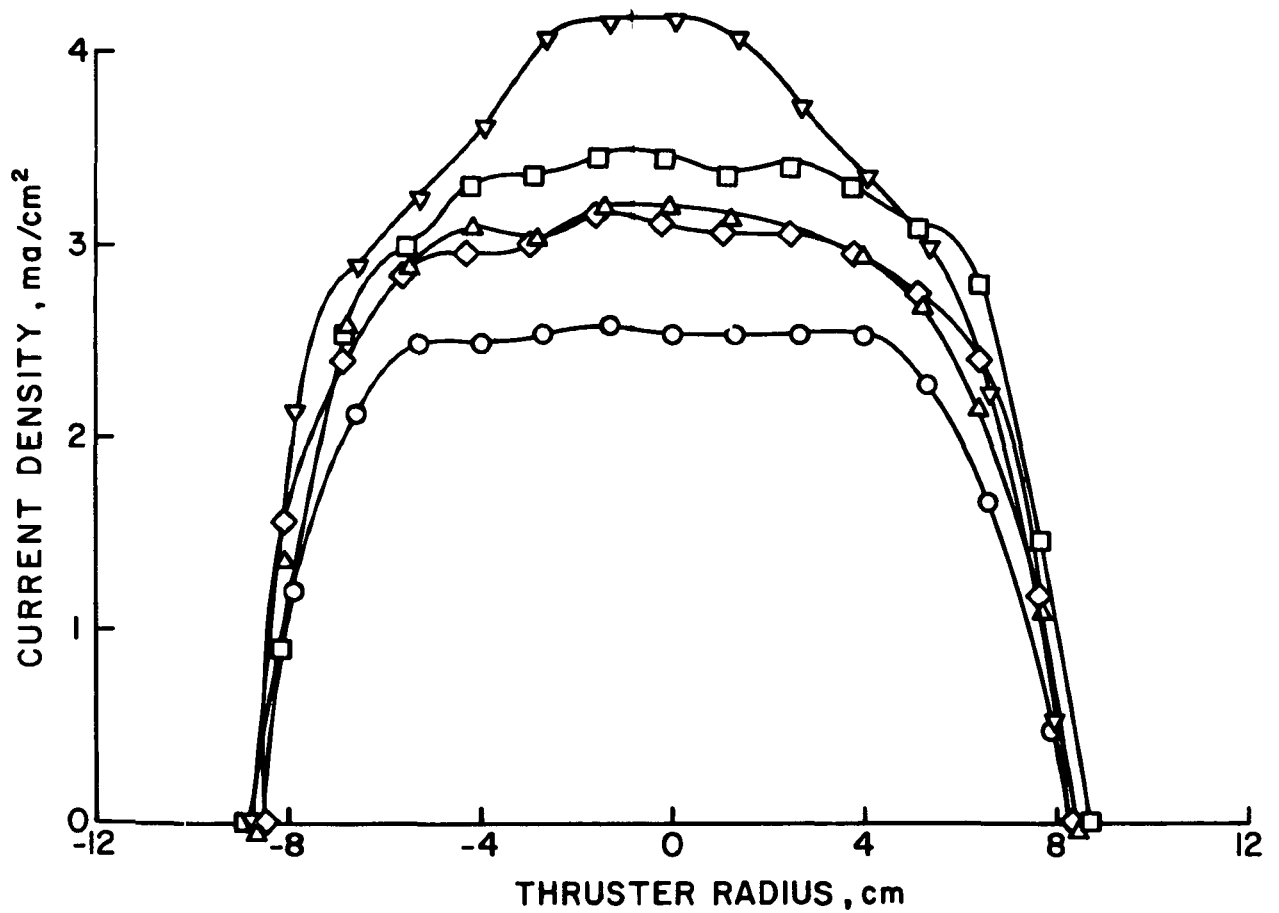


Figure 2-11. Ion beam profiles with xenon propellant.

These higher values are believed to be better indicators of the use of accelerator-system area. The decrease in flatness parameter downstream of the accelerator system is more a measure of the lack of beam collimation. The degree of collimation is, of course, not necessarily related to the beam flatness at the accelerator system.

### Performance Correlation

A wider range of chamber lengths was included in this investigation than in any recent study of discharge-chamber performance. The possibility of correlating performance for different lengths was therefore examined.

The value of the neutral-loss parameter,  $N_0 m_i \sigma (V_p/A_p)/A_0$ , in correlating "knee" performance<sup>9</sup> made it a promising candidate for a more general performance correlation. In the terminology of this report,  $N_0$  equals either  $I_b(1-\eta_u)/\eta_u$  or  $I_0(1-\eta_u)$ . Using the last form, the neutral loss parameter becomes  $I_0(1-\eta_u)m_i\sigma(V_p/A_p)/A_0$ . Inasmuch as the accelerator system was constant for all data, the effective open area  $A_0$  was omitted. Also, use of data for only one gas at a time permitted ion mass  $m_i$  and ionization cross section  $\sigma$  to both be omitted. These omissions left  $I_0(1-\eta_u)(V_p/A_p)$  where  $I_0$  is the total neutral flow rate in amperes and  $V_p/A_p$  is the ratio of volume to outside area for the primary electron region. In a multipole thruster, the primary electron region can be taken as the cylindrical volume enclosed by the accelerator system and the inside edges of the pole pieces and anodes. The ratio  $V_p/A_p$  is in meters.

For a discharge-loss parameter, some means of compensating for

changes in wall area (and associated wall losses) was required. The simplest approach was to multiply experimental discharge losses (eV/ion), by the ratio of beam area to primary electron region area,  $A_b/A_p$ . The distribution of actual losses is more complicated, but the use of this simple area ratio might be expected to give a first-order correction.

The ion chamber data for both argon and xenon over a range of flow rates and with all chamber lengths are plotted in Figs. 2-12 and 2-13. It is evident that these parameters give a reasonable degree of data correlation for both propellants.

The expected neutral losses for the discharge-loss "knee" were calculated using the method of Kaufman and Cohen.<sup>9</sup> The results corresponded to neutral-loss parameters of 0.0077 for argon in Fig. 2-12 and 0.0014 for xenon in Fig. 2-13. These values are in good agreement with the curve shape shown.

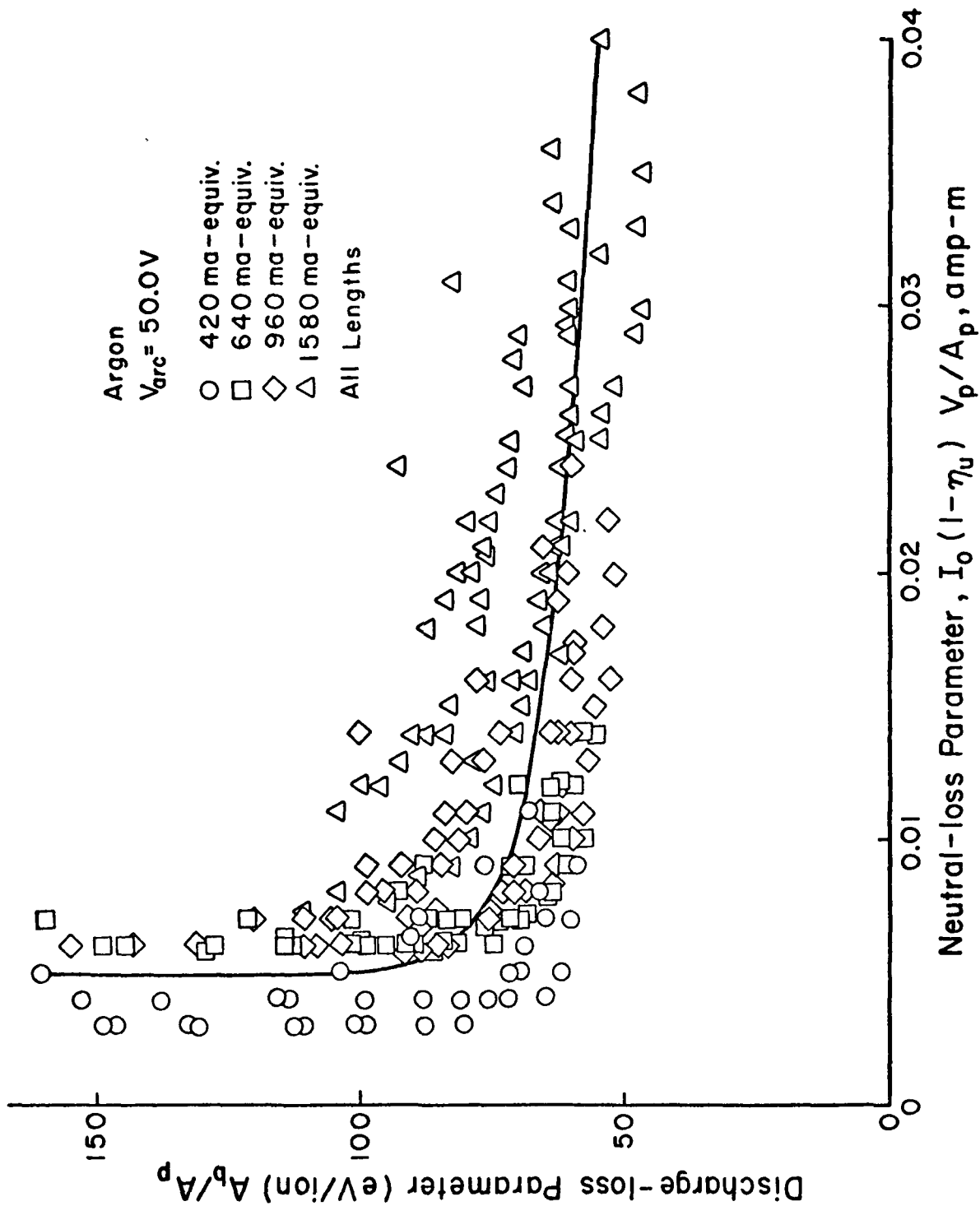


Figure 2-12. Performance correlation for all discharge-chamber lengths and all flow rates with argon propellant.

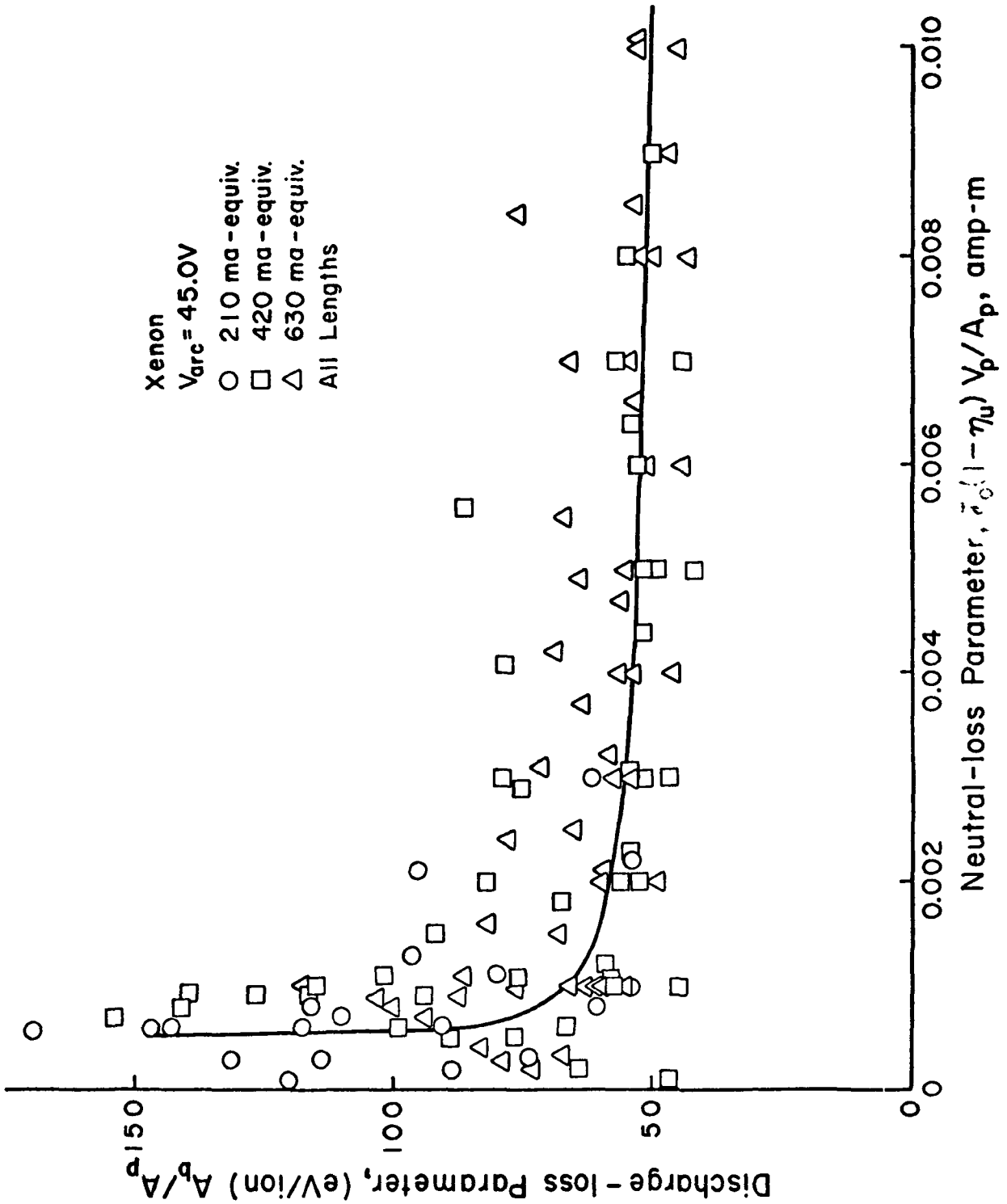


Figure 2-13. Performance correlation for all discharge-chamber lengths and all flow rates with xenon propellants.

### III - ELECTRON DEFLECTION IN A SPATIALLY VARYING MAGNETIC INDUCTION

by Raymond S. Robinson

In a multipole ion source, primary electrons are prevented from escaping to the anodes, before expending most of their energy producing ions, by a fringe magnetic field in the region adjacent to the anodes. In calculating the deflection of an electron in such a fringe field, it is assumed that in the region of interest the radius of curvature of the anode is large compared to the depth of the field involved and that the magnitude of the magnetic induction  $B$  varies arbitrarily as a function of the distance from the anode. It is further assumed that  $\bar{B}$  is parallel to the anode surface in the region of interest.

In passing through an infinitesimal region  $dx$ , an electron with a component of velocity  $v$ , perpendicular to  $\bar{B}$ , is deflected through an angle  $d\theta$  -- as indicated in Figure 3-1. The radius of curvature of the electron path in the region  $dx$  is

$$r = \frac{mv}{qB(x)}$$

where  $m$  and  $q$  are the mass and charge of an electron. From geometrical considerations, the radius  $r$  can be related to  $d\theta$  and  $dx$ .

$$r d\theta = \frac{dx}{\sin\theta}$$

The radius  $r$  can be eliminated between these two expressions.

$$B(x) dx = \left[ \frac{mv}{q} \right] \sin\theta d\theta$$

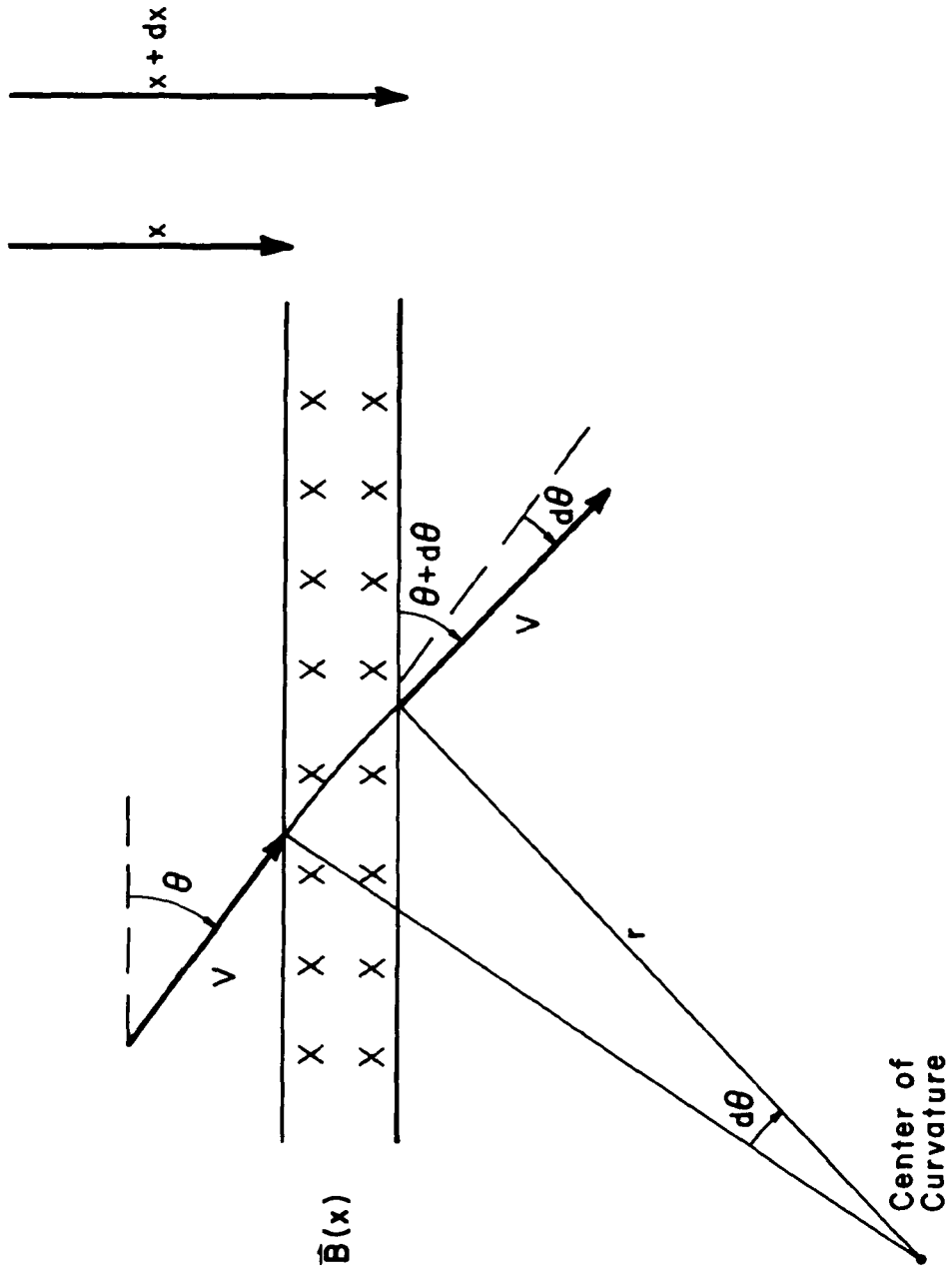


Figure 3-1. Electron deflection in magnetic field.

The integral of  $B(x)dx$  can now be related to electron deflection,

$$\int_0^D B(x) dx = \int_{\theta_i}^{\theta_f} \left[ \frac{mv}{q} \right] \sin\theta d\theta$$

where  $\theta_i$  is the incident electron angle and  $\theta_f$  is the angle after the electron traverses a thickness  $D$  of magnetic induction. The maximum value of the angular integral corresponds to the maximum electron penetration toward the anode, and is obtained with  $\theta_i = 0$  and  $\theta_f = \pi$ . The angular integral can be evaluated for these limits

$$\int_0^D B(x) dx = \frac{2mv}{q}$$

or, in terms of electron kinetic energy,  $E$ ,

$$\int_0^D B(x) dx = 2\sqrt{\frac{2m}{q^2}} \sqrt{E}$$

With the substitution for electron charge and mass this becomes

$$\int_0^D B(x) dx = 6.74 \times 10^{-6} \sqrt{E}$$

if  $E$  is measured in electron volts and the left hand side is in MKS units. This expression then provides a criterion on the integrated field for primary electron containment.

#### IV - ARGON HOLLOW CATHODE

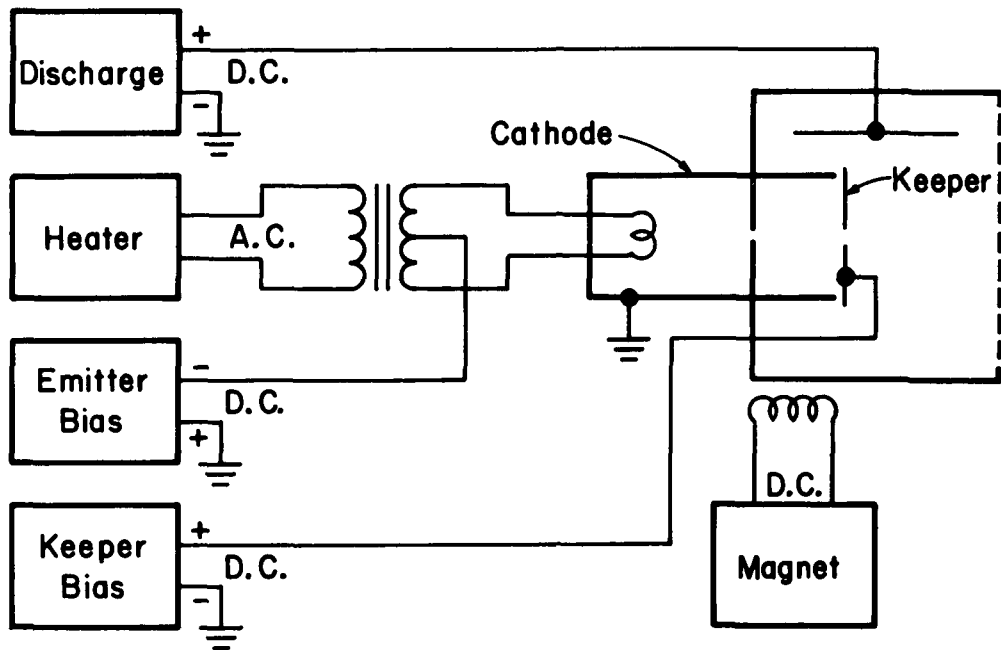
by Larry A. Rehn

The major objective of this study was the development of a long life hollow cathode. A secondary objective was ease and reliability of starting. Argon was emphasized in this study because it is of great interest and is a greater departure than xenon from the usual thruster propellants of cesium and mercury.

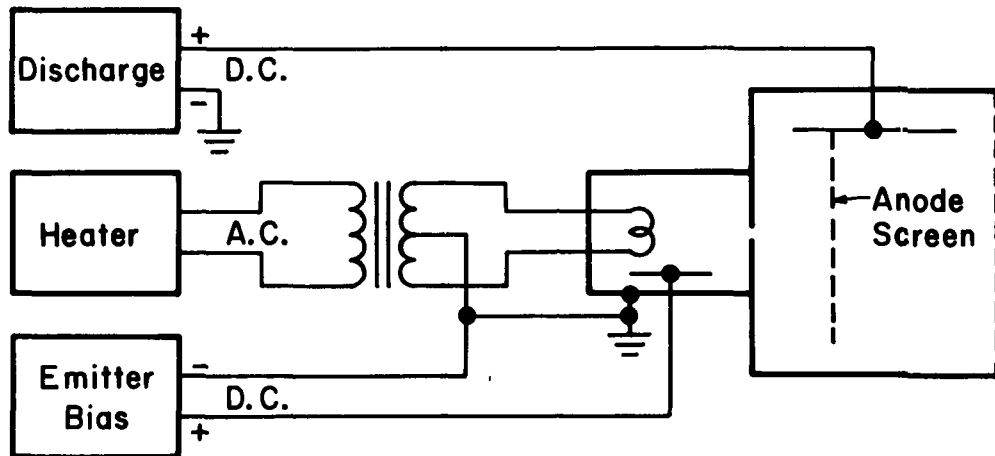
An internal thermionic emitter of tungsten was selected for this study. Hopefully, a thermionic emitter could have a longer lifetime inside a hollow cathode than exposed to the ion-chamber discharge. If so, the internal emitter would also facilitate starting without high voltage. Another important reason for the selection of an internal emitter, though, was to obtain reproducible emission characteristics without the coating and conditioning problems of barium-strontium oxides.

Cathode discharge currents were limited in this study to less than about 5 amperes. This level is sufficient for a main discharge of a 15-20 cm source, or the neutralizer of a 30 cm source.

Initial tests were conducted in a 30-cm bell jar facility, while later tests used one with a 45-cm bell jar. Although both facilities employed 15-cm diffusion pumps, the larger facility gave nearly a factor of ten lower pressure. The major components of the electrical system are indicated in Fig. 4-1. The thruster simulator was a complete 15-cm axial field thruster, except that no accelerator grid or neutralizer were included. When the electromagnet was used, the magnetic field was sufficient to keep primary electrons from directly reaching the anode. Higher field strengths gave no significant difference in cathode performance. Calculations indicated that the screen grid blockage should



(a) All Cathodes Except Discharge-Chamber Cathode.



(b) Discharge-Chamber Cathode.

Figure 4-1 Power supply block diagram. The use of the enclosed keeper, screen anode, and discharge chamber magnet were optional. The screen anode was used with the other cathodes, but always with the discharge chamber electromagnet turned off.

result in a discharge chamber pressure 1.55-2.0 times the ambient bell jar pressure (1000-500 ma-equivalent of argon). The bell jar pressures, when given, are therefore indicative of discharge-chamber pressure.

The cathode assemblies are all cylindrical, but otherwise varied widely in configuration. Except for the magnetic orifice and discharge chamber cathodes, they were functionally similar to the version shown attached to the thruster simulator in Fig. 4-2. Diameters varied from 0.64 cm to 7.6 cm, while lengths were maintained at about 3.8 cm. Tungsten wire with a diameter of 0.25 mm was used for all emitters. Emitter length was 3.5-4.0 cm except for the 0.64 cm diameter, which used a 2.5 cm length. The emitter connections were made through the back (upstream) wall in all configurations except the 0.64 cm diameter, where the connections were made in the side (cylindrical) wall. Propellant feed was through the back wall in all tests. In most configurations the orifice plate was 1 mm thick tantalum, 5 cm in diameter. Eight mounting screws permitted the rapid replacement of this plate for a change in orifice hole size.

#### Test Environment Effects

The effect of bell jar pressure,  $P_{bj}$ , on cathode performance is shown in Fig. 4-3. The pressure difference was due to the use of two different vacuum facilities, as discussed earlier. The cathode configuration used was similar to that shown in Fig. 4-2, with the circuit the same as Fig. 4-1(a) except that no keeper was used. Although the orifice diameters and flow rates were not the same, the difference in discharge characteristics was typical for the two facilities. Most data were obtained in the lower pressure facility and typically showed the same sharp rise in

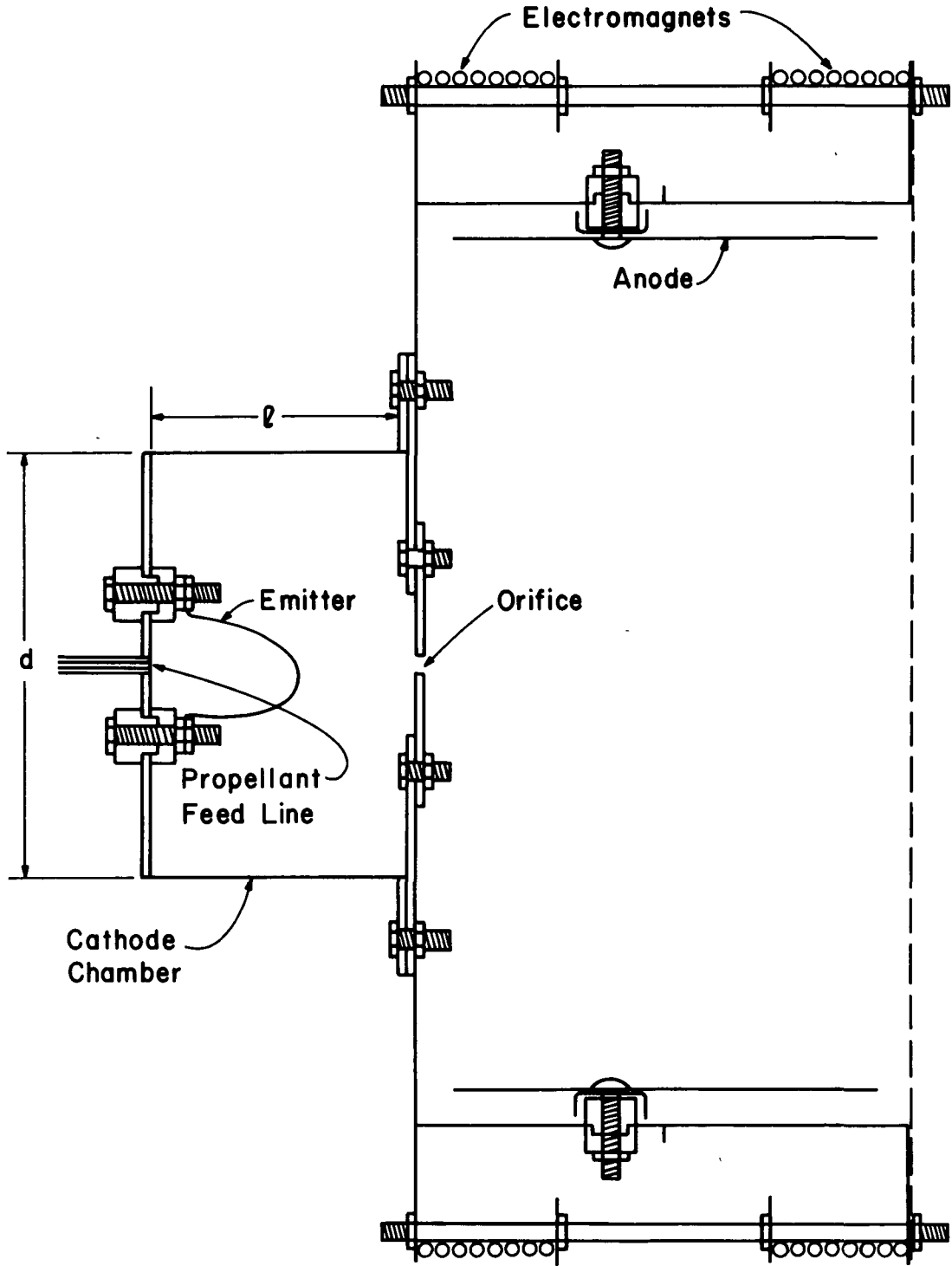


Figure 4-2. Sketch of hollow cathode and discharge chamber assembly.

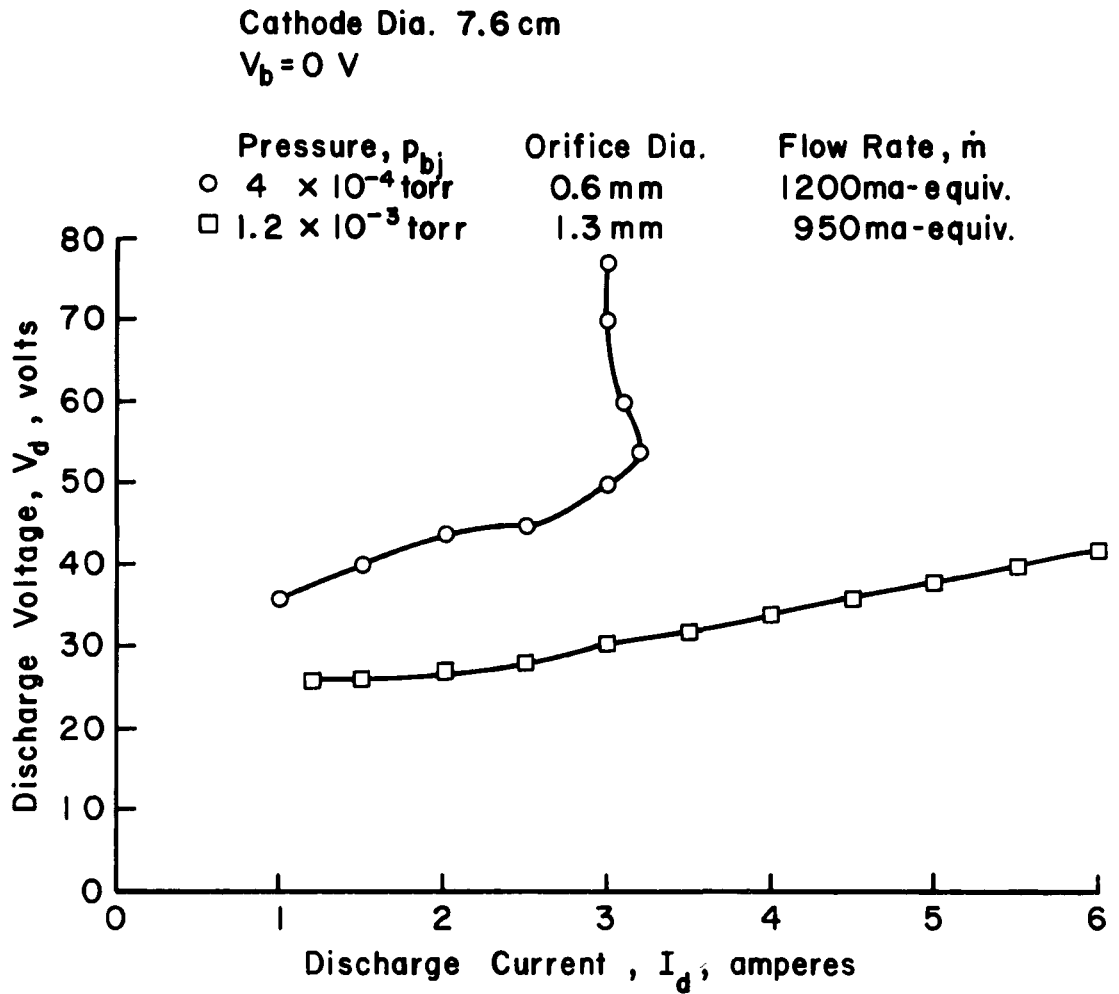


Figure 4-3. Effect of bell jar (background) pressure on cathode performance. Without screen anode.

voltage at some discharge current.

Cathodes were operated both with the simulated thruster as indicated in Fig. 4-2 and with an additional 7-mesh/cm stainless-steel screen anode (indicated schematically in Fig. 4-1(b)) to simulate neutralizer operation. When used, the screen was electrically connected to the cylindrical anode in the thruster simulator. The screen was about 5 cm square and located about 2.5 cm downstream of the cathode (or keeper, when used). No magnet current was used with a screen anode.

The effect of using the screen anode is shown in Fig. 4-4. A non-zero bias voltage,  $V_b$ , was used, but the results shown in Fig. 4-4 are typical for all comparisons of data with and without screen anodes. The use of a screen anode resulted in higher discharge currents at all discharge voltages. The decreased anode-cathode distance and the absence of a magnetic field (or decreased strength thereof) probably contributed to the current increase with a screen anode. Part of the increase may also be due to an increase in pressure upstream of the screen, but this effect should be small because the open area fraction of the screen used was nearly 0.7.

Long life cathodes require low discharge voltages. It is true that discharge chamber potential differences of 40-50 volts may be required for efficient ionization, but the immediate environment of the cathode should be much closer to cathode potential if a long life is to be obtained. There is no "pole piece" or equivalent cathode protection in the simulated thruster of Fig. 4-2. Lower voltage operation at the same discharge current is therefore more desirable or better for the cathode. The terms "better" or "best" will be used throughout to describe such a voltage decrease. The incorporation of cathode protection into an actual thruster

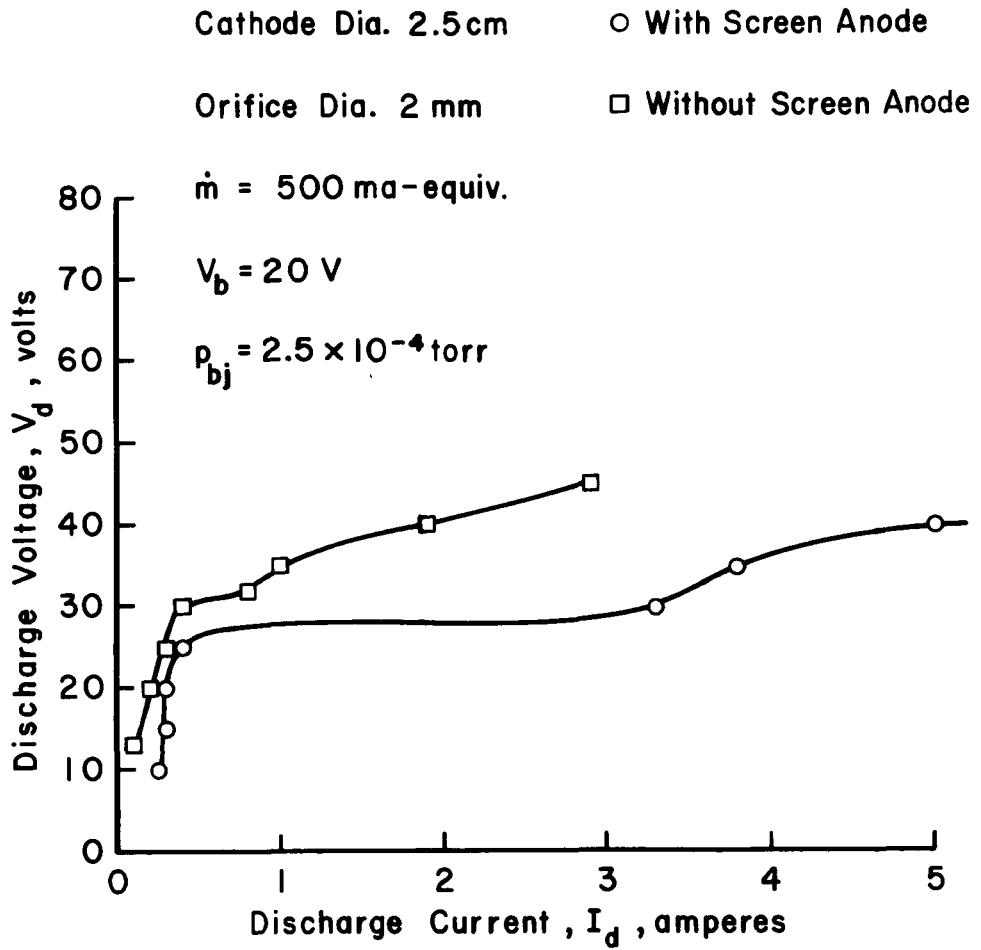


Figure 4-4. Effect of using a stainless steel screen anode, located 2.5 cm from the orifice vs. a conventional discharge-chamber anode.

is important, but it is less pressing than the development of the cathode.

Emission calibration proved to be a recurrent problem. Tungsten wire of a constant diameter was used in all tests, with the emitter length the same in all except the smallest cathode chamber diameter. It was initially hoped that these precautions, together with the use of a constant heater current would serve to provide a constant emission. But sufficient emitter erosion (due to ion bombardment and/or the effects of impurities initially present) occurred so that constant heating current resulted in substantial increases in electron emission during some of the tests.

As the next calibration technique, a bias discharge between the emitter and cathode chamber wall was utilized. After establishing an internal discharge, the emitter bias voltage was reduced until the discharge was extinguished. The discharge was then re-established with the bias 5 volts above this minimum value for a discharge. The emitter heater current was then adjusted until the emission was some standard value, typically 1 ampere. This calibration approach was an improvement over the use of a constant heating current through a constant length cathode. But it still had several shortcomings. In some cases, the internal discharge would slowly dwindle to zero as bias voltage was reduced, leaving no clear reference point for calibration. The variation of internal discharge with emitter heater current is shown in Fig. 4-5. Note that the minimum bias voltage for a discharge varies with heater current.

As a final calibration method for this study, entire emitter performance curves were taken - as shown in Figs. 4-5 and 4-6. An initial curve at 7 amperes heating current served as a calibration for each configuration. As time passed during each run, these data were retaken and the heating

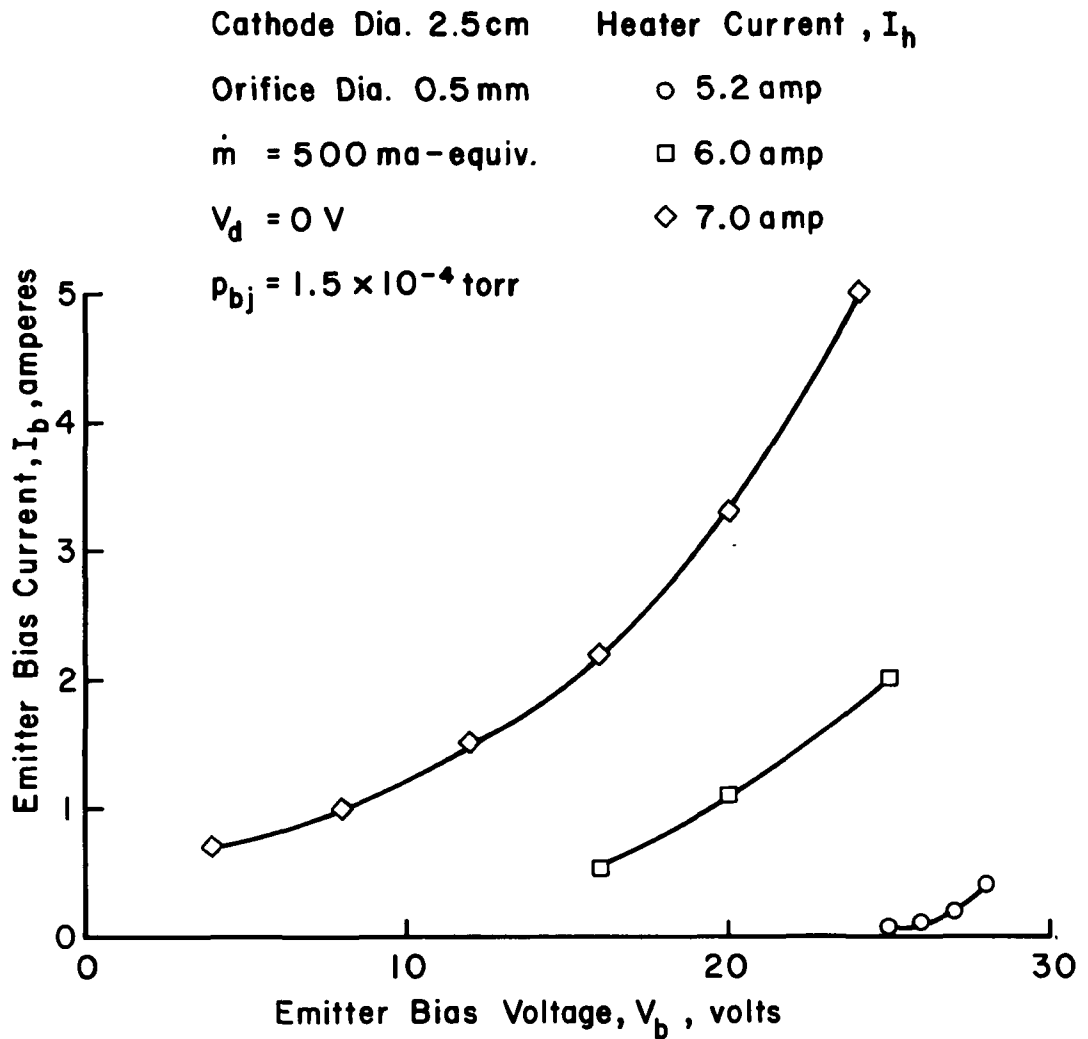


Figure 4-5. Effect of heater current changes on cathode emission. Without screen anode.

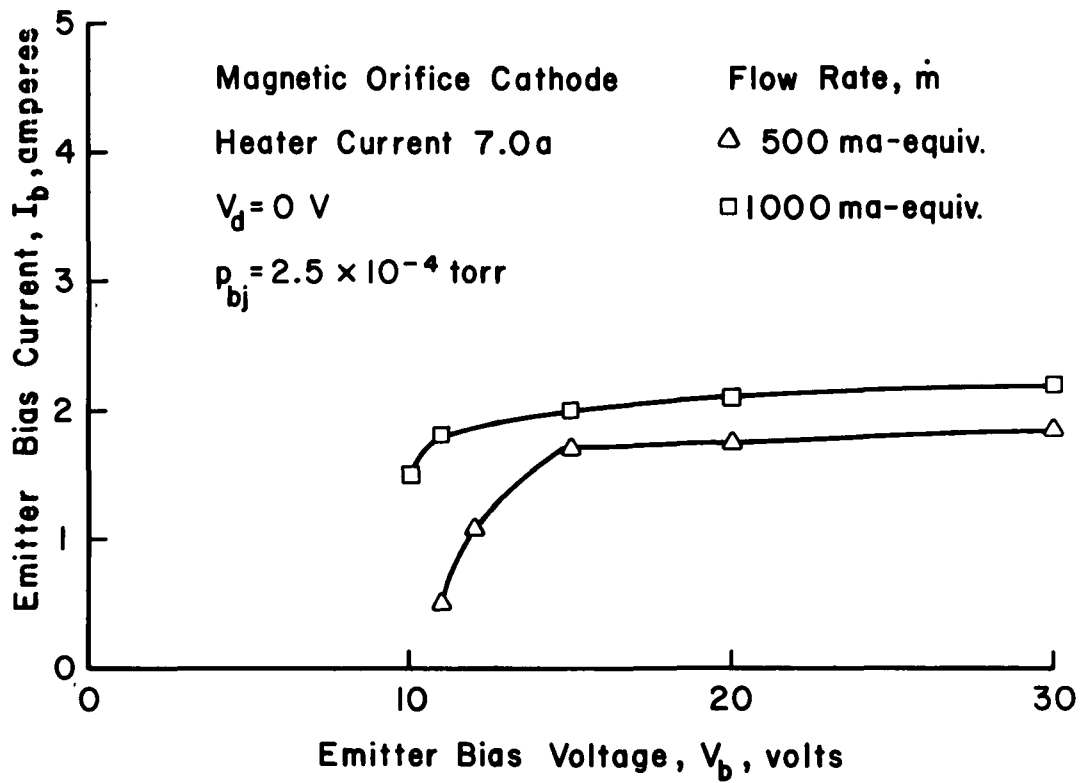


Figure 4-6. Effect of propellant flow changes on cathode emission. With screen anode.

current adjusted to give a discharge curve close to the original one obtained at 7 amperes. It is felt that this procedure corrects for most of the changes in emission that would otherwise take place with time.

#### Cathode Size Effect

Inasmuch as both volume and surface losses tend to increase with plasma size, cathode performance was expected to improve with a decrease in cathode chamber size. The initial intent of the size investigation was to determine the penalty for a size increase. A size increase over the usual 3 and 6 mm mercury hollow cathodes would, of course, ease fabrication problems for more complex geometries, as well as provide more radiation area for cooler operation.

The results of varying cathode chamber diameter are shown in Fig. 4-7. Instead of the expected monotonic improvement in performance with decreased size, a broad optimum was found from about 1 to 2.5 cm in diameter. The nearly horizontal curves of the intermediate diameters would, from other data, be expected to show sharp rises in voltage if they had been extended to higher discharge currents. The 2.5 cm data apparently shows the beginning of this expected rise at 5 to 6 amperes of discharge current.

The cathode chamber length was kept nearly constant at 3.5 to 4 cm as mentioned earlier. The 0.64 cm diameter chamber therefore had a large length-to-diameter ratio. To make sure that this large ratio was not the cause of poorer performance of this diameter, an additional test (not shown) was conducted with the length cut in half. No significant performance difference was found for these two lengths of 0.64 cm diameter.

From Fig. 4-7, then, it appears that argon hollow cathodes should be larger in diameter than the sizes customarily employed for mercury hollow

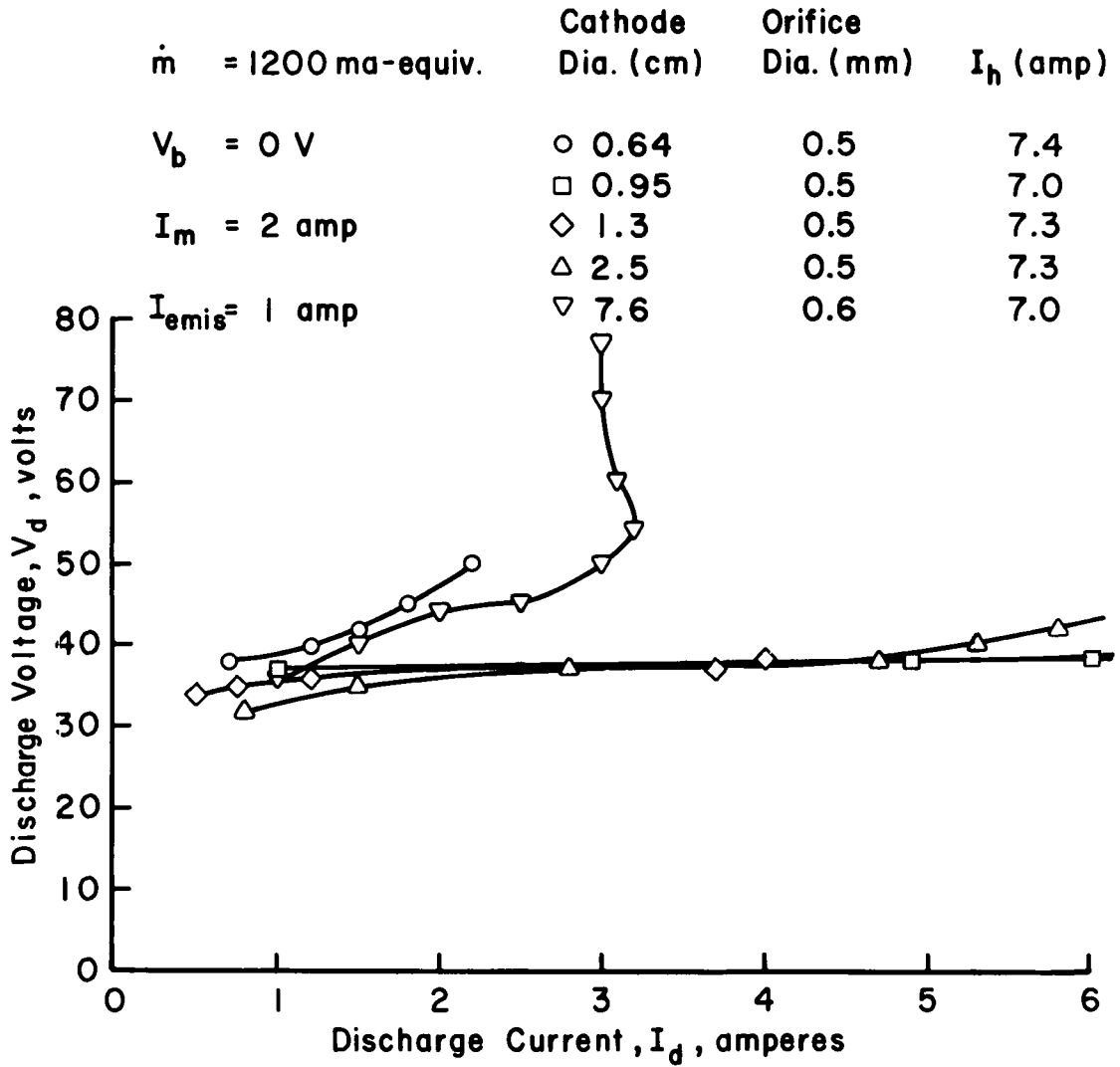


Figure 4-7. Survey of cathode performance as a function of cathode chamber diameter. Without screen anode.

cathodes. This result is significant in that room can be made available for more complex electrode geometries without paying a performance penalty for the increased size. On the other hand, all the data in Fig. 4-7 were obtained at discharge voltages above 30. From endurance tests of hollow cathodes, a substantial reduction of discharge voltage would be required for the orifice of an argon hollow cathode to have thousands of hours of life.

#### Enclosed Keeper

Several modifications to the basic design were investigated as possible means for reducing the discharge voltage. The use of an enclosed keeper was one of these modifications. A cathode chamber diameter of 0.64 cm was selected because promising results had been obtained elsewhere in preliminary tests with this size using an enclosed keeper and an oxide-impregnated insert. These preliminary tests were obtained with the cathode operating as a neutralizer, so the screen anode was used herein to simulate neutralizer operation.

Data obtained with an enclosed keeper are shown in Fig. 4-8. The discharge voltage remained above 30 with a keeper, while no significant increase in discharge current was found. In fact, an increase in the keeper current resulted in a decrease of maximum discharge current. The keeper tended to float at about 12 volts. As the keeper was increased to 16 volts, the maximum discharge current was decreased by about the increase in keeper current.

The performance with a keeper was disappointing in that all operation was above 30 volts. This result differed sharply from thruster performance at Lewis. The only significant difference in configuration

Cathode Dia. 0.64 cm

Orifice Dia. 0.5 mm

$\dot{m} = 1200$  ma-equiv.

Keeper Voltage,  $V_k$

$V_b = 0V$

○ 12 V

$p_{bj} \approx 6 \times 10^{-4}$  torr

□ 18 V

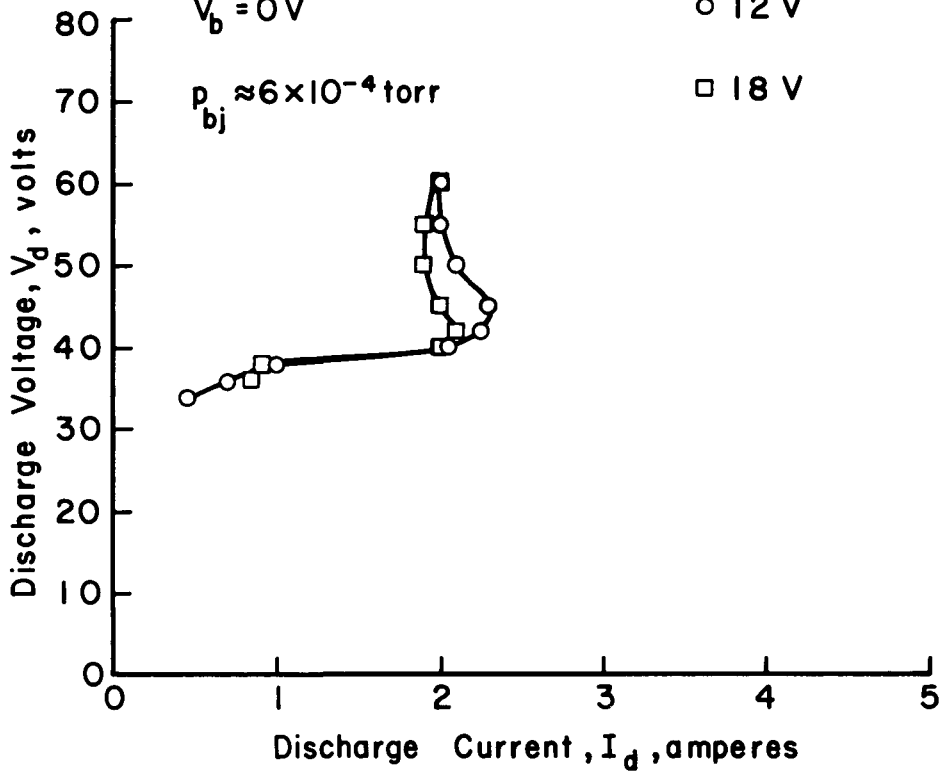


Figure 4-8. Performance with an enclosed keeper. The keeper was 1.3 cm from the cathode and had an orifice diameter of 0.76 mm. With screen anode.

appeared to be the use of a refractory emitter instead of an oxide-impregnated insert.

#### Effect of Barium-Strontium Oxides

Operation with an enclosed keeper, described above, resulted in substantially higher voltages than obtained in thrusters. Because the presence of oxides appeared to be the only significant difference, tests were conducted herein with a commercial barium-strontium oxide mix (R-500, J.T. Baker Chemical Co.). A small amount of this mix was injected (as carbonates with a volatile carrier) into the 0.64 cm cathode chamber near the orifice.

As shown in Fig. 4-9, the use of oxides resulted in a substantial increase in discharge current. The normal function of oxides is to decrease the surface work function, thereby increasing the emission at a given temperature. But the thermionic emitter used herein operated at a high enough temperature to rapidly vaporize any barium-strontium oxides that contacted it. The major cause of the performance difference with oxides is believed to be vaporized oxides mixed with the argon, thereby providing a small fraction of low ionization potential atoms.

It is tentatively suggested, then, that the lower voltages obtained at Lewis resulted from "seeding" the argon with barium-strontium oxides. Depletion of oxide impregnated inserts could be a problem if seeding is the cause of the of the performance difference - rather than some other parameter such as background pressure.

#### Comparison of Xenon and Argon

As mentioned at the beginning of the hollow cathode section, most tests were conducted with argon as the propellant. A few tests were

Cathode Dia. 0.64 cm

○ With Ba,Sr Oxides

Orifice Dia. 0.5 mm

□ No Oxides

$\dot{m} = 1200$  ma-equiv.

$V_b = 0$  V

$V_k = 10$  V (Oxide),  $12$  V (No Oxide)

$p_{bj} \approx 5 \times 10^{-4}$  torr

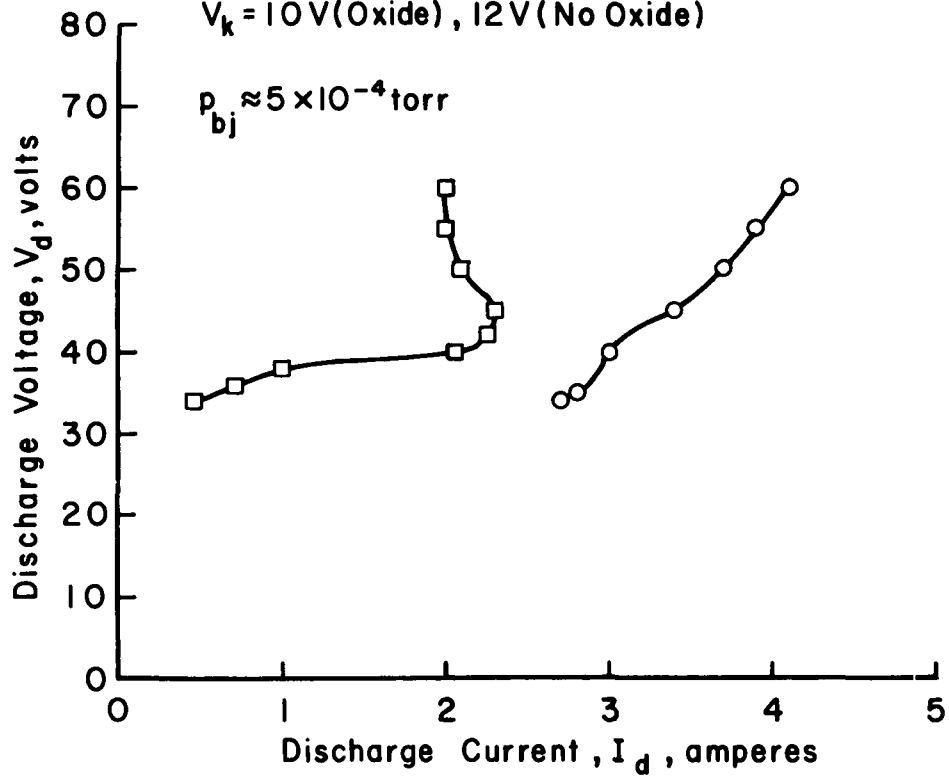


Figure 4-9. Performance comparison with and without barium-strontium oxides. With screen anode.

conducted with xenon, though, for comparison with argon data. Data from these tests are shown in Figure 4-10. The xenon performance curves have the same general shape as the argon curves shown previously. The specific performance values, however, are better for xenon. For example, xenon at 500 ma-equivalent has about the same corrected bell jar pressure as argon at 1000 ma-equivalent. (Note that the pressures in all figures are indicated pressures, and must be reduced by a factor of 1.1 for argon and 2.5 for xenon.) But the discharge current can operate over a wider range with xenon.

The better performance with xenon should be expected from the lower ionization potential, the larger ionization cross section, and the higher atomic weight. The latter results in a higher neutral density for the same ma-equivalent flow rate as argon. In general, wider ranges in discharge current are possible with xenon, while the discharge voltages are up to 10 V lower.

#### Orifice Size Effect

Another parameter investigated was that of orifice diameter. Figs. 4-11 and 4-12 show the effects of changing orifice size at high and low bell jar pressure. Although a screen anode is used for the low pressure data, the differences between Figs. 4-11 and 4-12 are similar to the differences shown for high and low pressure data in Fig. 4-3. The low pressure data should be more representative of a thruster environment, so that considerations of optimum orifice size will be restricted to Fig. 4-12. For discharge currents of 3 to 5 amperes, the 0.5 mm orifice resulted in the lowest discharge voltage. At lower discharge currents, the 2 and 5 mm orifices result in the lowest discharge voltages. It is not clear why the 1 mm orifice has the highest discharge voltage over much of the current range.

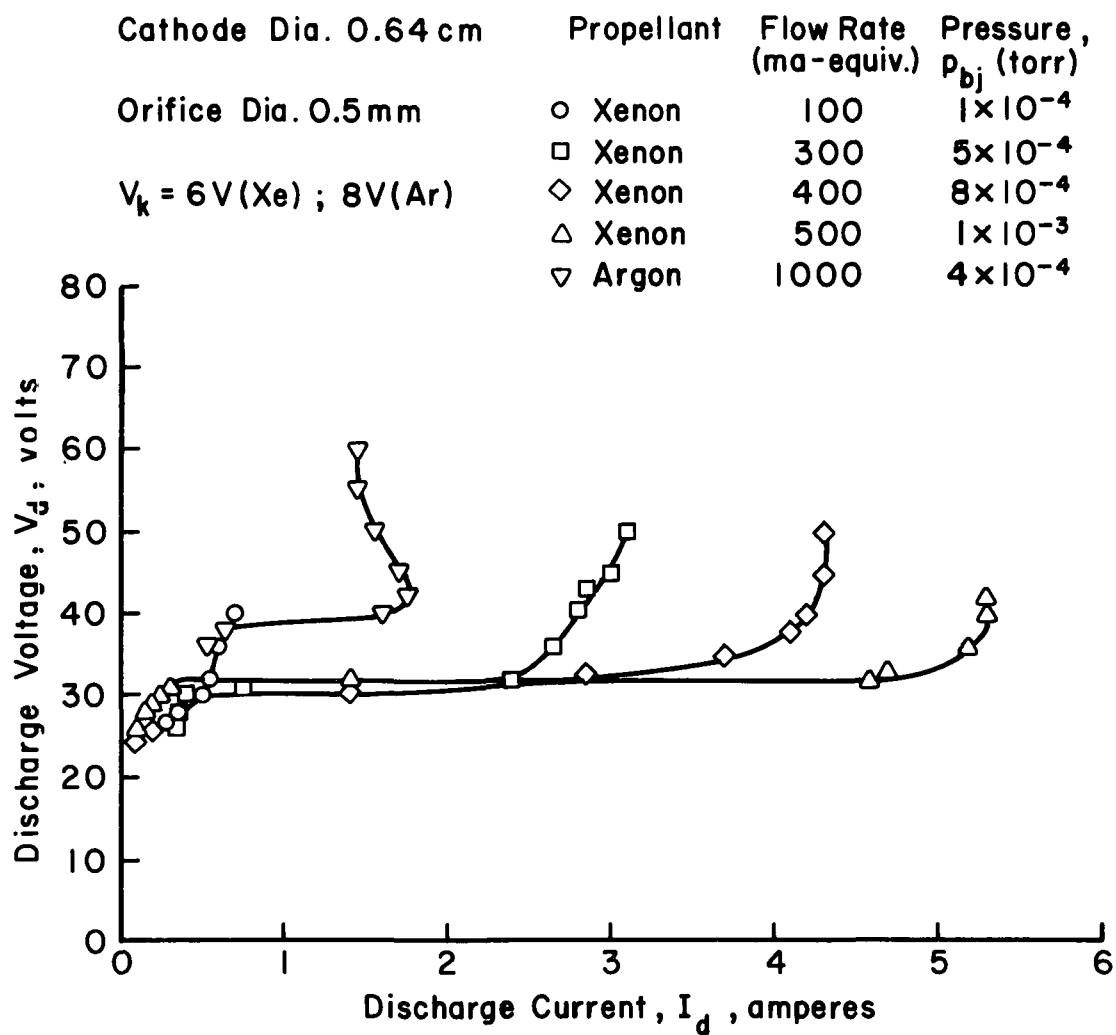


Figure 4-10. Comparison of argon and xenon performance with several flow rates of xenon used. With screen anode.

Cathode Dia. 7.6 cm

Orifice Dia. (mm)

$\dot{m} = 700 \text{ ma-equiv.}$

$V_b = 0 \text{ V}$

$p_{bj} \approx 9 \times 10^{-4} \text{ torr}$

● 1.3

▽ 3.0

△ 5.0

◆ 10.0

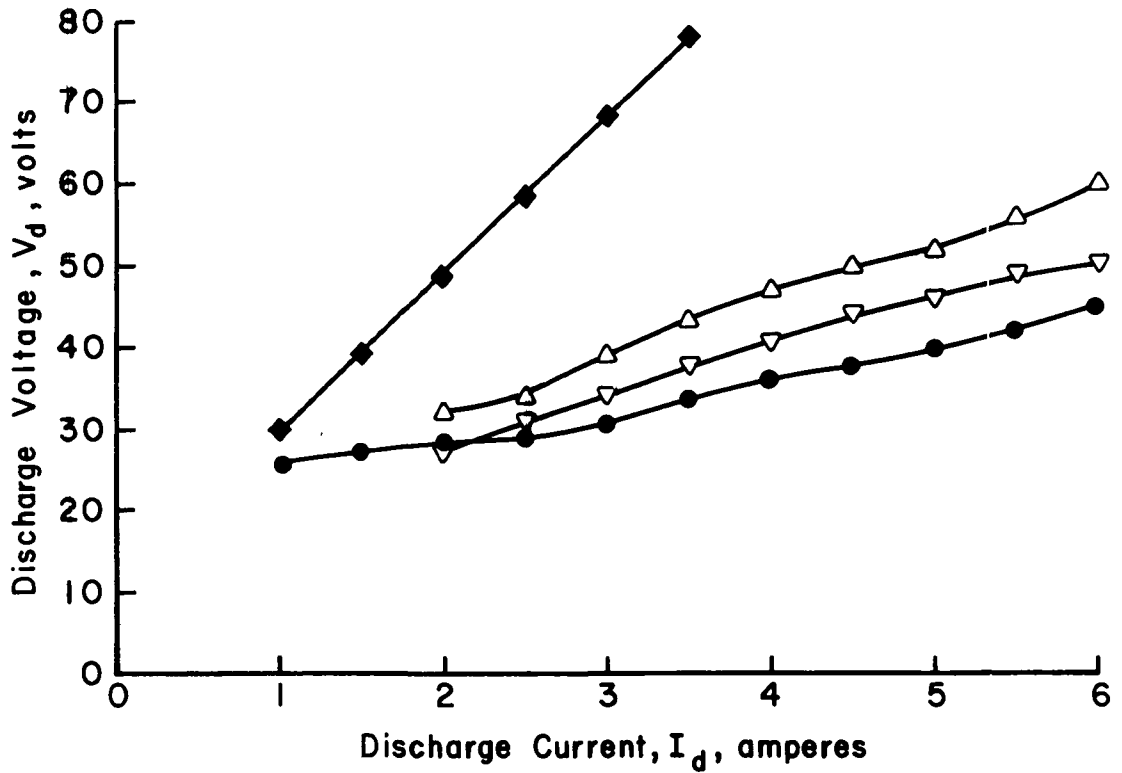


Figure 4-11. Effect of orifice size changes at high bell jar (background) pressure. Without screen anode.

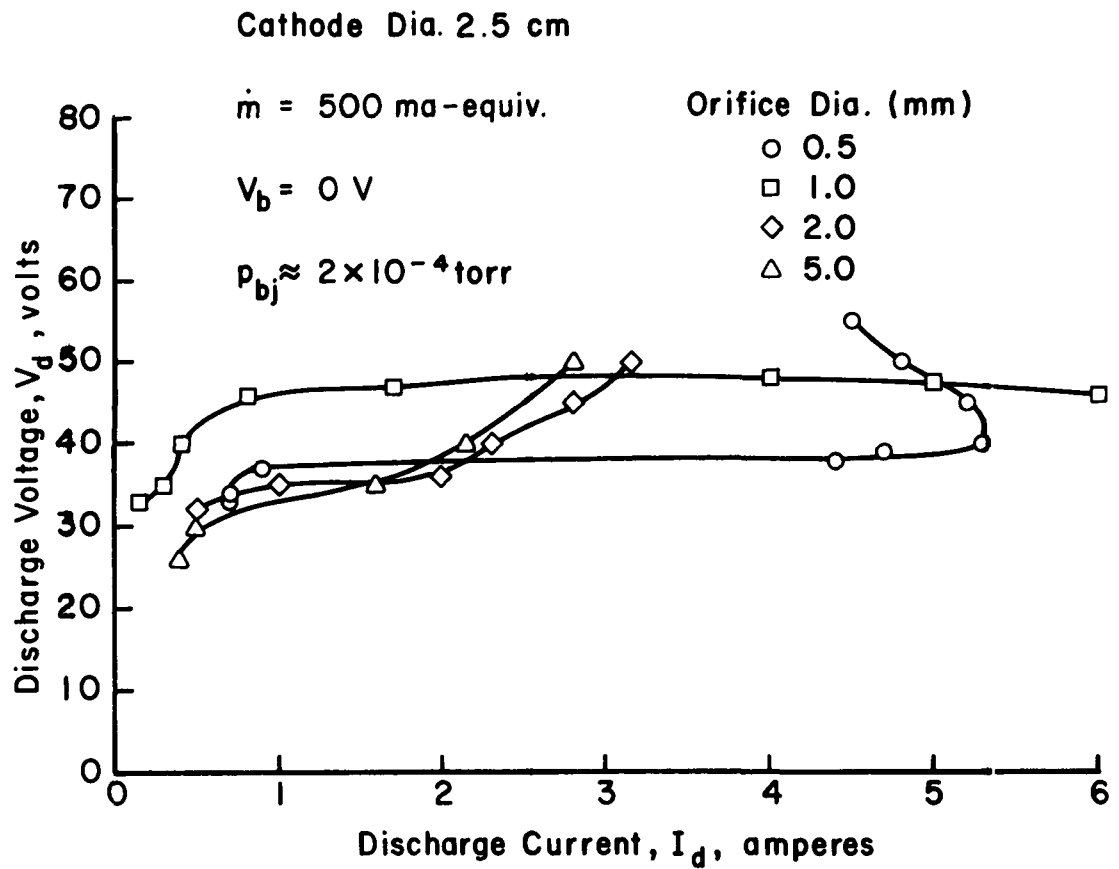


Figure 4-12. Effect of orifice size changes at low bell jar (background) pressure. With screen anode.

All the orifice plates were 1 mm thick. This thickness was found to be an approximate minimum value for both conducting away heat and withstanding erosion in mercury hollow cathodes. (A larger thickness than the minimum value is not desirable because of increased ion recombination within the orifice.) If similar voltages were obtained with argon, the heat losses and erosion rates would be roughly the same as mercury, hence require about the same minimum thickness. Because similar voltages for argon and mercury are implied in the long-life objectives of this study, initial investigations were limited to this 1 mm thickness.

It is interesting that fairly long life could be obtained for a cathode in the 1 to 2 ampere range despite the high voltage. As shown in Fig. 4-12, an orifice could start at 2 mm and wear to 5 mm without significant change in operating characteristics. There would be a large amount of sputtered material using such a design, but it could be used in any application that would permit this amount of sputtering.

Another survey of orifice diameters, in which a nonzero emitter bias was maintained, is shown in Fig. 4-13. Only the trends due to orifice size changes will be discussed here. The other effects of emitter bias will be discussed in the following section. The 2 and 5 mm orifices are better at low discharge currents, similar to the trends in Fig. 4-12. At higher currents, though, the 1 mm orifice is best. The 0.5 mm orifice operated over a restricted range that appears to correspond to only a part of the 0.5 mm curve in Fig. 4-12. Both voltage and current limited modes were used to obtain discharge curves. It therefore seems unlikely that a power supply interaction would prevent the 0.5 mm orifice from operating over a wider range. But until more is known about the operation of the 0.5 mm orifice with a bias, the possibility of a power supply interaction cannot be ruled out.

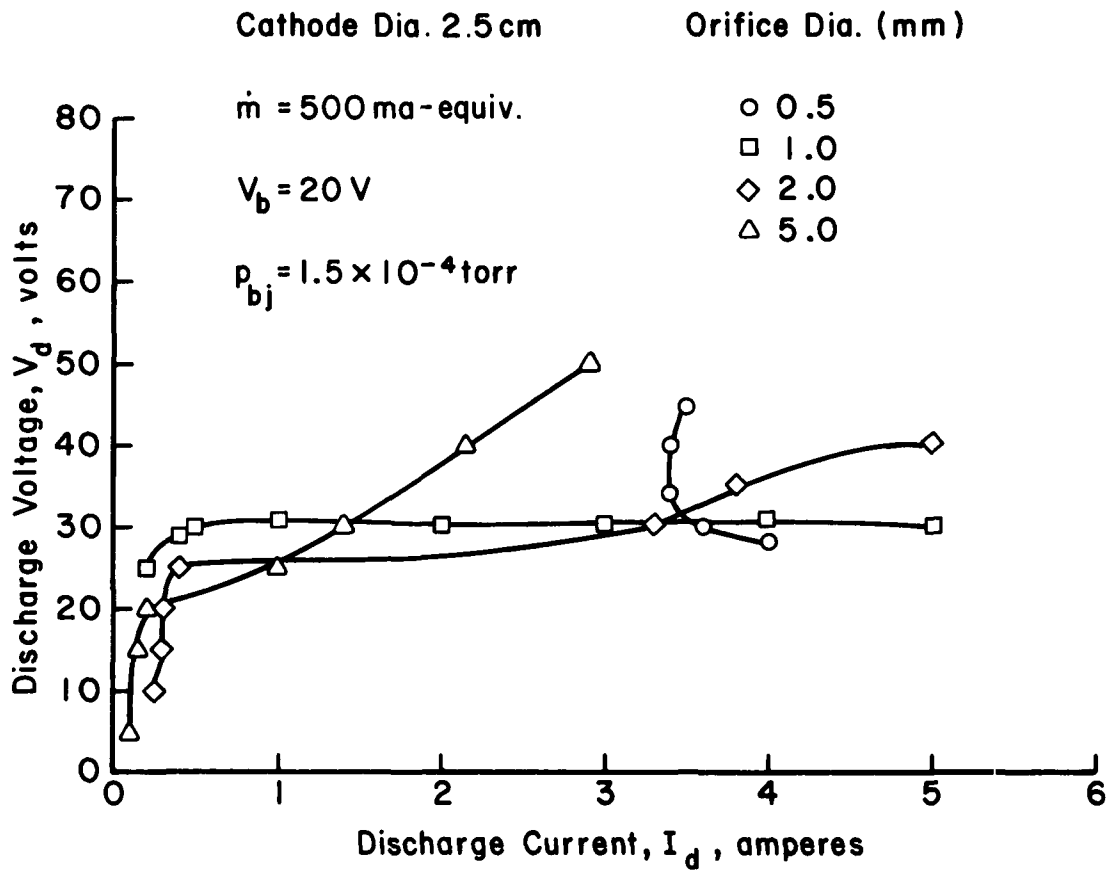


Figure 4-13. Effect of orifice size changes at a non-zero bias voltage. With screen anode.

### Emitter Bias Effect

With the exception of Fig. 4-13, all preceding data were obtained with the emitter at cathode chamber potential. (Nonzero biases were used only to initiate a discharge for these previous tests.) The effect of bias on steady state operation was investigated as a possible means of reducing discharge voltage, and hence erosion damage. Data from this portion of the investigation are shown in Fig. 4-14.

The effect of emitter bias voltage was substantial. Operation at discharge currents below 0.5 amperes was possible only with a bias voltage for the conditions shown. Above 0.5 amperes the use of a bias voltage permitted a substantial decrease in discharge voltage. The decrease in discharge voltage is clearly a step in the direction of decreased orifice sputtering. The effect on the emitter is less clear.

The discharge voltage is measured between the cathode chamber and the anode, while the emitter bias is between the emitter and the cathode chamber. The total emitter-anode voltage is therefore the sum of discharge voltage and emitter bias. The emitter lifetime will actually depend on the plasma environment in the cathode chamber, but this total voltage defines the approximate upper limit for energy of ions that bombard the emitter.

The emitter-anode voltage can be increased or decreased by the use of a bias voltage, depending on the specific operating conditions. With a 10 V bias, for example, the emitter-anode voltage can be as low as 20 V (compared to a minimum of 32 V with no bias). On the other hand, the use of a 20 V bias at a 1 ampere discharge current gives an emitter-anode voltage of 47 V (compared with 35 V at the same discharge current and no bias).

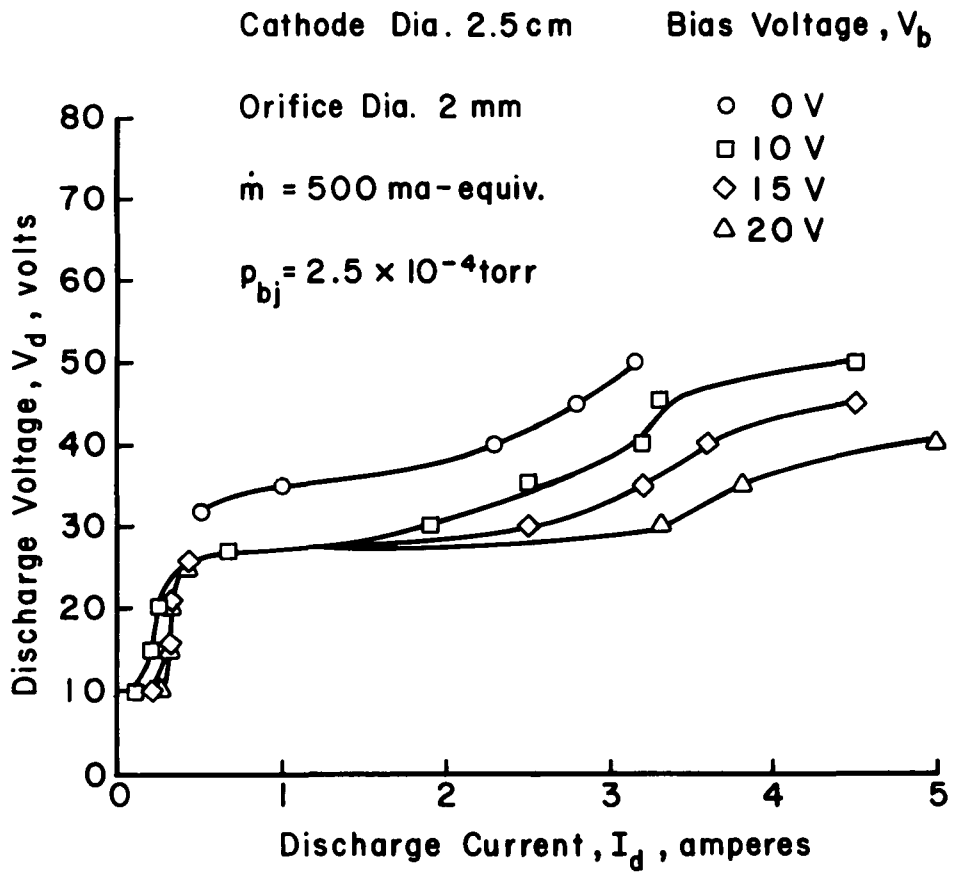


Figure 4-14. Effect of changes in emitter bias voltage. With screen anode.

From the emitter-anode voltage, then, the use of a bias voltage should lead to increased emitter lifetimes for some operating conditions. Plasma probe data and, ultimately, life tests will be required to determine the effect of emitter bias on emitter lifetime at other operating conditions.

Some other advantages of using a bias voltage are not shown in Fig. 4-14. While the minimum discharge voltage is 10 V in Fig. 4-14, bias data at other conditions showed minimum discharge voltages close to zero. Also, the minimum flow could be reduced from 500 ma-equivalent (no bias) to 200 ma-equivalent (with bias). With no coupling through the orifice, the internal bias discharge could be maintained at flows as low as 50 ma-equivalent.

A substantial electron current from the emitter to the cathode chamber wall was always observed during operation, even at zero bias voltage. The center tap of the emitter heating transformer winding was connected to the negative side of the bias supply. At zero bias, then, one side or the other of the emitter is negative relative to the surrounding chamber. With a conducting plasma present, an electron current will flow from the negative side of the emitter to the cathode chamber wall. The power supply requirements of the bias supply are indicated by data in Fig. 4-15, where both the internal bias discharge and external discharge characteristics are shown for a range of operating conditions.

#### Magnetic Orifice Cathode

The use of a magnetic field at the cathode orifice was included among the approaches investigated. A sketch of the configuration used is shown in Fig. 4-16. The cathode chamber consisted of a nonmagnetic stainless steel tube that was 2.5 cm in diameter. The magnetic field

Cathode Dia. 2.5 cm

Orifice Dia. 2 mm

$\dot{m} = 500 \text{ ma -equiv.}$

$V_b = 10V$

$p_{bj} = 2.5 \times 10^{-4} \text{ torr}$

○ Discharge Current,  $I_d$

□ Bias Current,  $I_b$

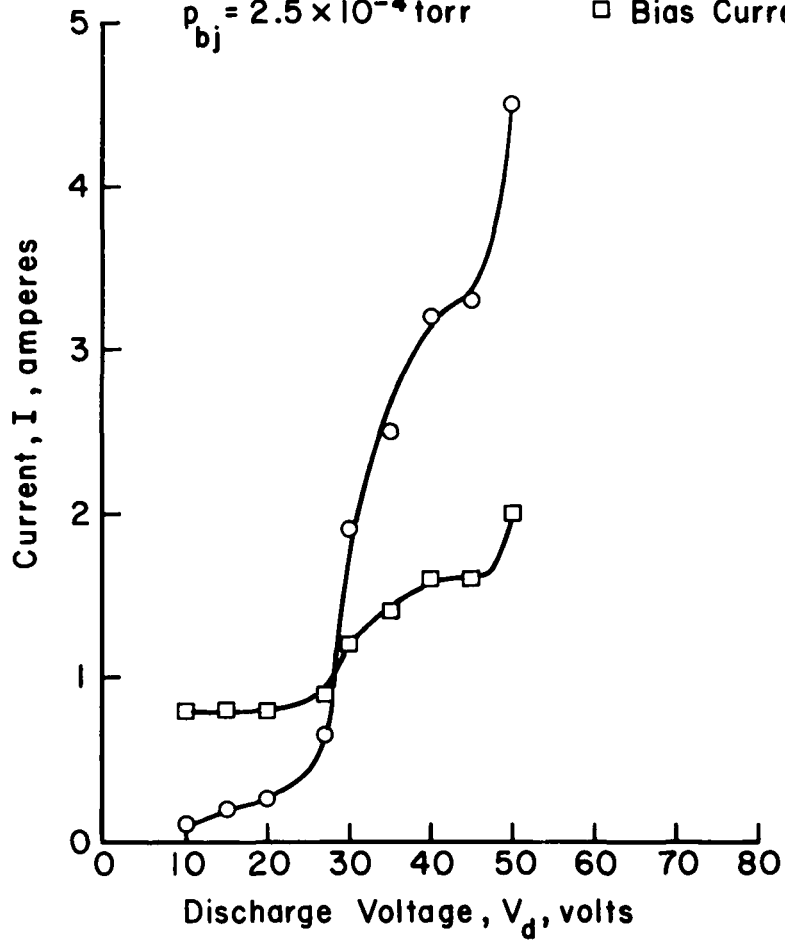


Figure 4-15. Comparison of discharge and bias current for the same operating condition. With screen anode.

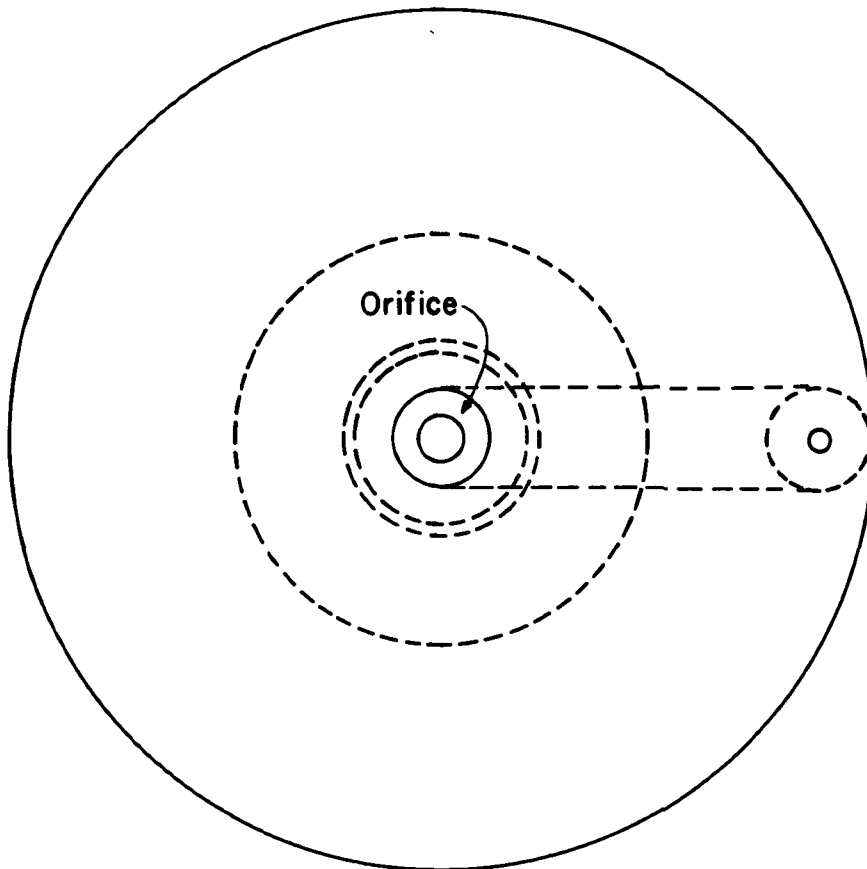
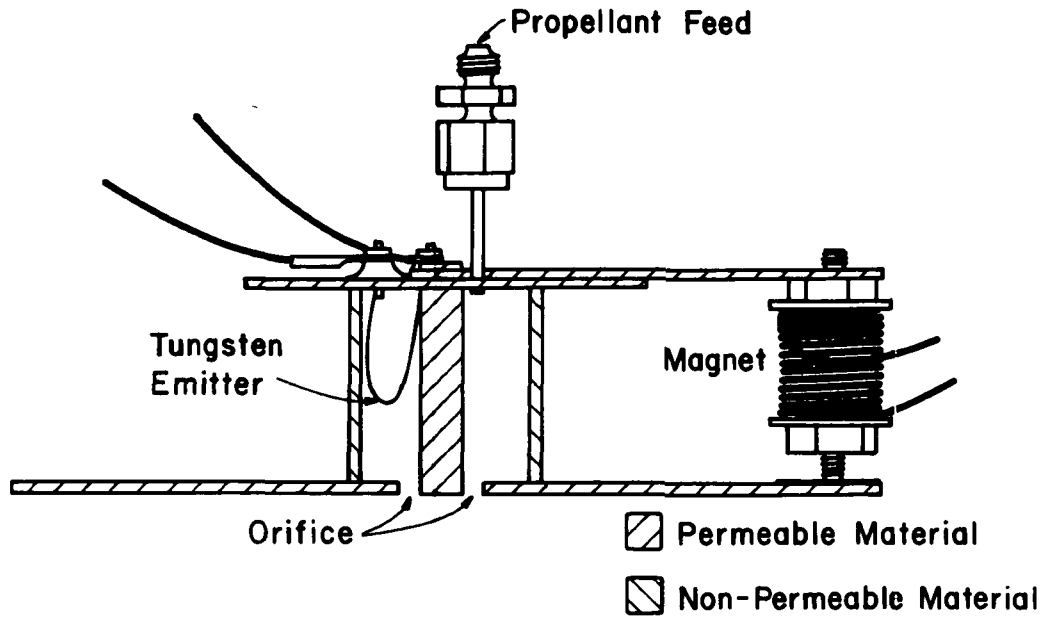


Figure 4-16. Magnetic orifice cathode.

at the orifice passed between a 6.4 mm diameter soft iron rod and a 1.6 mm thick orifice plate.

Data obtained with the magnetic orifice cathode are shown in Fig. 4-17. The data with an annular orifice area of  $0.95 \text{ cm}^2$  were obtained first. The performance was so poor that another orifice area ( $0.40 \text{ cm}^2$ ) was tried. The performance with the reduced area was substantially improved, but showed little advantage over the simple biased cathode of Fig. 4-14.

The field strength in the center of the orifice gap ( $0.40 \text{ cm}^2$  area) was about 150 Gauss at 3 amperes and something less than 50 Gauss at 0 amperes. Calculations indicated that  $\leq 50 \text{ eV}$  electrons should be contained at a maximum field strength of about 120 Gauss, so that the maximum experimental value of 150 Gauss should have been sufficient as the upper end of the range covered.

A magnetic field would be expected to reduce electron mobility through the orifice and increase ion production in that region. From the data of Fig. 4-17, though, the added ionization within the orifice due to a magnetic field has little effect on cathode performance. This conclusion is supported by the small difference between data obtained at 0 and 3 amperes. The big difference in data for the two orifice areas is probably due to pressure effects within the cathode chamber. Note that the  $0.95 \text{ cm}^2$  annular orifice is equal in area to that of an 11 mm circular orifice.

#### Discharge Chamber Cathode

The construction of this cathode concept is indicated in Fig. 4-18. The magnetic field is provided by four 6.4 mm diameter permanent magnets between two permeable pole pieces. The strength of the magnetic field was sufficient to prevent 50 eV electrons from going directly to the

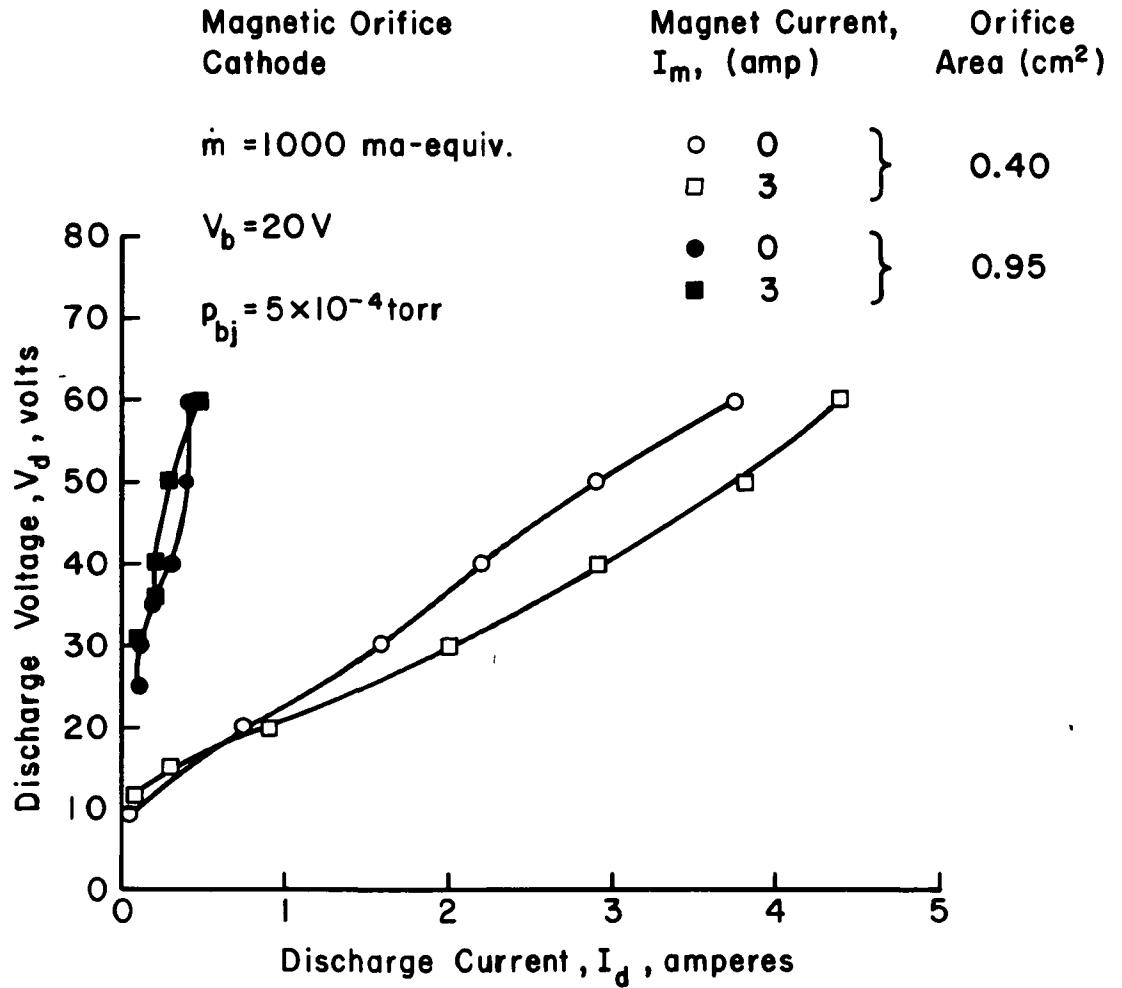


Figure 4-17. Effect on the performance of the magnetic orifice cathode due to changes in magnet current and orifice area. With screen anode.

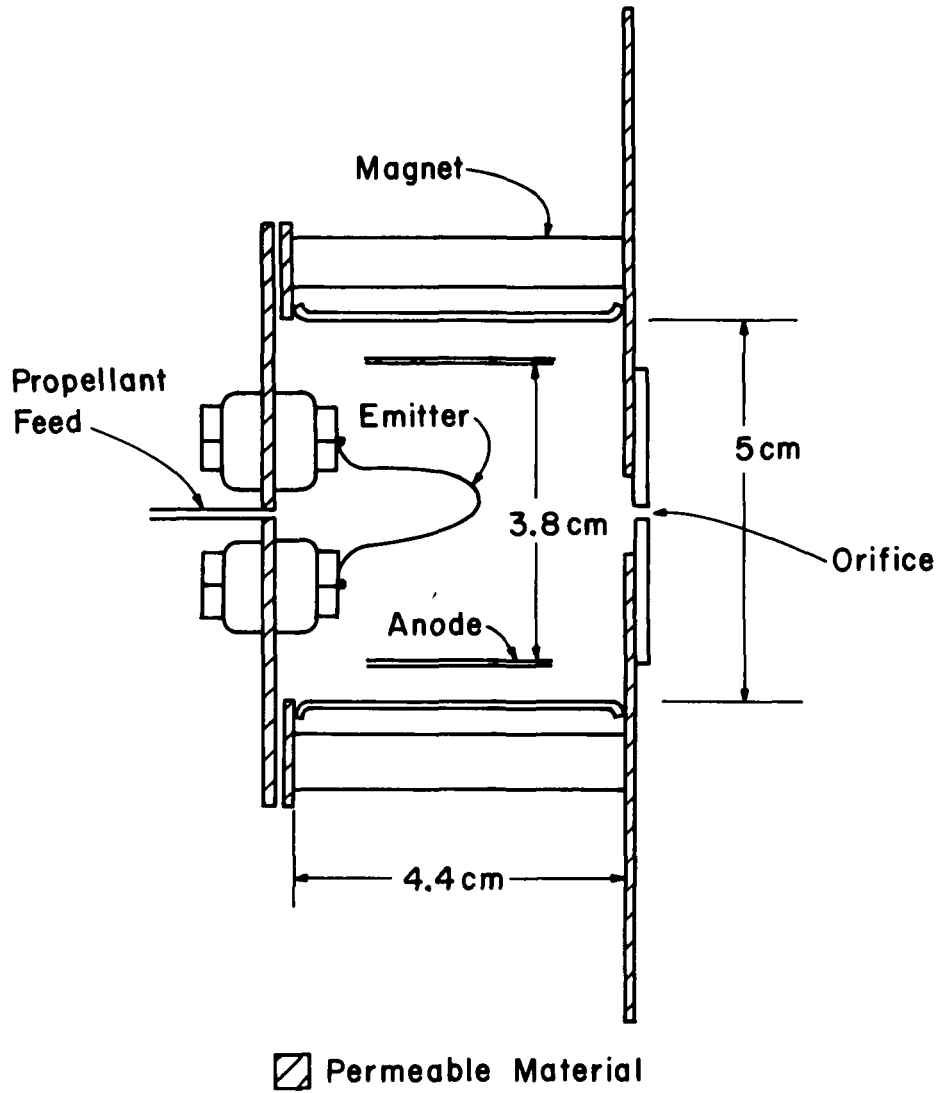


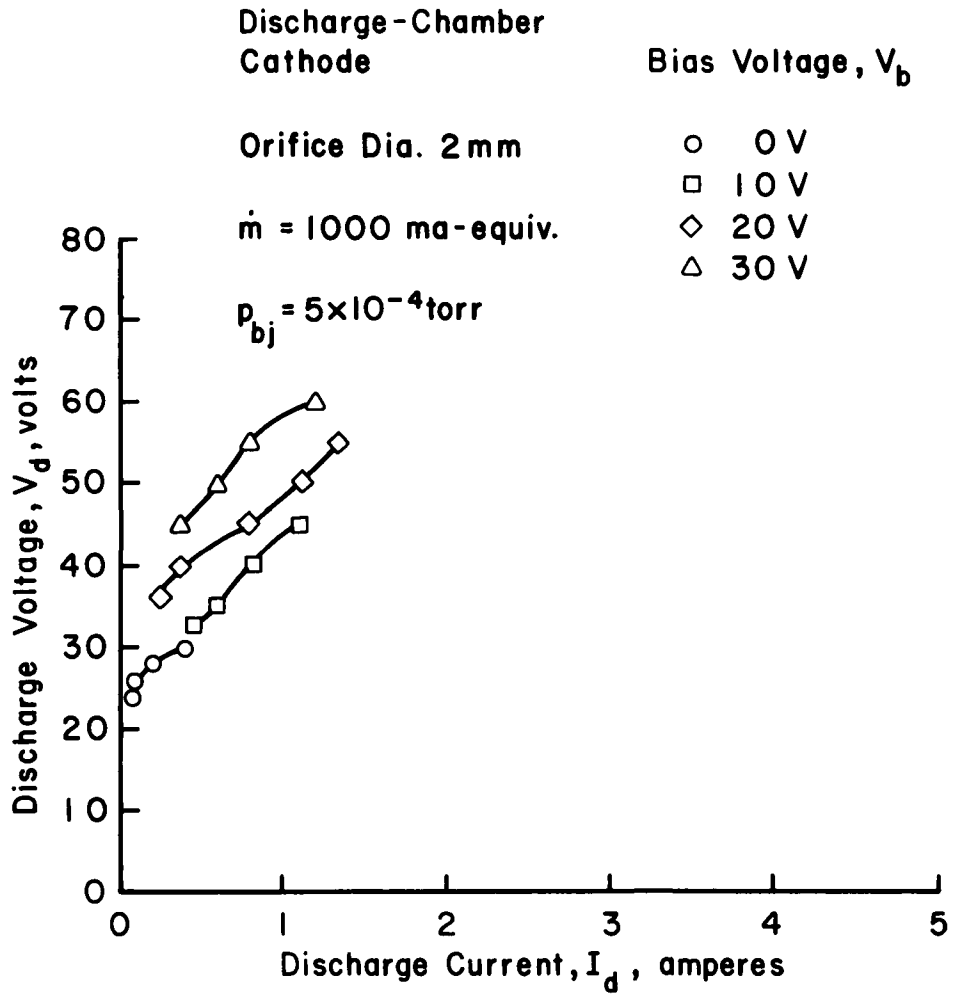
Figure 4-18. Discharge-chamber cathode.

internal anode after emission. The magnetic field is slightly divergent due to the downstream pole piece being larger than the upstream one. This cathode is used in the electrical system indicated in Fig. 4-1(b). Note that the internal anode is biased relative to both the emitter and the cathode chamber. This means that the discharge voltage equals the emitter-anode potential difference, regardless of internal bias.

The performance of the discharge chamber cathode is shown in Fig. 4-19 for both 2 and 5 mm orifice diameters. (Operation was attempted with a 0.5 mm orifice, but the internal discharge could not be coupled to the external anode.) The discharge voltage generally increases with bias voltage for both orifice diameters. The difference is small, though from 0 to a 10 V bias. The advantage of a bias voltage for a simple cathode chamber (shown in Fig. 4-14) is therefore missing for the discharge chamber cathode. That is, the use of a bias voltage will not result in reduced orifice sputtering for a discharge chamber cathode.

The variation of emitter-cathode potential difference is a different story. In Fig. 4-14, for discharge currents that were common to both bias voltages, going from 0 to 10 volts bias resulted in 0 to 4 volts increase in emitter-anode voltage. For the discharge chamber cathode, keeping in mind the discharge voltage equals the emitter-anode voltage, the increase of the latter is 1 to 5 volts.

It appears that the use of a bias voltage can substantially change operating limits. But, within these operating limits, a bias of 10 V has little effect on emitter-anode potential difference. Also, for a bias voltage to reduce orifice sputtering, the emitter should be biased negative relative to the orifice. This means that a more promising configuration of the discharge chamber cathode would have the orifice in the anode.



(a) 2 mm orifice

Figure 4-19. Effect of varying the emitter bias voltage on cathode performance. With screen anode.

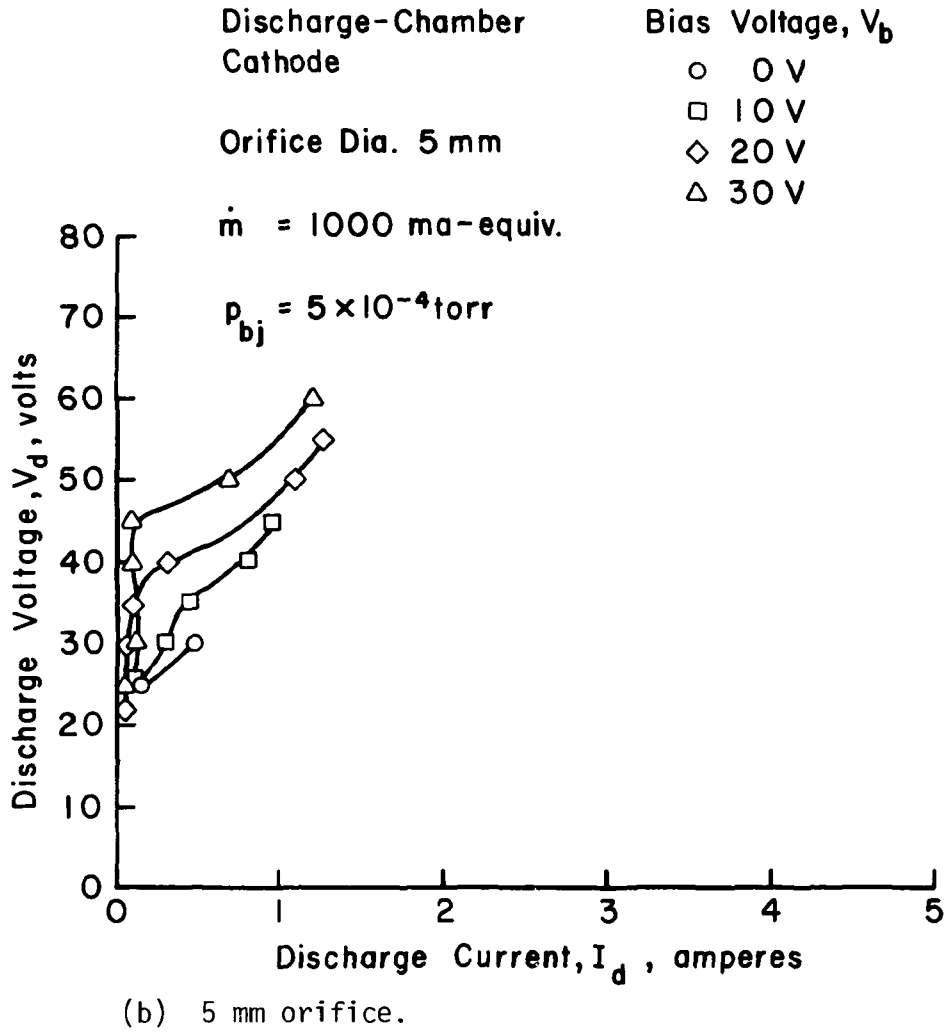


Fig. 4-19- Concluded.

The effect of propellant flow rate on performance of the discharge chamber cathode is shown in Fig. 4-20, and is similar to that shown for other cathode types. The higher flow results in higher pressures and higher probabilities of electron collisions with atoms. The higher collision probability leads to lower discharge voltages.

#### Cathode Chamber Plasma Properties

Plasma properties within the cathode chamber were obtained using Langmuir probes. The probe was an 0.07 mm diameter tungsten wire with an exposed area of about  $1.3 \times 10^{-2} \text{ mm}^2$ . This probe was located 1 cm from the upstream plate of the 2.5 cm cathode chamber. The cathode performance data for the configuration used are shown in Fig. 4-21.

Plasma potential, electron temperature, electron density, and emitter bias current are shown as functions of discharge voltage in Fig. 4-22. At zero discharge voltage, the discharge current was also zero. The plasma properties at this condition were therefore the result only of the bias discharge. All the plasma properties change slowly with discharge voltage up to the 35 to 45 V range. Below this range, the plasma properties appear to be determined mostly by the internal discharge, and the plasma potential (relative to ground) is 5 V, or less. This means that ions from the internal plasma should strike the emitter at an energy corresponding to bias voltage plus 5 V, or 25 eV. The electron density is  $\sim 10^{12}/\text{cm}^3$  (below a 35 V discharge), which is  $\sim 10$  times more dense than a typical ion thruster discharge chamber. But the ion energy of 25 eV is approaching the sputtering threshold, where indefinite lifetime can be expected in the absence of contaminants.

The plasma properties are also shown in Figs. 4-23 and 4-24 as functions of propellant flow rate and emitter heater current. The effects

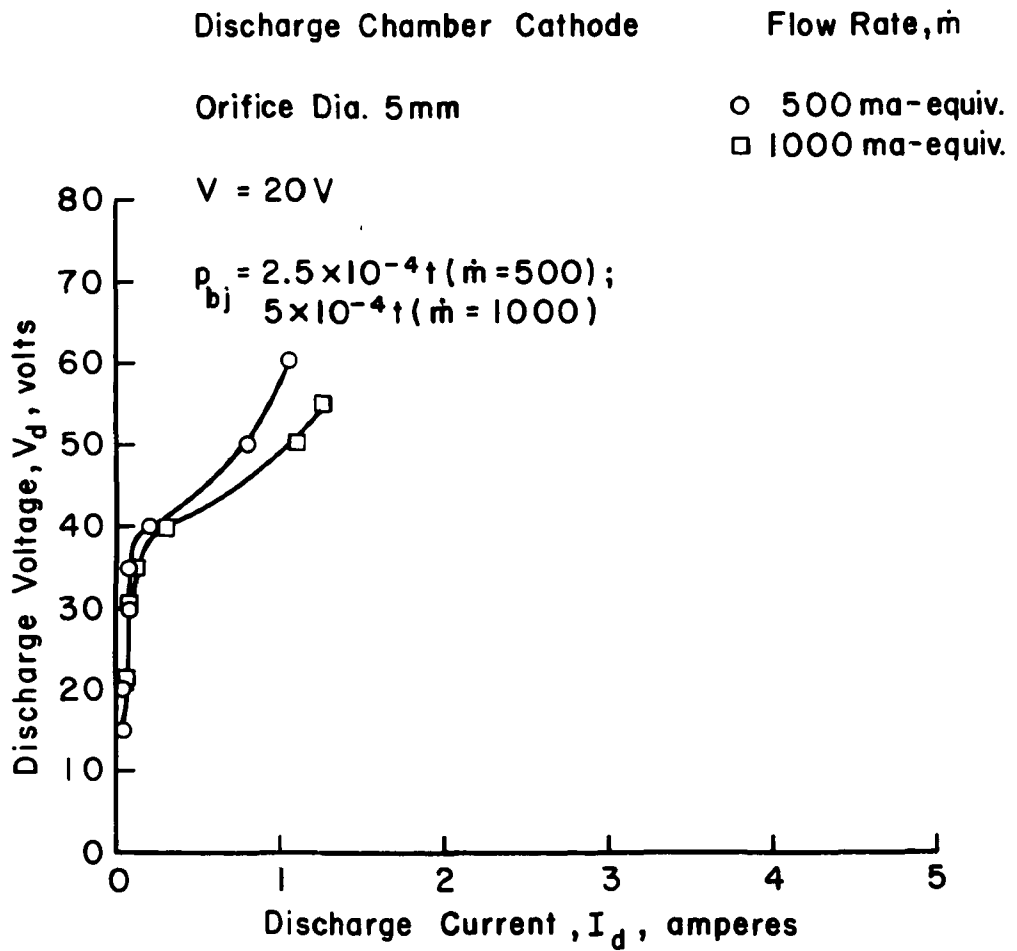


Figure 4-20. Effect of changing the propellant flow rate on cathode performance. With screen anode.

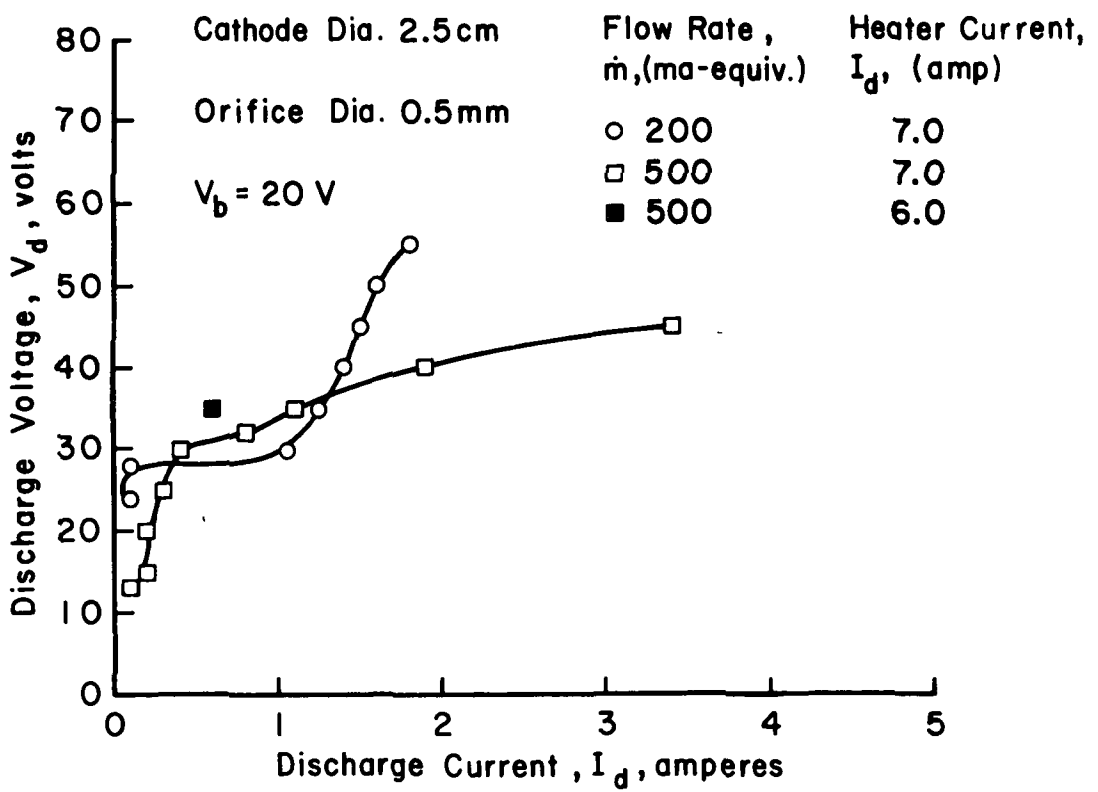


Figure 4-21. Cathode operating conditions corresponding to plasma properties illustrated in Figures 24-26. With screen anode. (Plasma properties not obtained at all data points.)

Cathode Dia 2.5cm  
Orifice Dia. 2mm  
 $\dot{m} = 500$  ma-equiv.  
 $V_b = 20V$   
 $p_{bj} = 2.5 \times 10^{-4}$  torr

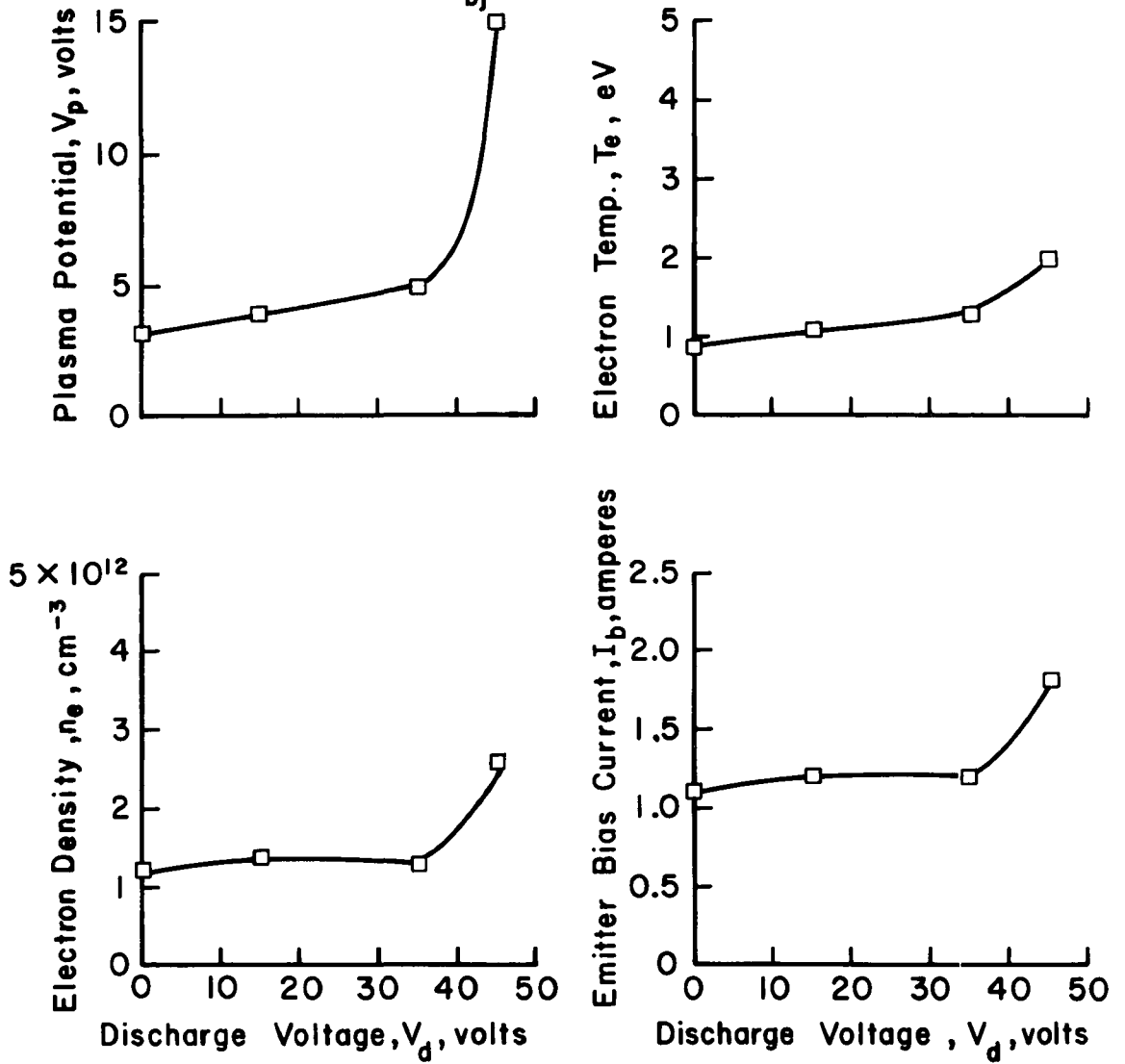


Figure 4-22. Plasma properties as a function of discharge voltage.

Cathode Dia. 2.5 cm

Orifice Dia. 2 mm

$V_b = 20$  V

$V_d = 30$  V ( $\dot{m}=200$ );  $35$  V ( $\dot{m}=500$ )

$p_{bj} = 2.5 \times 10^{-4}$  torr ( $\dot{m}=500$ );  $1 \times 10^{-4}$  torr ( $\dot{m}=200$ )

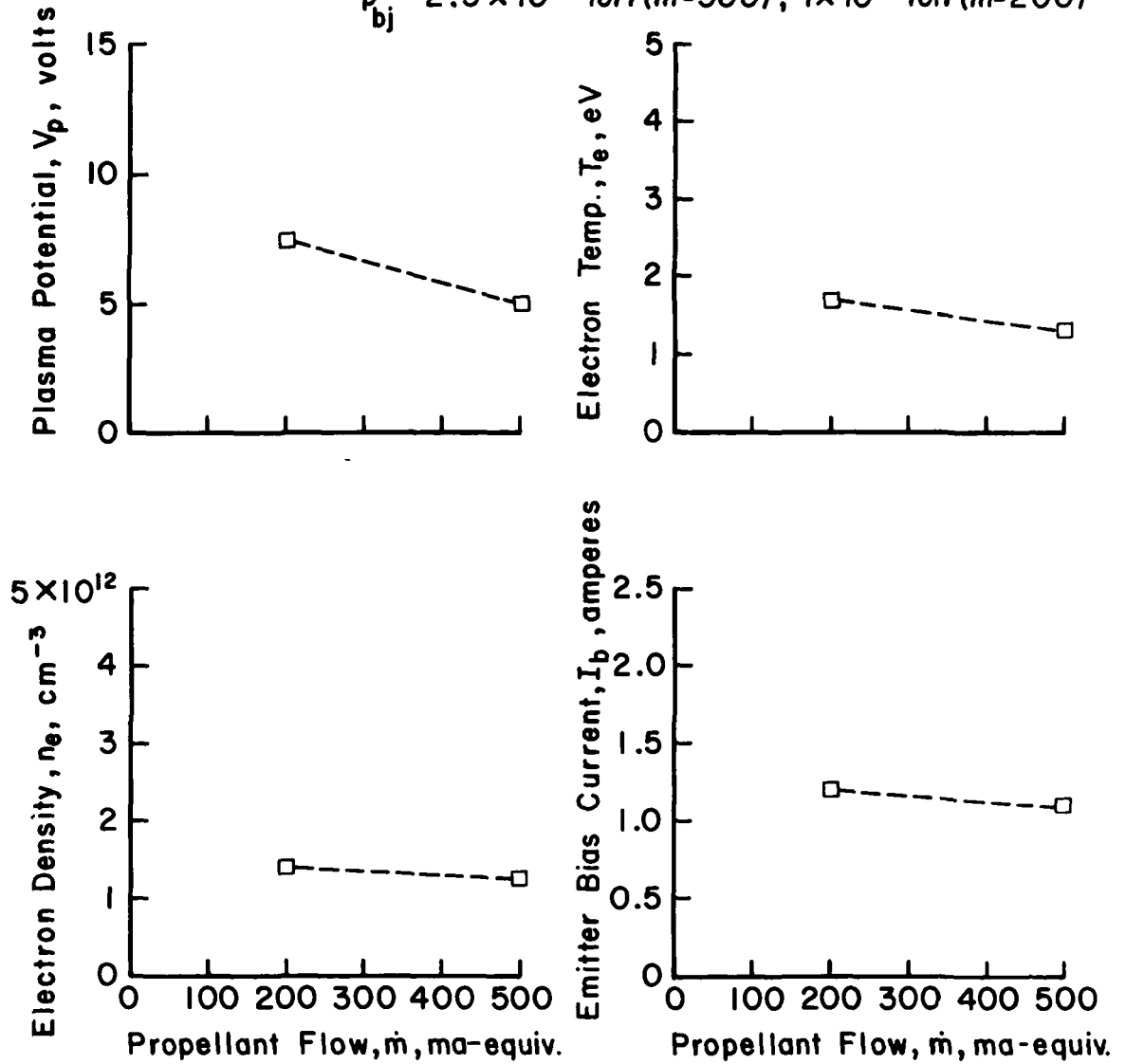


Figure 4-23. Plasma properties as a function of flow rate.

Cathode Dia. 2.5 cm  
Orifice Dia. 2 mm  
 $V_b = 20V$   
 $V_d = 35V$   
 $p_{bj} = 2.5 \times 10^{-4}$  torr

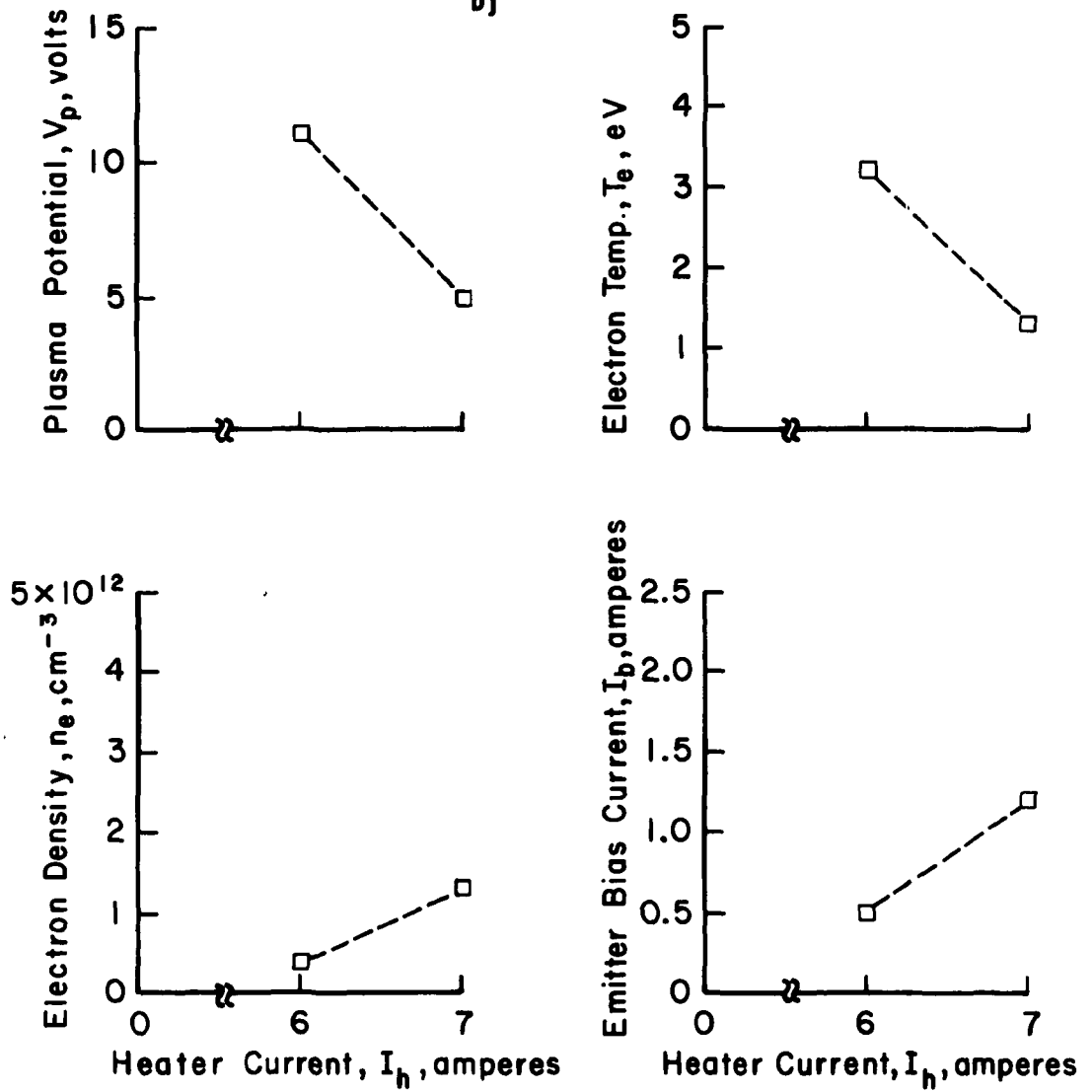


Figure 4-24. Plasma properties as a function of heater current.

of flow rate are minor, except for a small rise in plasma potential at the lower flow rate. The effects of decreasing the emitter heater current by one ampere is more significant. This decrease leads to a substantial reduction in emission, as indicated by the drop in bias current. This, in turn, results in a substantial drop in electron density. To offset the decrease in electron emission, the plasma potential increases. This increases ionization by increasing both the emitted electron energy and the background electron temperature. It is clear that an excess of electrons from the emitter is preferable to a shortage. A shortage will lead to higher energies for bombarding ions and therefore a more rapid failure of the emitter.

The effect of changing bias voltage was found to be more complex. Above 10 V, bias voltage changes resulted in little change of plasma potential or electron density. The electron temperature, surprisingly, decreased slightly with an increase in bias voltage. Below 10 V, probe traces became increasingly difficult to analyze. The effect of bias voltage on the probe trace is indicated in Fig. 4-25. These traces were obtained in a 2.5 cm cathode chamber with a 5 mm orifice.

Assuming a Maxwellian electron distribution, the probe current becomes nearly constant or increases slowly as the probe potential is increased above the plasma potential. Fig. 4-25(c), at 20 V bias, shows the curve shape normally expected, with a well defined inflection point at plasma potential (at ~ 30 V probe potential). At a 10 V bias, Fig. 4-25(b), the plasma potential can still be determined, but with less certainty. When the bias voltage is reduced to zero, the plasma potential is no longer evident -- Fig. 4-25(a). Most probe traces at zero bias were further from the ideal than the one shown in Fig. 4-25(a), with current

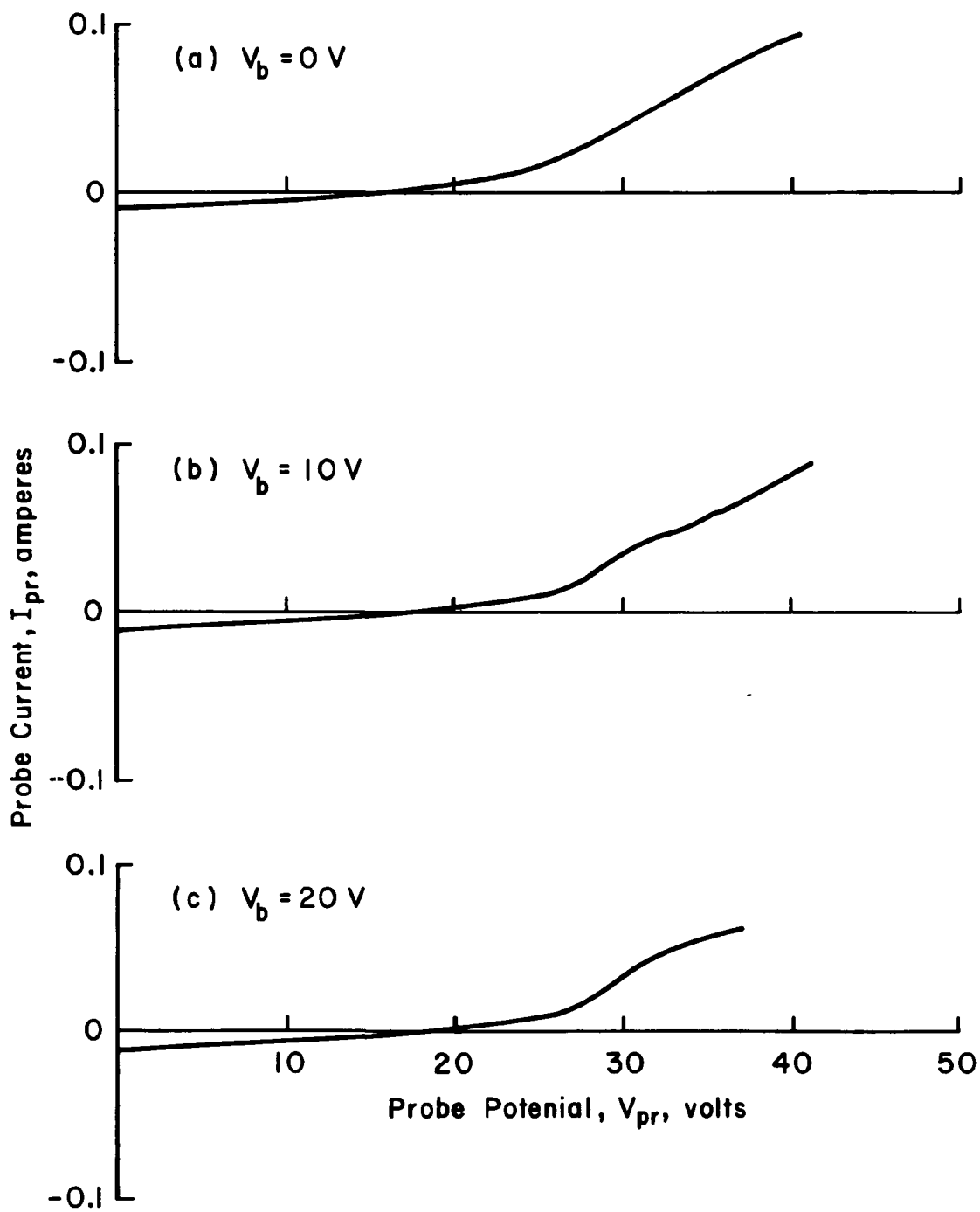


Figure 4-25. Langmuir probe traces at several different bias voltages.

continuing to increase at an increasing rate as probe potential is raised, until a damaging arc is established.

A possible explanation for the degradation of probe traces at low bias voltage is the presence of high frequency plasma fluctuations. The recording equipment used would average the potential and density fluctuations in the plasma, so that the trace obtained would be a composite of a wide range of instantaneous traces.

The plasma probe was connected to an oscilloscope to look for plasma fluctuations. For the zero bias case of Fig. 4-25(a), a 0.1 V peak-to-peak signal was found at about  $4 \times 10^5$  Hz. At a 10 V bias this signal still appeared to be present, but much weaker. At a 20 V bias, no rapid fluctuation was evident. Other tests at zero bias showed signal amplitudes up to 7 volts, so the low magnitude found with the trace of Fig. 4-25(a) may be associated with the more conventional shape of that probe trace.

Population-potential oscillations are often found in plasmas. The attrition of electrons and ions, with electrons leaving faster because of their low mass, results in the increase in plasma potential. At some value of plasma potential there is a sudden influx of electrons, which produce a new generation of ions due to collisions with background neutrals. Some oscillation of this type appears possible at low bias voltages. The loss of ions would be expected to be related to ion transit time (ion acoustic wave velocity), which is in approximate agreement with the observed frequency. Similar oscillations in discharge current were observed by Byers in Mercury hollow cathode tests.<sup>1</sup> Byers found that changes in keeper supply impedance affected both the oscillations and the cathode performance. No changes in power supply impedance were made for the tests reported herein.

### Cathode Starting

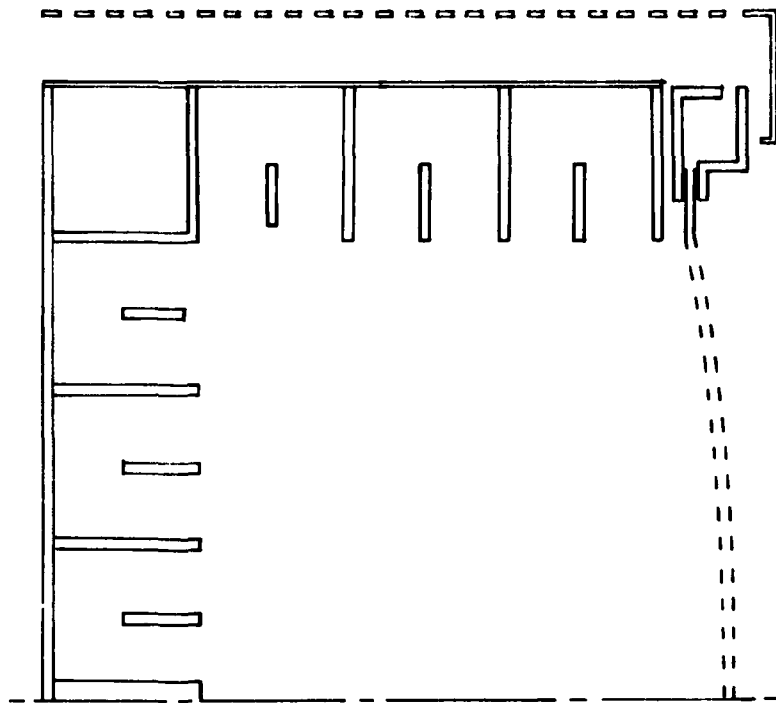
Ease and reliability of starting were also of interest in this investigation. Normal startup procedure was to obtain an internal cathode chamber discharge by biasing the emitter at -30 V relative to the chamber wall - or internal anode in the case of the discharge chamber cathode. This internal discharge always started if the emitter heater was used (at 6 to 7 amperes) to preheat the cathode chamber for 5 to 10 minutes. Omission of this preheat step sometimes led to erratic startups. The bias current at 30 V was typically 1 to 2 amperes for a heater current of ~7 amperes. At this point, initiation of a discharge to the main anode could usually be accomplished by applying normal voltage to the main anode. For low propellant flow rates and/or small orifice diameters (less than 1 mm), a high voltage tickler (about 17 kV maximum) was required to initiate the main discharge. Restarts were easier than the initial startup after pumpdown, probably because contaminants were removed by normal operation.

In summary, the use of an internal emitter and a preheat phase gave 100 percent starting reliability for the internal discharge. Initiation of the discharge to the main anode was more dependent on propellant flow rate and orifice diameter, with increases in both parameters favoring startup of the main discharge.

## V - FLIGHT-TYPE THRUSTERS

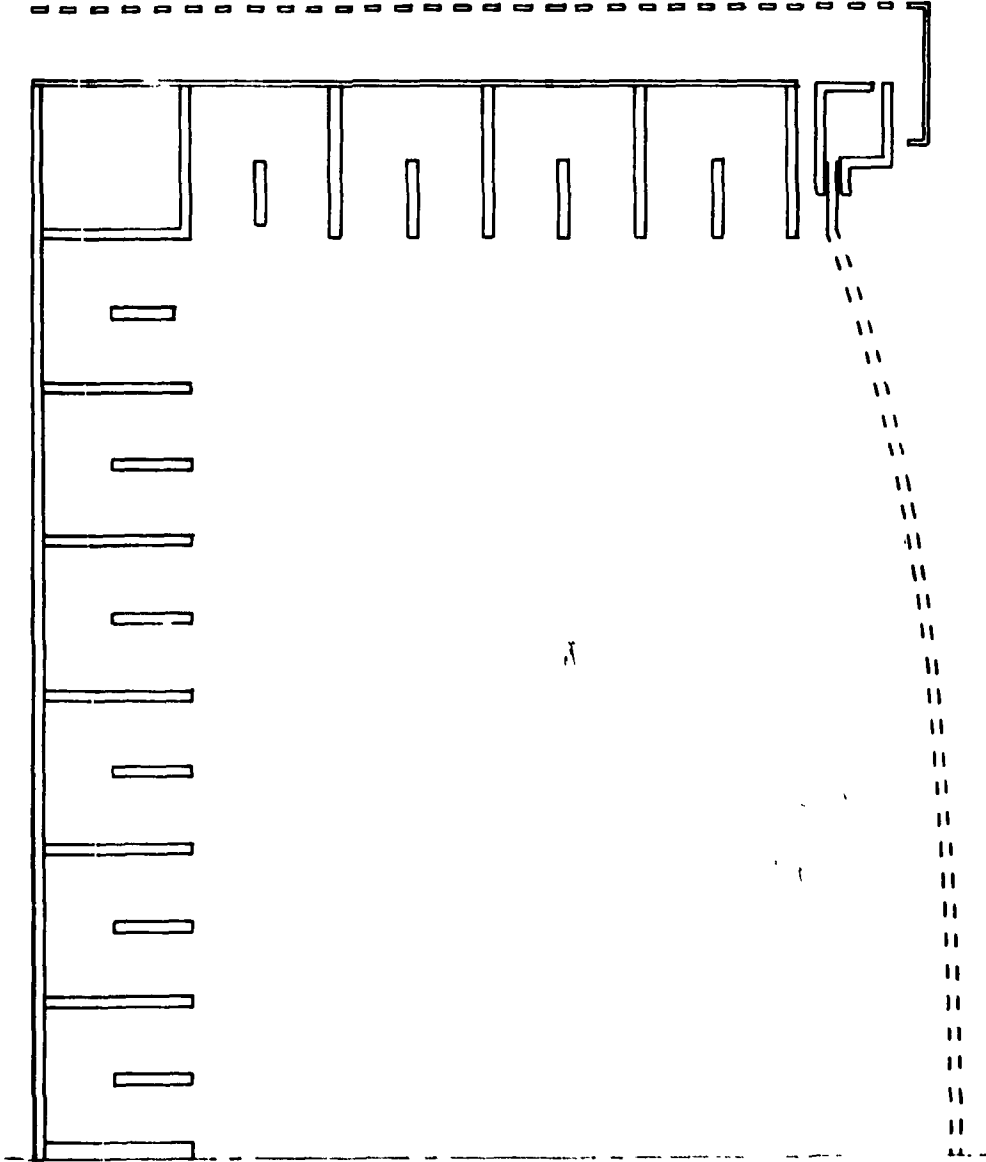
The multipole gas thruster is sufficiently developed for a first approximation of flight-type design and mass. Two thruster sizes were considered, 15 cm and 30 cm. The design approach for both of these sizes was similar, as shown in Fig. 5-1. The cylindrical outer shell is a stress carrying member and is stiffened by the pole pieces. Hard point attachment can be obtained by integrating the two corner pole pieces and the back plate into a single rigid structure. The back plate is shown as a simple flat plate, but is thick enough that a stiffer structure can be designed for the same weight. Back plate, pole pieces, and anodes in the basic design of Fig. 5-1 are all 1.5 mm thick. The cylindrical outer shell and the ground screen (50 percent open) are both 0.75 mm thick. This last thickness is approximately the minimum to avoid excessive screw hole enlargement during frequent assembly and disassembly.

The basic design, as indicated in Fig. 5-1, used 2.5 cm wide pole pieces spaced 2.5 cm apart. This is approximately the pole-piece configuration tested in this grant. The distribution of mass in the basic design is indicated in the following table:



(a) 15 cm

Figure 5-1. Thruster conceptual designs.



(b) 30 cm

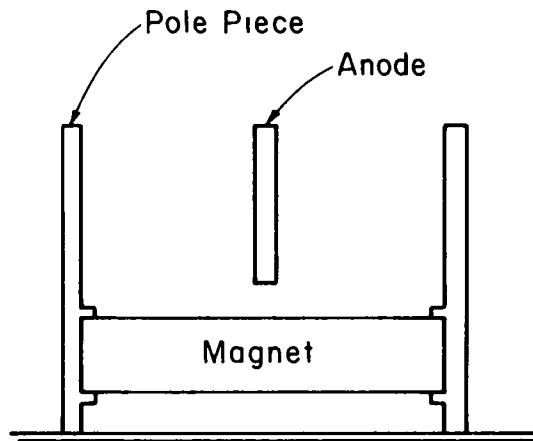
Figure 5-1. Concluded.

Table 5-1  
Distribution of Thruster Mass

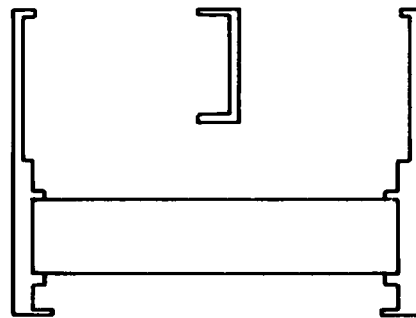
	15 cm	30 cm
Pole pieces	.29	.29
Anodes	.10	.12
Outer cylinder	.11	.09
Back plate	.11	.13
Permanent magnets	.15	.18
Grids	.06	.06
Grid supports	.10	.07
Ground screen	<u>.08</u>	<u>.06</u>
Total	1.00	1.00

The calculated masses of the thruster components shown add up to 2.8 kg for the 15 cm thruster and 7.2 kg for the 30 cm. There will be a large number of insulators and fasteners that are not included. For these insulators and fasteners, together with main and neutralizer cathodes, an additional 50 percent mass is estimated. This gives a total of 4.2 and 10.8 kg for the basic 15 and 30 cm thrusters.

The total masses for the basic thrusters are large due to the numerous anodes and pole pieces. Together, these components add to about 40 percent of the total for both thruster sizes. Substantial mass reductions can be obtained by contouring these components. Contouring (see Fig. 5-2(b)) would reduce weight by using stiffer cross sections with less mass as well as varying pole-piece thickness to match the magnetic flux density. Contouring anodes and pole pieces is estimated as capable



(a) Basic Design



(b) Contoured Design

Figure 5-2. Pole-piece and anode cross sections.

of reducing these component masses by half. The total thruster masses using this approach are estimated at 3.4 and 8.6 kg for the 15 and 30 cm thrusters.

Further mass reductions should be possible using lighter materials. The mass estimates given above all assume stainless steel in all parts except pole pieces. Substitution of titanium for stainless steel, for example, should permit further reductions, although no calculations were made for such an option.

## VI - GAS THRUSTER PROPULSION SYSTEM

A preliminary system analysis was made to determine major component needs for argon and xenon space propulsion applications. Major components making up the gas feed system are discussed in detail. General component status and potential experiments are examined. A summary list of recommended follow-on activities is included.

Fig. 6-1 shows the gas feed system discussed herein. Components and activities involving these components are discussed in the order of propellant flow direction.

### Tankage

Owen gives an analytical comparison of noble gases, cesium, and mercury tankage which is adequate for this system analysis.<sup>1</sup> The minimum tankage-to-propellant ratios for argon, xenon, and mercury are 0.76, 0.12, and 0.16. The high tankage fraction for argon results from the storage in the gas phase. Xenon is stored near critical conditions (58 atm, 17°C) while mercury is, of course, stored as a liquid. Despite the substantially heavier tankage fraction for argon, the choice between argon and xenon as an alternative to mercury is not clear. This lack of clear choice is due to the much higher cost and poorer availability of xenon. As an example, a low tankage fraction is less important in auxiliary propulsion, so that argon could easily be a better choice for stationkeeping. As another example, extremely large systems could use cryogenic storage similar to that used for fuel cells in Apollo flights. Cryogenic storage should eliminate most, or all, of any tankage penalty associated with argon.

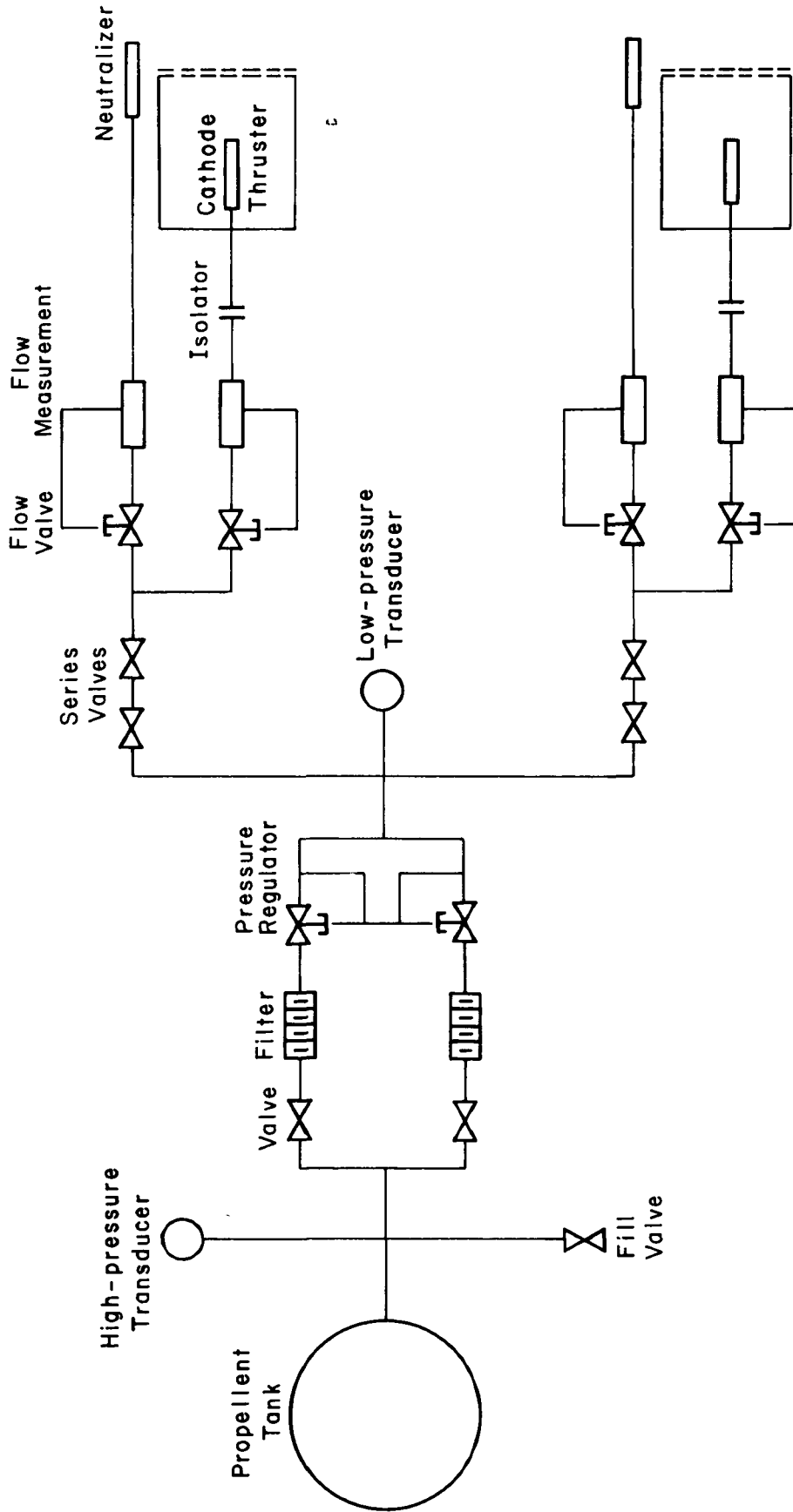


Figure 6-1. Gas feed system.

An extensive background of flight experience exists for long-life gas tankage and valving systems. The gas storage and control systems developed for the Pioneer, Mariner, and Viking programs should be surveyed for components that can be used in ion propulsion systems. Some of this space-flight background is covered in a book edited by Schurmeier.<sup>2</sup> One paper in that book, for example, describes a low leakage valve design that was successfully tested for 72,000 cycles.<sup>3</sup>

### Flow Metering and Control

A breadboard of a closed-loop control system would be valuable to provide proof of concept as well as to build up practical experience. Heated capillary flow measuring devices and piezoelectric flow control valves have both been used at Colorado State University. The flow measuring devices have included both commercial versions<sup>4</sup> and experimental versions designed by Dr. Wilbur. The piezoelectric valve is a commercial version<sup>5</sup> that is controlled directly by an applied voltage. With the crystal the only moving part, the response rate is extremely fast and the expected reliability very high. The only additional components required for a control system are some electronic logic elements. The output of the commercial flow measuring device is a low-level voltage signal. This signal can be compared to a reference signal, with the output used to control the 0-100 volt piezoelectric valve signal. Using only commercial components, a control breadboard can be constructed to test the full range of input/output choices. Of particular interest are cold starts with gas, which should be much faster than possible with a condensible propellant. Space qualified versions of the flow measuring device and piezoelectric

valve would eventually be required, but (time permitting) a breadboard test with commercial components should precede such development.

### Isolation

Electrical isolation between the tankage and thruster should be simplified with a gas propellant. A mercury isolator must operate above 125-150°C to avoid condensation and below about 300°C to avoid gradual failure of the insulator. With no condensation problem, a gas isolator should have a much wider temperature range, hence be much easier to thermally integrate into a thruster design. The recommended approach would be to test existing isolator concepts. The multiple screen approach of Hughes should be satisfactory, perhaps even with a reduced number of screens. The earlier Lewis concept of an aluminum-oxide coaxial labyrinth was found marginal with mercury and SERT II voltages, but should be satisfactory with inert gas at lower voltages.

### Cathodes

Different cathode approaches should be used for argon and xenon. Hollow cathodes operated for short times on xenon have performed in a manner similar to what has been observed with mercury. Because of this similarity and the known excellent performance with mercury, the hollow cathode appears to be the best approach with xenon. The major uncertainty is lifetime. A duration test of a hollow cathode with xenon should be conducted at conditions close to that used with mercury to permit a direct comparison.

Argon presents a different problem. Hollow cathodes have been operated on argon, but high voltages and/or high operating temperatures

have often resulted in rapid failures. It appears clear that long-life argon cathodes will require a different approach than that developed for mercury for at least some operating conditions. NASA Grant NSG-3011 currently includes the study of alternate long-life cathodes for argon.

#### Discharge Chamber Erosion

The erosion of discharge chamber components is related to cathode lifetime. The higher vapor pressure of gas propellants would be expected to increase the erosion of these components due to the absence of adsorbed protective layers that are found with mercury below about 300°C. Although this problem is not expected to be crucial, experimental evaluations should be conducted with argon and xenon, similar to those already conducted with mercury.

#### Starting and Control

Mirtich has demonstrated acceptable starting performance down to -100°C with a 30-cm mercury thruster.<sup>6</sup> Due to the limits imposed by condensation, full power was not developed for nearly an hour. With gas feed systems, the propellant boiling points are so low (-186°C for argon and -107°C for xenon) that similar cold starts should result in full power operation in several minutes. The thermal shock transients possible with gas propellants are therefore greater than those previously experienced with mercury. While no significant starting and control problems are anticipated with gas propellants, extension of existing thermal analyses and operational demonstrations are recommended.

#### Propulsion-System Characteristics

It is unlikely that the thruster efficiency of a thruster using

lighter atoms will ever exceed that of a similar thruster using heavier atoms. There is no data available at present that contradicts this trend. This simple general trend, however, is complicated by the near infinite number of hardware-mission combinations that can be used to support a variety of conclusions. For this reason, two classes of missions are recommended for study to characterize gas propellant systems.

The first mission class is composed of those missions that are under near-future consideration for mercury propellant. Care should be taken to assure that the modular design of specific hardware does not bias system performance toward either gas or mercury propellant. It is expected that such a comparison would show only small overall differences between xenon and mercury. The heavier tankage and the effect of much lighter atomic weight on thruster efficiency would be expected to show a substantial penalty for argon on the missions of this class.

The second mission class consists of those missions that are particularly suited to the use of a gas propellant. Near-earth missions would have an environmental advantage with gas propellant. While there is no known hazard of a properly conducted mercury propellant mission, past associations of hazards with mercury contamination will always tend to raise questions about mercury. The use of an inert gas propellant, on the other hand, would not tend to raise these questions. If a large number of near-earth missions were planned, the potential environmental obstacles could easily be more expensive in time and money than a switch to gas propellant. Xenon propellant would appear to be a clear choice over argon for intermediate power levels (several kilowatts to several tens of kilowatts) for near-earth missions. The advantage of xenon over

argon would be expected to result from the need for high thruster efficiency at moderate levels of specific impulse, as well as the high tankage fraction of argon. For small systems, such as attitude control and stationkeeping of conventional satellites, the performance level is less important and argon may be a serious competitor for xenon. For the largest power levels (above 100 kilowatts), the cost and availability of xenon could force the use of argon. With the amounts of propellant involved at these high power levels, the cryogenic liquid storage of argon (with a low tankage fraction) becomes a reasonable alternative to gaseous storage. Some high power applications also involve high specific impulses. The thruster efficiency loss due to a light atomic weight propellant is, of course, less at high specific impulses.

Another mission where the use of a gas propellant would be advantageous would be a comet or asteroid rendezvous where the contamination from thruster propellant is to be minimized during the final approach phase. In fact, a "clean" beam of inert-gas ions may be useful as a diagnostic tool. The sputtered efflux of a comet or asteroid mass could be analyzed by a mass spectrometer on the spacecraft. In comparison, the use of mercury ion beams on such cold bodies could lead to condensation of neutral propellant, with mercury sputtered particles making up the bulk of the sputtered efflux.

#### Summary of Recommendations

There are a number of tasks that are very important to the success of a gas thruster program relative to their costs. Some of these tasks are also long lead-time items. Because of their importance relative to their costs, the conduct of these tasks is recommended for even a fairly

low probability of using a gas thruster in space. These tasks are:

1. Discharge-chamber technology (Continuation of present effort).
2. Review of Mariner, Viking, and similar hardware for component suitability in gas thruster systems.
3. Fabrication of a closed loop breadboard control system using commercial components.
4. Starting and control tests with the breadboard system of Task 3.
5. Isolator tests, starting with the simplest types.
6. Cathode tests. Hollow cathodes for xenon and new cathode concepts for argon. (Continuation of existing effort.)
7. Sputtering tests of discharge-chamber components (other than cathodes).

Other tasks are also important, but, because of higher costs or less lead time required, should be conducted as the use of a gas thruster system becomes more certain. These tasks are:

8. Duration tests of specific argon and xenon cathode designs.
9. First class of Mission Studies. The direct comparison of xenon and mercury for near-future missions anticipated for mercury. Effort on argon (if any) should be lower level because of poorer expected performance.
10. Second class of Mission Studies. Missions in which the reduced contamination and/or environmental problems of an inert-gas propellant are important.
11. Development of flight-ready components such as control valve, flowmeter, isolator, cathodes, and discharge chamber.

## VII - CONCLUDING REMARKS

The multipole discharge chamber investigated herein has been shown capable of low discharge losses and flat ion beam profiles with a minimum of optimization. Minimum discharge losses were in the 200-250 eV/ion range for xenon and the 300-350 eV/ion range for argon. Flatness parameters in the plane of the accelerator grid were 0.85-0.95, which approximates the best values obtained previously in highly optimized designs. The design used employs low magnetic field strengths compared to other multipole designs, which permits the use of flat or cylindrical sheet-metal parts. The corner problem of the discharge chamber was adequately resolved with recessed corner anodes. The recessing increased the integrated field over these corner anodes to about the same value as for other anodes. This approach results in a fairly uniform distribution of electron currents to the anodes. Also a derivation was obtained for the electron containment by a varying magnetic field above multipole anodes.

Significant progress was also made towards long life argon hollow cathodes. The optimum diameter of the cathode chamber was found to be about 1.0-2.5 cm, larger than the sizes currently used for mercury hollow cathodes. This large size permits the use of replaceable internal emitters, as well as the use of more complex internal electrodes. The optimum orifice diameter ranged from 0.5-5 mm, depending on operating conditions. The use of an emitter bias voltage tended to extend the operating range and eliminate internal plasma fluctuations. An internal emitter was also found to be consistent with reliable starting.

The cathode studies described herein were conducted with a maximum discharge current of about 5 amperes. General scaling considerations

indicate argon should perform better in larger sizes, due to both the small ionization cross section and light atomic weight of argon. It is believed that these scaling considerations are involved in the large diameters found for optimum orifices and cathode chambers. These considerations also suggest improved performance may be expected at higher discharge currents.

A preliminary estimate of flight-type thruster mass was obtained. Basic 15 and 30 cm designs were estimated to have masses of about 4.2 and 10.8 kg. By contouring the anodes and pole pieces, these masses should be reduced to about 3.4 and 8.6 kg. Further mass reductions should be possible with the substitution of a lighter material for the stainless steel parts.

A study of gas thruster system requirements was also conducted, with recommendations made for a development program. These recommendations were divided into two categories: tasks that could conveniently be delayed, and tasks that should be conducted first due to their long lead time or their high ratio of value to cost.

## REFERENCES

### Section I

1. Reader, P. D., "The Operation of an Electron-Bombardment Ion Source with Various Gases," NASA TM X-5006 (1964); also in "International Conference on Electron and Ion Beam Science and Technology" (Wiley, New York, 1965), p. 925.
2. Schertler, R. J., "Preliminary Results of the Operation of a SERT II Thruster on Argon," AIAA Paper No. 71-157 (1971).
3. Byers, D. C., and Reader, P. D., "Operation of an Electron-Bombardment Ion Source using Various Gases," NASA TN D-6620 (1971); also in 11th Symposium on Electron, Ion, and Laser Beam Technology, Boulder, Colo., 1971.
4. Martin, A. R., "Design and Operation of an Ion Engine using the Rare Gases," Journal of the British Interplanetary Society, Vol. 26, pp. 742-752 (1973).
5. Martin, A. R., "Physical Behavior of some Biowaste Gases in an Ion Engine," AIAA Paper No. 73-1113 (1973).

### Section II

1. Kaufman, H. R., "Experimental Investigations of Argon and Xenon Ion Sources," NASA Contract Report CR-134845 (1975).
2. Moore, R. D., "Magneto-Electrostatically Contained Plasma Ion Thruster," AIAA Paper No. 69-620 (1969).
3. Ramsey, W. D., "12-cm Magneto-Electrostatic Containment Mercury Ion Thruster Development," J. Spacecraft and Rockets, Vol. 9, pp. 318-321 (1972).

4. Beattie, J. R., in "15 cm Diameter Ion Thruster Research" (by P. J. Wilbur) pp. 73-80, NASA Contract Report CR-134755 (1974).
5. Beattie, J. R., and Wilbur, P. J., "Cusped Magnetic Field Mercury Ion Thruster," AIAA Paper No. 76-1011 (1976).
6. Wilbur, P. J., "Experimental Investigation of a Throtttable 15 cm Hollow Cathode Ion Thruster," NASA Contract Report CR-121038 (1972).
7. Vahrenkamp, R. P., "Measurement of Double Charged Ions in the Beam of a 30 cm Mercury Bombardment Thruster," AIAA Paper No. 73-1057 (1973).
8. Beattie, J. R., in "15 cm Mercury Ion Thruster Research - 1975"(by P. J. Wilbur), pp. 100-106, NASA Contract Report CR-134905 (1975).
9. Kaufman, H. R., and Cohen, A. J.. "Maximum Propellant Utilization in an Electron-Bombardment Thruster." in Proc. Symp. Ion Sources and Format on Ion Beams, pp. 61-68. Brookhaven Nat. Lab. (1971).

#### Section IV

1. Byers, D. C., NASA Tech. Memo. TM X-52543 (1969).

#### Section VI

1. Owen, W. L., Jr., "A Noble Gas Ion Propulsion System," AIAA Paper No. 73-1114, 1973.
2. Schurmeier, H. M., editor, "Management and Design of Long-Life Systems," Vol. 34, AAS Science and Technology Series, 1974.
3. Salvinski, R. J., "Design of Mechanical Components for Long-Term Performance," AAS No. 73-059, Ibid., p. 111.
4. Hastings Mass Flow Instruments, Catalog No. 500D, p. 2, 1973.
5. Veeco's Vacuum Products 1975, Fast response piezoelectric gas leak valve, Model PV-10, p. 149.
6. Mirtich, M. J., AIAA Paper No. 75-343, 1975.

DISTRIBUTION LIST

	<u>No. of Copies</u>
National Aeronautics and Space Administration Washington, D. C. 20546	
Attn: RPE/Mr. Wayne Hudson	1
Mr. Daniel H. Herman, Code SL	1
 National Aeronautics and Space Administration Lewis Research Center 21000 Brookpark Road Cleveland, Ohio 44135	
Attn: Research Support Procurement Section	
Mr. Allen Jones, MS 500-313	1
Technology Utilization Office, MS 3-19	1
Report Control Office, MS 5-5	1
Library, MS 60-3	2
N. T. Musial, MS 500-113	1
Spacecraft Technology Division, MS 54-1	
Mr. E. Davison	1
Mr. R. Finke	1
Mr. D. Byers	1
Mr. B. Banks	1
Mr. S. Domitz	1
Mr. F. Terdan	1
Mr. P. Thollot	1
Mr. W. Kerslake	1
Mr. E. Theman	1
Mr. M. Mirtich	10
Physical Science Division, MS 301-1	
Mr. W. E. Moeckel	1
 National Aeronautics and Space Administration Marshall Space Flight Center Huntsville, Alabama 35812	
Attn: Mr. Jerry P. Hethcoate	1
 Research and Technology Division Wright-Patterson AFB, Ohio 45433	
Attn: (ADTN) Lt. David A. Fromme	1
 NASA Scientific and Technical Information Facility P. O. Box 8757 Baltimore/Washington International Airport Baltimore, Maryland 21240	40
 Case Western Reserve University 10900 Euclid Avenue Cleveland, Ohio 44106	
Attn: Dr. Eli Reshotko	1

Royal Aircraft Establishment Space Department Farnborough, Hants, England Attn: Dr. D. G. Fearn	1
United Kingdom Atomic Energy Authority Culham Laboratory Abingdom, Berkshire, England Attn: Dr. P. J. Harbour Dr. M. F. A. Harrison Dr. T. S. Green	1 1 1
National Aeronautics and Space Administration Goddard Space Flight Center Greenbelt, Maryland 20771 Attn: Mr. W. Isley, Code 734 Mr. R. Hunter Mr. R. Callens, Code 734	1 1 1
SAMSO Air Force Unit Post Office Los Angeles, California 90045 Attn: Capt. D. Egan/SYAX	1
Comsat Laboratories P. O. Box 115 Clarksburg, Maryland 20734 Attn: Mr. B. Free Mr. O. Revesz	1 1
Rocket Propulsion Laboratory Edwards AFB, California 93523 Attn: LKDA/Mr. Frank Mead	2
DFVLR - Institut für Plasmadynamik Technische Universität Stuttgart 7 Stuttgart-Vaihingen Allmandstr 124 West Germany Attn: Dr. G. Krülle	1
DFVLR - Institut für Plasmadynamik 33 Braunschweig Bienroder Weg 53 West Germany Attn; Mr. H. Bessling	1
Giessen University 1st Institute of Physics Giessen, West Germany Attn: Professor H. W. Loeb	1

Jet Propulsion Laboratory	
4800 Oak Grove Drive	
Pasadena, California 91102	
Attn: Dr. Kenneth Atkins	1
Technical Library	1
Mr. Eugene Pawlik	1
Mr. James Graf	1
Dr. John R. Beattie	1
Electro-Optical Systems, Inc.	
300 North Halstead	
Pasadena, California 91107	
Attn: Mr. R. Worlock	1
Mr. E. James	1
TRW, Inc.	
TRW Systems	
One Space Park	
Redondo Beach, California 90278	
Attn: Mr. M. Huberman	1
Dr. J. M. Sellen	1
National Aeronautics and Space Administration	
Ames Research Center	
Moffett Field, California 94035	
Attn: Technical Library	1
National Aeronautics and Space Administration	
Langley Research Center	
Langley Field Station	
Hampton, Virginia 23365	
Attn: Technical Library	1
Hughes Research Laboratories	
3011 Malibu Canyon Road	
Malibu, California 90265	
Attn: Dr. Jay Hyman	1
Mr. J. H. Molitor	1
Mr. T. D. Masek	1
Dr. R. L. Poeschel	1
Mr. R. Vahrenkamp	1
United States Air Force	
Office of Scientific Research	
Washington, D. C. 20025	
Attn: Mr. M. Slawsky	1
Princeton University	
Princeton, New Jersey 08540	
Attn: Mr. W. F. Von Jaskowsky	1
Dean R. G. Jahn	1
Dr. K. E. Clark	1

Communications Research Centre Ottawa, Ontario, Canada Attn: Dr. W. F. Payne	1
Joint Institute for Laboratory Astrophysics University of Colorado Boulder, Colorado 80302 Attn: Dr. Gordon H. Dunn	1
Department of Aeronautics and Astronautics Stanford University Stanford, California 94305 Attn: Professor Howard S. Seifert	1
Boeing Aerospace Co. P. O. Box 3999 Seattle, Washington 98124 Attn: Mr. Donald Grim	1
Intelcom Rad Tech 7650 Convoy Court P. O. Box 80817 San Diego, California 92138 Attn: Dr. David Vroom	1
Lockheed Missiles and Space Company Sunnyvale, California 94088 Attn: Dr. William L. Owens Propulsion Systems, Dept. 62-13	1
Fairchild Republic Company Farmingdale, New York 11735 Attn: Dr. William Guman	1
COMSAT Corporation 950 L'Enfant Plaza SW Washington, D. C. 20024 Attn: Mr. Sidney O. Metzger	1
Electrotechnical Laboratory Tahashi Branch 5-4-1 Mukodai-Machi, Tanashi-Shi Tokyo, Japan Attn: Dr. Katsuva Nakayama	1
Office of Assistant for Study Support Kirtland Air Force Base Albuquerque, New Mexico 87117 Attn: Dr. Calvin W. Thomas OAS Ge Dr. Berhart Lber OAS Ge	1 1

Bell Laboratories  
600 Mountain Avenue  
Murray Hill, New Jersey 07974  
Attn: Dr. Edward G. Spencer  
      Dr. Paul H. Schmidt

1  
1

Massachusetts Institute of Technology  
Lincoln Laboratory  
P. O. Box 73  
Lexington, Massachusetts 02173  
Attn: Dr. H. I. Smith

1